An Open Database of Free-Surface Gravity Waves for Validation of Numerical Wave Tanks

Martin Gjørvad Øen

Master's Thesis in Ocean Technology

University of Bergen

Department of Physics and Technology

June 2021

Preface

Several people have contributed to this master's thesis and made it possible. Therefore, I would like to extend my gratitude towards supervisors, fellow students and other contributors.

First and foremost, I would like to thank my supervisor, David Roger Lande-Sudall, for his excellent guidance during the experimental testing and many constructive discussions during the last year. I would also like to thank supervisor Øystein Lande for demonstrating patience while instructing me in using numerical tools and enlightening discussions in terms of hydrodynamic effects and theories. Also, Harald Totland deserves recognition for proofreading the thesis and formalities regarding the completion of the project.

Furthermore, I would like to thank all of my classmates for the great moments and good discussions during the two years at the University of Bergen. Special thanks to Trine Asp Sande, for the collaboration and assistance during the experimental investigation.

Last but not least, I would like to extend a thank you to Thomas Berge Johannessen, who has kindly shared data from his PhD research, allowing me to validate my experimental results.

Abstract

Advances within the field of structural reliability of offshore structures have shown that wave amplification beyond second-order predictions may substantially impact the design practice. Computational Fluid Dynamics (CFD) is a valuable tool that has shown that it can incorporate nonlinear behaviour, which further generates wave amplification and phase modulation. Therefore, it is essential to know if the applied CFD code can accurately capture this nonlinear behaviour present in waves when conducting numerical assessments of wave propagation.

Advances within the field of wave theories have resulted in the NewWave formulation, which describes the surface profile around the crest of extreme ocean waves. With this formulation, the surface dynamics of rogue waves for a given sea state can be modelled and investigated, and this is studied in the present thesis. Having calibrated the wave generator present at Western Norway University of Applied Sciences (HVL), several focused wave events, corresponding to the NewWave formulation and with variations in both frequency range, amplitude, and spectral shape, were conducted. Excellent agreement with previous focused wave experiments conducted by TB. Johannessen [1] validates the accuracy of the current experimental campaign. Moreover, the present study has exceeded the previous experiments and been able to generate non-breaking waves with a steepness of the surface profile close to the threshold of $ka = 0.55$, proposed by Toffoli et al. [2]. Furthermore, the most prominent wave amplification due to nonlinear behaviour was identified to be 60 % greater than the linear prediction for the highest amplitude wave events within the most narrow banded wave spectrum.

The validity of the CFD code Basilisk has been proven when utilised to investigate the same wave events from the experimental campaign. Numerical results and experimental results demonstrates good agreement, which validates the numerical tool's abilities to predict highly nonlinear wave propagation. The experimental data has further been organised and will be published as open-access, for use by other students, researchers and industry in the validation of numerical tools.

Contents

Preface **i**

Abstract **iii**

Nomenclature **xiv**

1 Introduction **1**

1.1 Background 1

1.2 Project description and aim of thesis 3

1.3 Synopsis of thesis 4

1.4 Limitations of the present study 5

2 Wave Groups and Wave Theories Used in the Present Study **7**

2.1 Linear wave theory 7

2.2 Second-order wave theory 13

2.3 Irregular waves 15

2.4 Standard wave spectrum 16

2.5 Focused irregular waves 20

3 Methodology **23**

3.1 Experimental background and spectral properties 23

3.2 Experimental method 24

3.2.1 Laboratory wave tank and wavemaker 25

3.2.2 Experimental setup 26

3.2.3 Test matrix and wave runs 30

3.2.4 Generating input to wave generator 32

3.2.5 Calibration of wavemaker 35

3.2.6 Sources of uncertainty 43

3.3 Numerical approach 48

3.3.1 Wave flume code . . . 48
3.3.2 Mesh generation . . . 51
3.3.3 Convergence testing of refinement levels . . . 54
3.3.4 Numerical wave input . . . 56
3.3.5 Numerical output . . . 57

4 Experimental Results and Discussion 61

4.1 Spectral energy density . . . 62
4.1.1 DUD wave cases . . . 62
4.1.2 BUD wave cases . . . 68
4.2 DUD - Surface measurements . . . 71
4.2.1 Surface elevation at the focal location . . . 71
4.2.2 Surface elevation at point of maximum crest . . . 84
4.2.3 Non-linearity and focus location . . . 90
4.3 BUD - Surface measurements . . . 92
4.3.1 Surface elevation at the focal location . . . 92
4.3.2 Surface elevation at point of maximum crest . . . 97
4.3.3 Non-linearity and focus location . . . 100
4.4 JONSWAP-focused wave groups . . . 102
4.4.1 Energy spectral density . . . 102
4.4.2 Surface elevation . . . 105
4.5 Repeatability of focused wave groups . . . 107
4.6 Measurement database . . . 110

5 Numerical Simulations of Wave Groups 111

5.1 Surface elevation . . . 111
5.1.1 Focal position comparison . . . 111
5.1.2 Point of maximum crest comparison . . . 113
5.2 Shift in focal location . . . 117

5.3 Suitability of numerical tool 119

6 Conclusion **123**

7 Suggestions for Further Work **125**

References **127**

Appendices **132**

A.1: MATLAB code - Spectral energy density 132

A.2: Basilisk - waveflume.c 136

A.3: Basilisk - DUD112 input file 141

List of Figures

1 Linear and regular wave train described by a cosine function. 11

2 Linear and second-order predictions of surface elevation for a regular wave with $H = 0.4$ m and $T = 1.33$ s. 14

3 Five individual regular waves, with different frequency, amplitude and phase, combined to make an irregular sea state (bottom). 15

4 Two types of wave spectra, one defined by JONSWAP-definitions and one truncated wave spectrum. 17

5 Concept of an irregular focused wave (bottom) presented with five individual wave components. 21

6 Experimental setup with wave gauges indicated with **X**. 27

7 Wave gauge setup showing how the gauges are linked to the wave generator and vice versa. 28

8 Spectral energy density calculations for DUD37 before and after calibration. . 37

9 Calculated phases for each frequency component in both measured time series and linear time series of DUD37. 40

10 Gain corrections applied for frequency components in both DUD and BUD wave cases. 42

11 Two different wave gauges with the upper wave gauge showing how the seeding particles have gathered on the probes near the water surface. 45

12 Tree structure illustrating how the mesh is divided into cells by adjusting the levels of refinement parameter. 51

13 Domain with variable levels of refinement (a) compared to the same domain with a fixed level of refinement (b). 52

14 Mesh and grid structure at the focal peak of numerical wave event DUD112. . 53

15 Measured peak height for the numerical DUD112 event with different levels of refinement. 54

16 Numerical time series with increasing levels of refinement from 8 to 13. Refinement level 8 is coloured in the lightest colour with increasingly darker colour up to refinement level 13. 55

17 Numerical wave event DUD112 with all 36 wave gauges positioned between 8.8 metres and 12.28 metres. 59

18 Spectral energy density calculations for all DUD wave events. Dotted line indicates the calculated spectral energy density from the measured time series, while solid line represents the theoretical spectrum. 63

19 Energy calculations for previous experiment and present experiment, with the DUD20 wave run from 1997 scaled up in advance of the energy calculations. . 64

20 Energy calculations for previous experiment and present experiment, with the DUD61 wave run from 1997 scaled up in advance of the energy calculations. . 65

21 Spectral energy density calculations for all BUD wave events. Dotted line indicates the calculated spectral energy density from the measured time series, while solid line represents the theoretical spectrum. 68

22 Measured time series of DUD37 at focal location plotted against the linear time series of DUD37. Time is centered around the desired focus time of 20 seconds. 71

23 DUD37 and DUD20 (1997) plotted against linear theory. DUD20 is align with the peak of DUD37 to make differences more identifiable. 73

24 Measured time series of DUD73 at focal location plotted against the linear time series of DUD73. Time is centred around the desired focus time of 20 seconds. 74

25 DUD73 and DUD40 (1997) plotted against linear theory. The provided data from Johannessen's experiments does not contain a full time series of DUD40, thus limiting the comparison of data to just around the time of focus. 75

26 Measured time series of DUD101 at focal location plotted against the linear time series of DUD101. Time is centered around the desired focus time of 20 seconds. 76

27 DUD101 and DUD55 (1997) plotted against linear theory. The provided data from Johannessen's experiments does not contain a full time series of DUD55, thus limiting the comparison of data to just around the time of focus. 77

28 Measured time series of DUD112 at focal location plotted against the linear time series of DUD112. Time is centered around the desired focus time of 20 seconds. 78

29 DUD112 and DUD61 (1997) measured at the focal location plotted against linear theory. 78

30 Measured surface elevation for both DUD115 (top) and DUD121 (bottom) compared against its respective linear prediction. 80

31 All the different wave events normalised with respect to their different linear target amplitude. The data is coloured with the lowest amplitude case of DUD37 being light grey and with increasing level of darkness as amplitudes increase all the way to DUD121 being coloured the darkest. 82

32 Surface profile measurements for all six wavegauges used in he DUD37 wave event. 84

33 DUD73 wave event with all six wave gauges. 85

34 DUD101 wave event with all six wave gauges. 86

35 DUD112 wave event with all six wave gauges 86

36 DUD115 wave event with all six wave gauges. 87

37 DUD121 wave event with all six wave gauges. 87

38 Normalised surface elevation of the focal peak for each DUD wave event at different positions from the wavemaker. Solid line represents a curve fitting for each wave case. 90

39 Measured time series of BUD37 at focal location plotted against the linear time series of BUD37. Time is centred around the desired focus time of 20 seconds. 93

40 Measured time series of BUD73 at focal location plotted against the linear time series of BUD73. Time is centered around the desired focus time of 20 seconds. 94

41 Measured time series of BUD95 at focal location plotted against the linear time series of BUD95. Time is centred around the desired focus time of 20 seconds. 95

42 BUD wave events measured at the focal position and normalised with respect to their linear target amplitude. 96

43 BUD37 wave event with all six wave gauges 98

44 BUD73 wave event with all six wave gauges 99

45 BUD95 wave event with all six wave gauges 99

46 Normalised surface elevation of the focal peak for each BUD wave event at different positions from the wavemaker. Solid line represents a curve fitting for each wave case. 101

47 JONSWAP defined wave spectra used in the experimental cases. 103

48 Energy calculations compared to theoretical energy spectrum for both JONSWAP wave events. 103

49 Measured surface elevation for both JONSWAP events with $T_p = 1.55$ seconds (top) and $T_p = 2.2$ seconds (bottom) compared against its respective linear prediction. 105

50 Five individual time series of DUD112 measured at wave gauge number 4 with solid line being the average surface elevation. 107

51 Five individual time series of DUD112 measured at wave gauge number 4 and zoomed in at the maximum crest elevation with solid line being the average surface elevation. 108

52 Numeric time series of DUD37 compared against experimental time series and time series computed with linear wave theory. 112

53 Numeric time series of DUD112 (top) and DUD121 (bottom) compared against its respective experimental measurements and linear time series. 113

54 Numerical time series of DUD112 (top) and DUD121 (bottom) compared against its respective experimental measurements. 114

55 Data from all wave gauges present in the numeric wave event DUD112. The blue line indicates data from the target focal position, while the red line indicates time series with maximum surface elevation. 117

56 Shift in focal position, relative to the target position at 8.8 metres, as a function of input amplitude. Results from Basilisk are marked with a square, and the experimental data is indicated with an asterisk. Locations of the experimental wave gauges are named and marked with a dashed line. 119

List of Tables

1 Examples of naming convention. 23

2 Label changes of experimental cases. 24

3 Longitudinal distance from the wavemaker for wave gauges in the present and previous experiments. 26

4 Test matrix for reproduced wave cases DUD and BUD. The target amplitude is obtained from linear theory, and the number of frequency components that make up the given spectrum is listed. 30

5 Test matrix for the JONSWAP wave events investigated in the experimental campaign. 31

6 Focal time and focal position for the different wave groups. 31

7 Wave generator input data for wave event DUD37 and DUD112 34

8 Input parameters used to simulate the wave tank at HVL. 50

9 Eight first frequency components used to define the numerical wave event of DUD112. 57

10 Comparison of energy calculations with present study and Johannessen's experiment. RMSE-value is calculated with respect to the theoretical spectrum for the given wave event. Maximum crest is given as a percentage deviation of the linear prediction and m_0 deviation is given as a percentage deviation between theoretical zeroth-order moment and the measured one. 66

11 Spectral energy density parameters for BUD wave events. RMSE-value is calculated with respect to the theoretical spectrum for the given wave event. Maximum crest is given as a percentage of the linear prediction and m_0 deviation is given as a percentage deviation between theoretical zeroth-order moment and measured. 69

12 Analysis of the three most prominent peaks in all wave runs seen in the data for the focal location. 82

13 Different parameters for the maximum wave crest measured in all wave cases. . 88

14 Nonlinear amplification and shifting in both time and space for the focal location of each experimental DUD wave event. Focal location is defined as the location where the wave events experience their maximum crest. 91

15 Different parameters for the maximum wave crest measured at the focal position for the BUD wave events. 97

16 Different parameters for the maximum wave crest measured in all BUD wave cases. 100

17 Nonlinear amplification and shifting in both time and space for the focal location of each experimental BUD wave event. 101

18 Energy calculations of measured energy spectrum for JONSWAP defined spectra with both $T_p = 1.55$ seconds and $T_p = 2.2$ seconds. 104

19 Parameters for the maximum wave crest measured at the focal position for the JONSWAP wave events. 106

20 Measured maximum amplitude for all wave events with average deviation compared to its respective average time series. 109

21 Comparison of maximum crest elevation, measured at the position of the experimental wave gauges, for all wave events. Deviation is defined as the difference between the numerical and experimental measurements, and given as a percentage of the experimental measurement. 115

22 Shift in focal location for all DUD wave events, both experimental and numerical. 118

23 Comparison of key parameters between the numerical and experimental wave event of DUD37, DUD101 and DUD121. Deviation is defined as the difference between the numerical and experimental events, and given as a percentage of the given experimental result. 120

24 RMSE value for the numerical time series compared against the experimental time series. All time series are measured at 8.8 metres and relative RMSE value is calculated from the wave events respective target amplitude. 121

Nomenclature

Symbol	Definition
A_C	Crest amplitude
A_n	Amplitude for wave component n
A_T	Trough amplitude
A_{max}	Maximum focal amplitude
A_{reg}	Amplitude for regular wave
$\boldsymbol{a}$	Acceleration term, Navier-Stokes
a_0	Fourier coefficient
a_n	Spectral shape parameter
a_f	Fourier coefficient a
b_f	Fourier coefficient b
$\boldsymbol{D}$	Deformation tensor
d	Water depth
E	Energy per unit area
E_n	Energy per unit area for wave component n
f	Frequency
f_n	Frequency for wave component n
f_p	Peak frequency
g	Gravitational acceleration
H	Wave height
H_s	Significant wave height
i_n	Frequency integer operator
k	Wavenumber
k_n	Wavenumber for component n
m_0	Zeroth-order spectral moment
m_n	n^{th}-order spectral moment
P	Fourier series period
p	Air pressure
$S(f)$	Spectral energy density
S_n	Spectral energy density for wave component n
T	Wave period
T_{dur}	Spectral repeat time
T_{DFT}	Spectral repeat time used in Discrete Fourier Transforms
T_p	Peak period
T_{WG}	Spectral repeat time defined by wave generator

t	Time
t_{foc}	Focal time
$\mathbf{U}$	Velocity field
U	Velocity
u	Horizontal particle velocity
$\boldsymbol{u}$	Fluid velocity vector
w	Vertical particle velocity
x, y, z	Three-dimensional co-ordinate system
x_{foc}	Focal position
α	Angle between SWL and tangent of wave profile
γ	JONSWAP spectral peakedness parameter
ϵ_n	Phase offset for component n
$\boldsymbol{\epsilon}$	Wave steepness parameter
η	Surface elevation
η_f	Fourier composed surface elevation
λ	Wavelength
λ_s	Froude scaling factor
μ	Fluid viscosity
ρ	Density
σ_a	Spectral width parameter
σ_b	Spectral width parameter
ϕ	Velocity potential
φ_f	Phase offset for Fourier wave components
φ_n	Angular phase for component n
ω	Angular frequency
ω_n	Angular frequency for component n

1 Introduction

1.1 Background

Rarely can one find a body of water open to the atmosphere that does not have waves on its surface. The description of the water surface and the field of water wave theory is well over 150 years old, and over the years, several books and papers have been written about the subject [3]. Still to this day, the linear wave theory developed by Sir George B. Airy in 1841 [4] is used extensively throughout the field of coastal engineering. However, more complex and detailed wave models have been developed over the years in order to capture the true behaviour of ocean gravity waves, with one of them being Stokes' second-order wave theory [5]. In 1985, the Stream function wave theory was developed by Robert G. Dean to examine fully nonlinear water waves with a numerical approach [6]. Subsequently, the second-order Stokes theory was extended to a fifth-order by John D. Fenton in order to analytically capture more of the true nonlinear behaviour of large ocean waves attributed to higher-order components [7]. These different wave theories have different validity ranges, determined by water depth, wavelength, and wave height.

The presented wave theories above are used for defining regular waves. Reals seas, however, are irregular and can be described by the summation of individual regular wave components, either linear or nonlinear. In terms of structural design, it is essential to capture the most extreme wave events, which for irregular waves means running long time series, both for experiments and numerical simulations. As a means to reduce the duration required for each design load case, one of the latest additions to the development of wave theories is the NewWave formulation developed by Peter S. Tromans et al. [8]. The NewWave formulation provides a method of analysing the extreme waves of a given wave field with a single wave compared to long time-domain simulations.

Application of this theory to wave load assessment may offer the realism of time-domain simulation of random wave fields with the speed and convenience of deterministic analysis [8].

In addition, this representation of a single rogue wave within a wave field opens up the possibility of detailed numerical simulations, where computational processing power previously has been a limiting factor.

Computational Fluid Dynamics (CFD) has become a frequently used tool to investigate various tasks related to engineering, one of them being the structural reliability of offshore structures. Events such as the Draupner-wave in 1995 [9], and the more recent Andrea-wave at Ekofisk in 2003 [10], showcase the importance of incorporating rogue wave events when assessing the structural reliability of offshore structures. In the case of the Draupner-wave, the linear NewWave formulation was modified to incorporate the fifth-order corrections defined by Fenton [7] and were able to match the measurements of the Draupner-wave accurately [9].

With the NewWave formulations being extensively validated in terms of load assessments on offshore structures [11, 12] and capabilities of predicting surface profile of extreme waves [9], several numerical studies with CFD, and experimental studies, have been performed using focused wave groups [13, 14, 15, 16]. Recently, T. Vyzikas et al. compared the surface dynamics of steep focused wave groups using three open-source numerical wave tanks (NWT). The results demonstrated that even weakly nonlinear solvers, such as SWASH and HOS-NWT, were able to simulate the higher order nonlinear wave-wave interactions present in focused wave groups with accuracy [17]. Furthermore, Ø. Lande and TB. Johannessen demonstrated the applicability of the commercial CFD-code ComFLOW and the open-source code Basilisk when reproducing the wave cases investigated by TB. Johannessen [1]. Results from ComFLOW and Basilisk reveal that both CFD-codes can capture the higher-order amplifications and shift in the focal position well [18].

Common for several of the numerical investigations into focused wave groups is the comparison with experimental results, such as in Ning et al. [19] where free-surface evolution and wave kinematics for nonlinear and uni-directional focused wave groups were investigated. Without accurate experimental data, it is challenging to evaluate if a numerical wave tank will yield the correct result and recreate the higher-order nonlinear behaviour present in steep focused wave groups. Moreover, the choice of CFD-tool used for a given wave case can di-

rectly influence the computational cost. For example, a seemingly less accurate and faster solver might be suitable for a particular wave event, such as demonstrated by Vyzikas et al., where both SWASH and HOS-NWT yielded precise results for the particular wave events investigated [17].

Conducting experimental investigations, and obtaining accurate results to validate a numerical wave tank, is a rigorous and time-consuming undertaking. To the author's knowledge, there are currently very few free and available online databases containing surface measurements from accurately calibrated wave experiments. Such a free and available source of data may be used to validate numerous CFD codes with respect to wave propagation capabilities and will, at the same time, reduce the need for an extensive experimental validation campaign. Hence, the main aim of the present project is to obtain high-quality surface measurements from focused wave events, both linear, nonlinear and close to the breaking limit, which can further be used by students, researchers, and industry to validate and fine tune CFD software without the need for an extensive experimental investigation.

1.2 Project description and aim of thesis

The aim of the present thesis is two-fold. Firstly, obtain high-quality surface measurements from focused wave events varying in both frequency range and amplitudes. With these measurements, properties such as steepness, agreement with linear wave theory, nonlinear amplification and shift in focal position will be examined. Furthermore, the repeatability of the focused wave groups will be assessed, and results from the present study will also be compared directly to available data provided by TB. Johannessen from his experimental investigation in 1997 [1]. Subsequently, uncertainties regarding the geometric scaling of wave components can be identified. The measurements, as well as the wave generator input, shall be gathered in an open database free to use for other students, researchers and industry.

The second aim of this thesis is to validate a CFD code in terms of wave propagation capabilities with the use of the measurements gathered from the main aim. This part will showcase

how the measurement database can be used to validate CFD codes, and the capabilities of the numerical Basilisk solver will also be assessed.

1.3 Synopsis of thesis

The outline of the present thesis is summarised below.

- Chapter 2 presents fundamental wave theory used to describe the wave events further presented in the thesis. How basic linear wave theory, and other common relations, can be utilised to create a focused wave will also be presented.
- Chapter 3 documents the experimental setup and the wave events selected for the main experimental investigation. In addition, the approach for the generation of wave input for both the wavemaker and the numerical tool will be addressed, as well as a review of the numerical tool used in the present study. Furthermore, an utmost important part of the experimental investigation is calibrating the wave generator. Thus, an extensive review of the calibration process will be presented.
- The results from the experimental campaign will be presented and discussed in Chapter 4. Parameters such as crest height and wave steepness will be identified, as well as the nonlinear behaviour of the different wave events. Where data is available, the present wave cases will be directly compared to data obtained from TB. Johannessen's PhD research [1]. Investigations into the stability and repeatability of the wave groups will also be discussed.
- Chapter 5 will present the results from the Basilisk solver for the wave cases within the DUD wave group. These time series will be compared with the experimental cases, and the shift in focal position due to nonlinear behaviour will be identified. The overall suitability of the numerical tool is further assessed.
- Finally, the conclusions and recommendations for future work will be presented in Chapter 6 and 7, respectively.

1.4 Limitations of the present study

The present study has only considered non-breaking focused wave groups. Therefore, validation of CFD codes in terms of wave-breaking prediction cannot be performed with the current measurement database.

Furthermore, the wave gauges used in the experimental investigation are positioned along the centre line of the wave tank. Therefore, the wave gauge setup is insufficient for validating three-dimensional CFD codes. Moreover, the total number of wave gauges present in the test facilities has also been a limiting factor in terms of the measurement setup.

The deep water wave tank present at Western Norway University of Applied Sciences (HVL) is currently not suitable to capture waves propagating over shallow water. Thus, validating a CFD code designed to capture shallow water effects using surface measurements from this thesis is not recommended.

2 Wave Groups and Wave Theories Used in the Present Study

This chapter introduces and reviews relevant wave theories explored throughout this thesis. This section will aid readers who are unfamiliar with wave theory, but also more experienced readers, to comprehend the contents of this thesis in a better manner.

The following parts will describe how the motion of the surfaces can be mathematically described in the most basic forms and how these formulations can be linked to describe more complex and disorderly sea states.

2.1 Linear wave theory

Linear wave theory, also known as the Airy wave theory, assumes that the height of the wave is significantly less than the wavelength. This dictates proportionality between the wave height and the parameters of interest, such as particle velocity and particle acceleration. This characterises linear wave theory. Both regular and irregular waves can be mathematically explained by linear wave theory. However, the way to analyse the two is different.

Linear wave theory is based on potential theory and sets four conditions to be able to determine the velocity potential of a wave [20]. These four conditions are as follows:

1. The continuity equation, or Laplace's equation, must be satisfied.
2. The normal velocity towards the bottom must equal zero at the finite water depth, d.
3. Bernoulli's equation shall apply at the free-surface (dynamic condition).
4. Kinematic condition at the free-surface must be satisfied.

The first condition states that Laplace's equation must be satisfied. By this is meant that the

divergence, as well as the curl, of the velocity vector should equal zero, i.e. an incompressible and rotation-free flow is required. For an incompressible flow, the continuity equation can be written as in Equation (2.1).

$$\nabla \mathbf{U} = 0 \tag{2.1}$$

In addition, if the liquid is rotation-free, i.e. the curl of the velocity vector is zero, the velocity field can be expressed as the gradient of a scalar function, ϕ [20].

$$\mathbf{U} = \nabla \phi$$

This means that for an incompressible and rotation-free flow, Equation (2.1) can be rewritten to Laplace's equation given by Equation (2.2).

$$\nabla^2 \phi = 0 \tag{2.2}$$

In other words, the first condition states that an incompressible and rotation-free flow is required and can be written as follows for a flow in three dimensions:

$$\nabla^2 \phi = \nabla(\nabla \phi) = \nabla \mathbf{U} = \frac{\partial^2 \phi}{\partial x^2} + \frac{\partial^2 \phi}{\partial y^2} + \frac{\partial^2 \phi}{\partial z^2} = 0$$

The second condition states that the velocity normal to the bottom, at the finite sea depth d, should equal zero. Hence, there will be no flow penetrating through the seabed. Assuming that the seabed is horizontal, this can be described mathematically as:

$$\left(\frac{\partial \phi}{\partial z} \right)_{z=-d} = 0$$

The third condition states that Bernoulli's equation shall apply at the free-surface. This can be investigated by applying Bernoulli's equation between two points on the free-surface. Here, a point A is selected as well as a new arbitrary point on the surface. It can be written as follows:

$$\frac{p}{\rho} + \frac{1}{2}U_A^2 + g\eta_A + \frac{\partial \phi_A}{\partial t} = \frac{p}{\rho} + \frac{1}{2}U^2 + g\eta + \frac{\partial \phi}{\partial t} = constant$$

The air pressure, p, is constant for both points, which means that the static pressure term can be removed from the expression. The particle velocity, U, at the surface is negligible due to the assumption of small amplitude waves, meaning that the velocity term is significantly smaller than the rest of the terms. The expression can then be reduced to the following:

$$g\eta_A + \frac{\partial \phi_A}{\partial t} = g\eta + \frac{\partial \phi}{\partial t} = constant$$

If the wave surface elevation, η, is defined as a cosine function, and the wave phase in point A is set to be $\pi/2$, the term containing $g\eta_A$ disappears. If Bernoulli's equation is to be valid at the free-surface in this case, the whole left side of the equation must equal 0. The remaining expression on the left side is the time derivative of the velocity potential, ϕ_A. For it to be zero, the velocity potential must be defined by a sine function. In this way, the time derivative of the velocity potential will become a cosine function, such as the wave surface elevation, η, and therefore also become zero at the given wave phase in point A. Under these conditions, combined with the assumption of small amplitude waves, Bernoulli's equation can again be reduced to the following:

$$g\eta + \left(\frac{\partial \phi}{\partial t}\right)_{z=0} = 0$$

The fourth and final condition for determining the velocity potential of a wave states that the kinematic condition at the free-surface must be satisfied. This means that fluid particles on

the free-surface of low waves always remain on the surface. This condition can be expressed in that the velocity, in the perpendicular direction to the surface, of the fluid particles is equal to the velocity of the surface profile perpendicular to itself [20]. This can be expressed mathematically as follows:

$$U_{surface} = U_{particle}$$

$$\frac{\partial \eta}{\partial t}\cos(\alpha) = w\cos(\alpha) - u\sin(\alpha)$$

Where w is the vertical particle velocity, u is the horizontal particle velocity, and α is the angle between the horizontal plane, or still water level, and the tangent of the wave profile at the given point.

By using these four conditions, and making sure that they are satisfied, the velocity potential of a cosine wave can be deduced and expressed as in Equation (2.3). Furthermore, the formulas used to describe vertical and horizontal particle velocity and particle acceleration can further be derived from Equation (2.3).

$$\phi = \frac{g\eta_A}{\omega}\frac{\cosh(k(d+z))}{\cosh(kd)}\sin(kx - \omega t) \tag{2.3}$$

The velocity potential in Equation (2.3) is based on the first three conditions. A new relation can be deduced from the fourth and final condition, which is the kinematic condition at the free-surface. This is called the dispersion relation and describes the relation between frequency and wavelength. The dispersion relation is given by Equation (2.4).

$$\omega^2 = kg\tanh(kd) \tag{2.4}$$

By using Equation (2.3), and (2.4), together with the definitions of hyperbolic functions, it is possible to derive the formulae used to describe kinematic and dynamic properties, such

as particle velocity and surface elevation, of a linear and regular wave as shown in Figure 1.

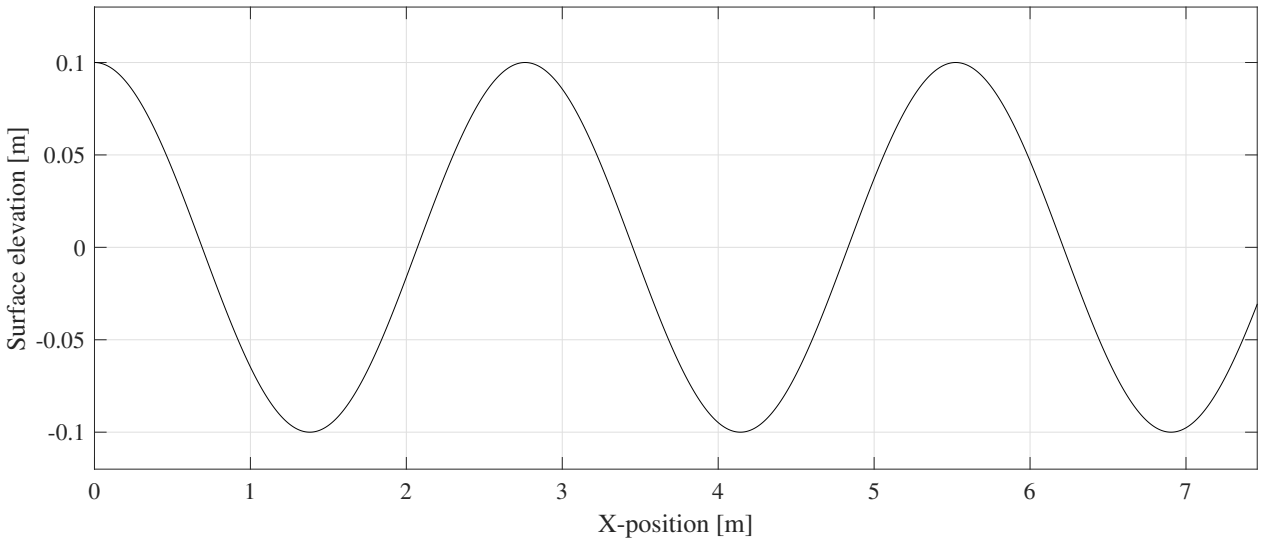

Figure 1: Linear and regular wave train described by a cosine function.

Linear wave theory covers waves, as shown in Figure 1, where the wave height is not higher than the wavelength, λ, divided by seven, commonly known as Stokes' limit for breaking waves [5]. Waves approaching, and exceeding this limit, will take an increasing nonlinear shape before breaking, and the deviation affiliated with the use of linear wave theory will therefore increase the higher the waves get. For wave heights below this limit, it is possible to use the formulas derived from the velocity potential and the dispersion relationship. However, there are more appropriate theories for steeper waves.

With the formulae described by linear wave theory, it is possible to calculate wave profiles and dynamic pressure together with particle velocity and particle acceleration. The relationship between depth and wavelength determines whether it is possible to simplify the equations provided by linear wave theory. This simplification applies to deep water waves where $d/\lambda > 0.5$. For wave situations that do not satisfy the deep-water criterion, formulae for finite water depth are used. These formulae are valid regardless of the water depth. Although the wave tank present in the MarinLab facility is defined as a deep water wave tank, the equations for finite water depth are used for calculations throughout this thesis. Using the equations for finite water depth removes the chance of error affiliated with the use of the simplified

equations, as some waves might be close to the simplification criterion of $d/\lambda > 0.5$.

As this thesis focuses on the surface profile of gravity waves, the main equations used are the ones describing the linear surface profile and the relation between wavelength and wave period. These two identities are described in Equation (2.5) and (2.6), respectively.

$$\eta(x,t) = \frac{H}{2}\cos(kx - \omega t) \tag{2.5}$$

$$\lambda = \frac{g}{2\pi}T^2 \tanh\frac{2\pi d}{\lambda} \tag{2.6}$$

Here, η denotes the surface profile, while H is the wave height of the regular wave event. ω is the angular frequency, t represents time, and together with the wavenumber, k, and position, x, these variables define the phase of the wave. The wavenumber, k, is defined as $k = 2\pi/\lambda$. Furthermore, Equation (2.6) describes the relation between wavelength, λ, and wave period T. Gravitational acceleration, g, is included along with the water depth, d.

2.2 Second-order wave theory

As mentioned in the previous section, linear wave theory holds for waves where the wavelength is significantly larger than the wave height. For larger waves with more prominent nonlinear effects, higher-order wave theories should be considered. For these waves, Stokes' wave theory will serve as a more accurate prediction of the surface elevation relative to linear wave theory. The second-order wave theory is based upon the same initial conditions as the linear wave theory. However, the Stokes wave expansion is an expansion of the surface elevation in powers of the linear wave height, H [21]. The surface profile for a regular second-order Stokes wave, at arbitrary water depth, is given by Equation (2.7) [21].

$$\eta(x,t) = \frac{H}{2}\cos(kx-\omega t) + \frac{\pi H^2}{8\lambda}\frac{\cosh(kd)}{\sinh^3(kd)}(2+\cosh^2(kd))\cos^2(kx-\omega t) \tag{2.7}$$

Characteristic for a Stokes wave is the higher crests and the shallower troughs. Contrary to linear wave theory, the crests and troughs in a Stokes wave exhibit asymmetrical properties. Furthermore, the troughs are wider and the crests are narrower than the surface profile predicted by linear wave theory. These distinct characteristics, defined by the second-order definition in Equation (2.7), make up a surface profile that is more representative of large ocean waves than the comparable prediction by linear wave theory [20]. For a deep-water, second-order Stokes wave, the asymmetry between the crest and the trough can be described by Equation (2.8) and (2.9), where A_C and A_T denotes the crest and trough amplitudes. Notably, the crest increases with the same amount as the trough, keeping the wave height unchanged compared to predictions with linear wave theory [21].

$$A_C = \eta(kx-\omega t=0) = \frac{H}{2}\left(1+\frac{\pi H}{2\lambda}\right) \tag{2.8}$$

$$A_T = |\eta(kx-\omega t=\pi)| = \frac{H}{2}\left(1-\frac{\pi H}{2\lambda}\right) \tag{2.9}$$

Figure 2 demonstrates the key distinctions between a second-order and linear wave. Both of the surface profiles displayed in Figure 2 have the same input parameters, a wave height of 0.4 metres and a wave period of 1.33 seconds, but are solved using Equation (2.5) and (2.7). The water depth in the equation, which is only directly included in the second-order theory, is set to 2.2 metres, the same as in the wave tank present at HVL.

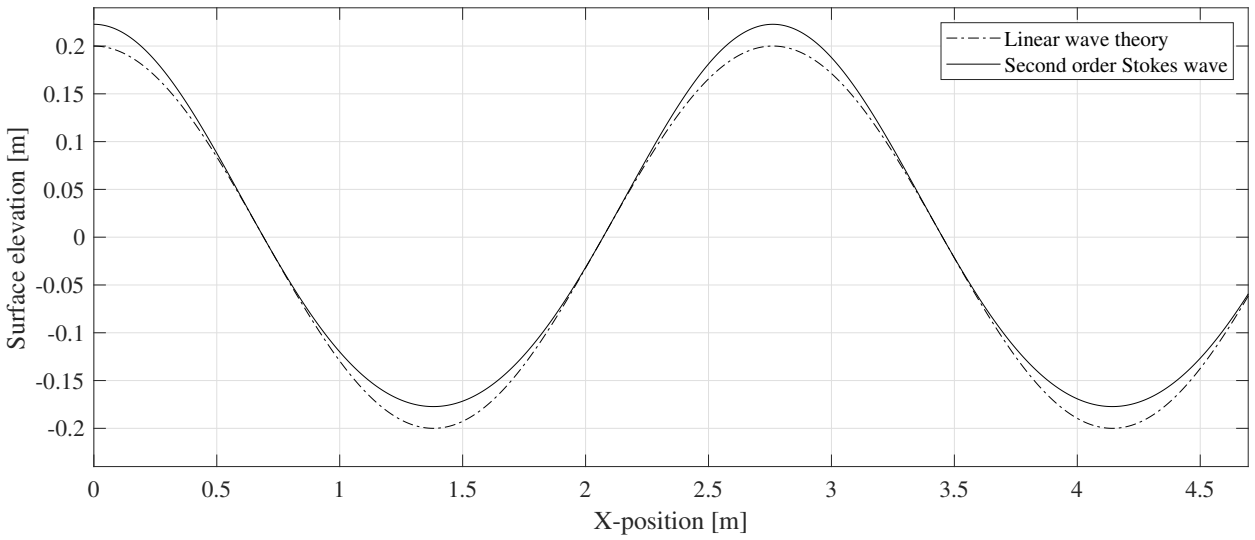

Figure 2: Linear and second-order predictions of surface elevation for a regular wave with $H = 0.4$ m and $T = 1.33$ s.

The linear dispersion relation, given by Equation (2.4), is also valid for the second-order expansion of the Stokes wave. Hence, the wavelength and phase velocity of the wave remains independent of the wave height [21].

For some of the wave events in the present study, the surface elevation consists of components that act far from linear. To capture the nonlinear effects displayed in Figure 2, the CFD tool used in the numerical investigation of the wave events generates second-order wave kinematics according to the definitions of Sharma & Dean [22]. Thus, implementing second-order wave theory in the numerical tool will generate a more accurate representation of the free-surface measured in the experimental investigation and capture the nonlinear behaviour to a greater extent than if linear wave theory was applied.

2.3 Irregular waves

By now, two different approaches for modelling a regular wave has been presented, with one of them able to capture more of the nonlinear behaviour present in large free-surface gravity waves. However, none of the regular wave models presented can recreate the random surface profile observed for actual sea states in the ocean. Nevertheless, the two different wave models can further be used to describe this chaotic and random behaviour.

Irregular sea states can be described as a sum of regular waves with different amplitudes, frequencies and with random phases. By the use of linear superposition, these regular wave components can describe the irregular surface elevation [23]. Figure 3 offers a description of how different components make up an irregular sea state. Here, five regular waves, with different frequency, amplitude and phase, are summed up with the result being the bottom time series.

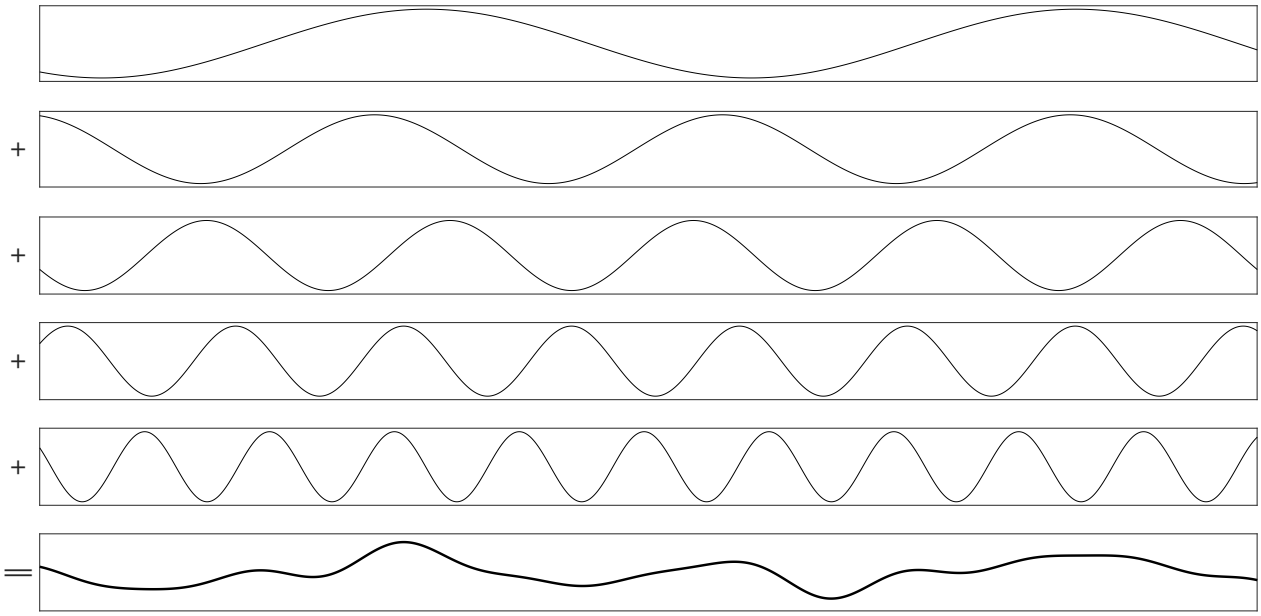

Figure 3: Five individual regular waves, with different frequency, amplitude and phase, combined to make an irregular sea state (bottom).

Furthermore, the irregular surface profile in Figure 3 can be defined mathematically using Equation (2.10), where n denotes an individual wave component, and N is the total number

of wave components. Finally, A_n and ϵ_n denotes the amplitude and phase offset, respectively. The phase offset, ϵ_n, takes a random value between 0 and 2π radians.

$$\eta(x,t) = \sum_{n=1}^{N} A_n \cos(k_n x - \omega_n t + \epsilon_n) \tag{2.10}$$

Linear wave theory has been used to model the surface elevation of the irregular sea state in Figure 3. However, the irregular surface profile can also be modelled with the second-order theory, presented in Section 2.2, by substituting the linear expression in Equation (2.10).

The distribution of amplitudes and frequencies for the individual wave components constitutes the sea states spectral information. With this information in place, any irregular sea state can be modelled using Equation (2.10). The following section will introduce how this spectral information is distributed and how some common sea states can be represented using standardised wave spectra.

2.4 Standard wave spectrum

As discussed, the distribution of amplitudes and frequencies within an irregular sea state can be described as a wave spectrum. A wave spectrum describes the distribution of energy density over a given frequency range. In addition, any wave spectrum described with energy can also be expressed as amplitude distribution over the same frequency range. Figure 4 displays two different types of wave spectra, one defined with the JONSWAP (Joint North Sea Wave Project) definitions and a truncated wave spectrum defined as in Baldock and Johannessen's experiments [24, 1].

Each wave spectra describes a specific sea state corresponding to the frequency distribution and the overall energy content. The most notable difference between the two is the presence of clearly defined cut-off frequencies displayed in Figure 4b. In contrast, Figure 4a has spectral components defined throughout the frequency range of 0 to 2 Hz.

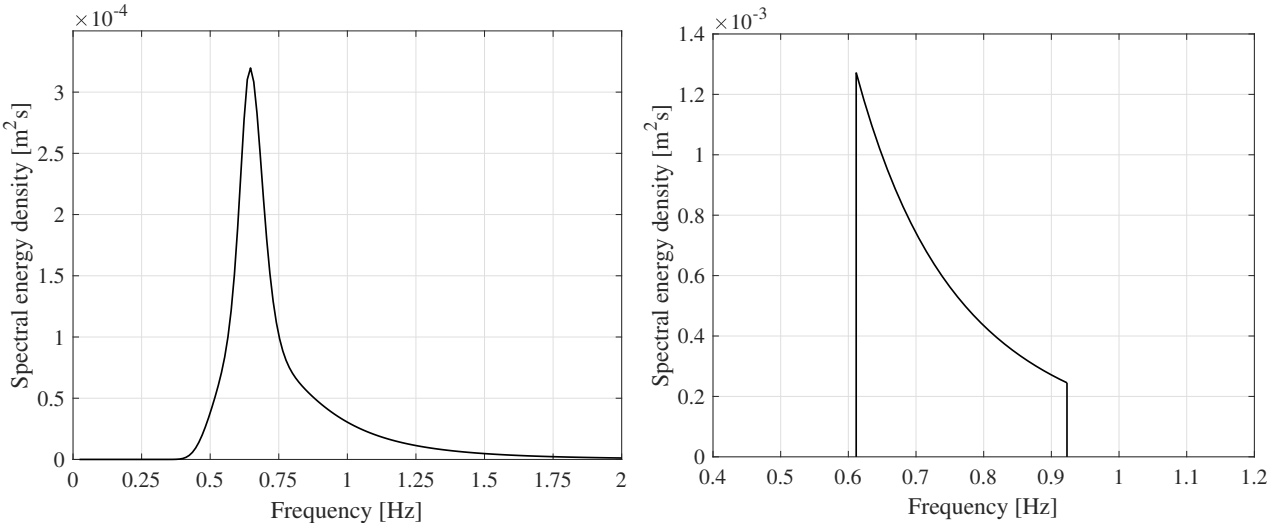

(a) JONSWAP defined wave spectrum.

(b) Truncated wave spectrum.

Figure 4: Two types of wave spectra, one defined by JONSWAP-definitions and one truncated wave spectrum.

Furthermore, the energy per unit surface area for wave component n, is given by Equation (2.11). This energy quantity corresponds to the n^{th} wave component, which, together with all wave components, make up the surface profile of an irregular sea state.

$$E_n = \frac{1}{2}\rho g A_n^2 \tag{2.11}$$

As both the density, ρ, and the gravitational acceleration, g, remain constant for all the wave components, 1/2 multiplied with the wave components amplitude, A_n, squared, becomes a parameter which is a measure of energy per unit surface area. The total energy per unit surface area for a given sea state can be described as the sum of energy contributions from N harmonic waves, thus defined by Equation (2.12) [20]. $A_n(f_n)$ denotes the amplitude of a wave component with frequency f_n.

$$\frac{E}{\rho g} = \sum_{n=1}^{N} \frac{1}{2} A_n^2(f_n) \tag{2.12}$$

The wave spectra, or spectral energy density, $S(f)$, can be introduced such that an area within a given frequency interval, Δf, equals the energy contribution for all the wave components within this frequency interval. This can be expressed mathematically with Equation (2.13).

$$\frac{E}{\rho g} = \sum_{n=1}^{N} \frac{1}{2} A_n^2 = \sum_{n=1}^{N} S(f_n) \Delta f \tag{2.13}$$

From Equation (2.13), the relation between the wave components amplitude and the spectral energy component can be derived. This expression, given by Equation (2.14), is used throughout this project to link the spectral energy components of a given wave spectrum to the amplitude components given as input to the wave generator. This relation is valid for both types of wave spectra displayed in Figure 4. However, their spectral shape is defined using two distinct forms.

$$A_n = \sqrt{2S(f_n)\Delta f} \tag{2.14}$$

The JONSWAP wave spectrum was the result of a joint wave measurement project for the southeast parts of the North sea in 1968, and 1969 [20]. Measurements from this particular region revealed that the resulting energy spectrum had a significantly sharper, thus higher, peak than another standard wave spectrum, the Pierson-Moskowitz spectrum. This led to the definition of the JONSWAP wave spectrum, which is a modification to the Pierson-Moskowitz spectrum. The JONSWAP spectrum is frequently studied for engineering applications, and especially in terms of structural assessments for offshore wind energy, such as [25, 26]. As a result of the relevance of the spectrum, JONSWAP defined wave events has been included in the experimental campaign. In this thesis, the JONSWAP wave spectrum has been defined according to Equation (2.15),

$$S(f) = A \frac{5}{16} H_s^2 f_p^4 f^{-5} \exp\left(-\frac{5}{4}\left(\frac{f}{f_p}\right)^{-4}\right) \gamma^{\exp\left(-\frac{1}{2}\left(\frac{f-f_p}{\sigma f_p}\right)^2\right)} \tag{2.15}$$

where σ and A are defined in the following way:

$$\sigma = \begin{cases} \sigma_a = 0.07 & \text{if} \quad f \leq f_p \\ \sigma_b = 0.09 & \text{if} \quad f > f_p \end{cases}$$

$$A = (1 - 0.287)\log(\gamma)$$

The spectral peakedness parameter, γ, is defined as the relation between the peak-value of the comparable Pierson-Moskowitz spectrum and the peak-value of the JONSWAP spectrum. Both γ and σ are selected according to the mean spectrum definitions of Hasselman et al. [27], giving γ the value of 3.3. With the mean spectrum definitions, the JONSWAP wave spectrum can be computed using only significant wave height, H_s, and peak period, T_p, as input.

With a defined wave spectrum, the distribution of all the wave components is known, as well as the information needed to investigate the statistical properties of the surface elevation of the sea state. Subsequently, information about significant wave height, characteristic wave periods and most probable maximum wave height can be determined by investigating the n^{th} order spectral moments given by Equation (2.16). Here, frequency is given as angular frequency, ω.

$$m_n = \int_0^\infty \omega^n S(\omega)\, d\omega \qquad\qquad n = 0, 1, 2, .. \tag{2.16}$$

2.5 Focused irregular waves

A focused irregular wave event can be designed using key aspects from the different wave theories presented in the previous sections. According to Tromans et al. [8], the NewWave formulation, which describes a focused irregular wave and the most probable extreme wave of a given sea state, agrees excellently with the time-domain simulations of the same sea state. Rather than simulating a typical three-hour interval of an irregular sea state, the NewWave formulation can be applied, and the most probable maximum wave of a given sea state can be measured experimentally with one single wave. The wave theory developed by Tromans et al. [8] defines all the regular wave components, which make up the given sea state, to come into phase at a desirable location in both time and space. Hence, the surface profile of a uni-directional focused irregular wave event can be expressed, in the same way as an irregular wave event from Section 2.3, given by Equation (2.10).

However, the key distinction between an irregular sea-state and a focused irregular wave event is the definition of the phase offset, ϵ_n. For irregular sea-states, this is a random value between 0 and 2π radians. For a focused irregular wave event, this term is determined such that all the wave components come into phase at a given location in time and space. Resultantly, the maximum wave amplitude in a focused wave event will be the superposition of all the independent wave components amplitudes. This can be expressed as in Equation (2.17).

$$A_{max} = \eta(x = x_{foc}, t = t_{foc}) = \sum_{n=1}^{N} A_n \tag{2.17}$$

Using the same example presented in Figure 3, the irregular wave event can be transformed into a focused wave event by rearranging the random phase offset, ϵ_n. The result of this rearrangement can be seen in Figure 5, where the maximum of each wave component comes into phase at a given location to create a focused wave.

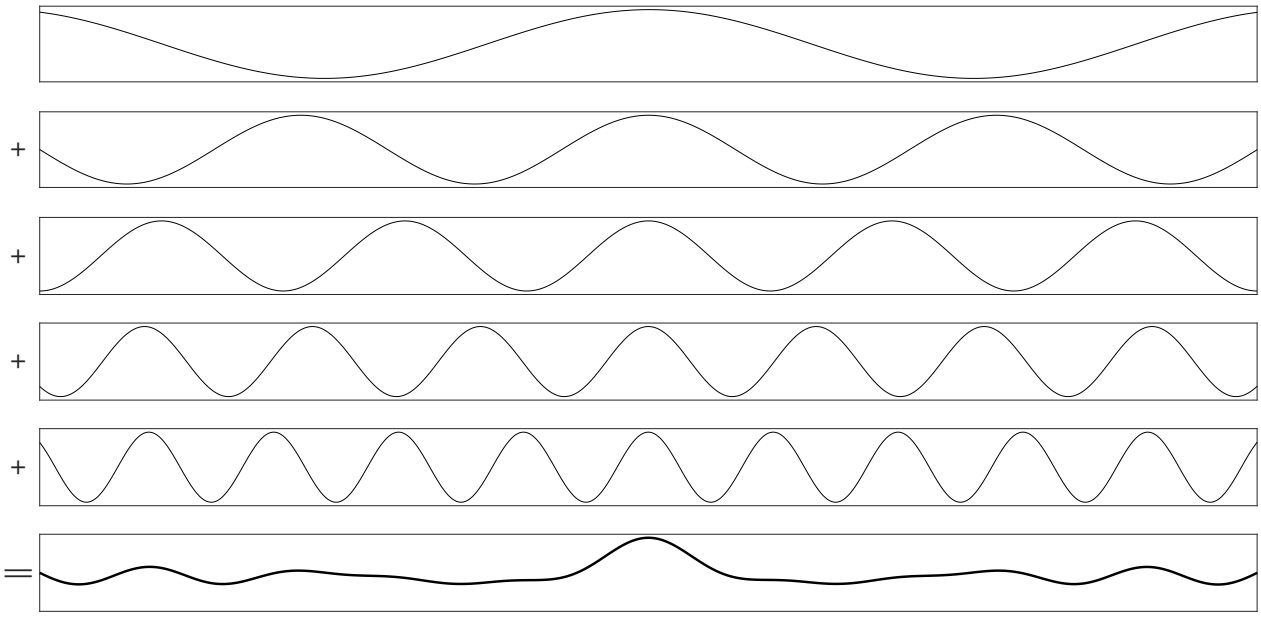

Figure 5: Concept of an irregular focused wave (bottom) presented with five individual wave components.

The spectral information presented in Section 2.4, which determines the amplitude or energy distribution for the given sea state, will influence the surface profile of the focused wave. Nevertheless, for a focused wave event composed of N linear wave components, the surface profile will be symmetrical about the focal crest.

The NewWave definition, and the generation of a focused wave event, opens up the possibility of determining an adequate design wave for a given sea state without rigorous and time consuming experimental testing. Furthermore, it enables the generation of relatively high and steep surface waves without pushing the wave generator to its limits, resulting in significantly more stable wave generation. Moreover, the reduction in simulation time for identifying the most probable maximum wave has made focused wave groups a desirable wave event in terms of numerical investigations into large ocean waves, for example, [28, 17, 19, 29].

3 Methodology

In the present chapter, all relevant information regarding the experimental test cases will be presented. As this thesis reproduces and advances upon previous experiments, the previous experiments and the differences with the present experiments will be addressed. Furthermore, the details regarding the choice of sea state for the JONSWAP events will be presented. An extensive description of the measurement setup and the calibration process will also be documented, as well as the numerical approach for the numerical validation of the experimental results.

3.1 Experimental background and spectral properties

In 1996, TE. Baldock et al. designed four different wave spectra, A, B, C and D [24]. Keeping the frequency range for a given spectrum constant and changing the energy content, or in other words amplitude, he conducted laboratory experiments and compared them against linear and second-order solutions. Later, TB. Johannessen reproduced these wave groups using spectrum B, C and D [1]. In his experiments, Johannessen also introduced directional spreading of the wave groups. In the present study, spectrum B and D have been reproduced and scaled according to the change in water depth. Both Baldock and Johannessen conducted their experiments with a water depth of 1.2 meters, while the experiments presented in this thesis were conducted with a water depth of 2.2 metres.

Table 1: Examples of naming convention.

Label	Description
D UD 20	Spectrum **D**, **U**ni-**D**irectional, **20** mm target amplitude
B UD 95	Spectrum **B**, **U**ni-**D**irectional, **95** mm target amplitude

For clarity, the wave spectrum is labelled in the same way as the previous experiments. Table 1 shows two examples of case labelling and how the naming convention is applied by

Johannessen. Further on, all the reproduced test cases in this thesis will be referred to by using this naming convention.

However, as a result of experimental scaling, the test runs have been relabelled compared to Johannessen. Table 2 shows the original case labelling and the resulting label for the present investigation. Johannessen's naming convention has been used to label experiments in both cases, but values for amplitude have been changed due to experimental scaling. Values for amplitude have also been rounded to the nearest millimetre to keep the labelling simple and clear.

Table 2: Label changes of experimental cases.

Johannessen (1997)	**Present Study**
DUD20	DUD37
DUD40	DUD73
DUD55	DUD101
DUD61	DUD112
BUD20	BUD37
BUD40	BUD73
BUD52	BUD95

3.2 Experimental method

In the following sections, the experimental test campaign will be reviewed and explained. First, an introduction to the test facility and how the experimental setup was configured will be given, followed by a review of the main test cases. As this thesis aims to develop a database consisting of highly accurate wave events, a thorough calibration process is needed to ensure that the output is as equal to the target cases as possible. Hence, an explanation of the calibration will be described along with the resulting transfer function and wavemaker input. Finally, a description of the numerical model used to replicate the experimental cases will be presented.

3.2.1 Laboratory wave tank and wavemaker

All the experiments in this thesis were conducted in HVL's MarinLab. The test facility is equipped with a towing tank measuring 50 metres long and 3 metres wide, and the tank is 2.2 metres deep. Waves are generated using a flap-type wavemaker which consists of 6 individual hinged wave paddles. Each paddle is 0.5 metres wide, and they are force-feedback controlled, enabling dampening of unwanted tank wall reflections. The paddles are mounted on top of a ledge approximately 1 metre above the tank floor. This configuration will generate decaying particle motion from the surface and down to the mounting point. This reduction in the horizontal particle motion is typical for deep water ocean waves and the reason why a hinged paddle wavemaker is chosen for HVL's deep water tank, rather than a piston wavemaker which is typically used for shallow water waves [30]. The wavemaker is capable of generating regular waves with a maximum wave height of 0.5 metres with a period of close to 2 seconds. In addition to unidirectional regular and irregular sea states, the individual paddle motion allows for directional spreading, as implemented for the focussed waves in Johannessen's experiments [1]. For simplicity, this study has only considered unidirectional waves, which runs parallel to the length of the wave tank.

At the opposite side of the wavemaker is a passive beach. This beach is constructed with perforated steel plates with an exponential profile asymptoting to a linear 9° slope at the waterline. The perforated steel plates allow water and waves to partially pass the beach before colliding with the end wall of the tank. At the same time, the passive beach forces a depth change, thus inducing breaking of waves and energy absorption. The passive porous beach dampens the waves at the far end of the wave tank, but small reflections can still be observed propagating in the opposite direction of the waves generated by the wavemaker. This reflection is only observable after a given time of wave generation, depending on the period of the waves generated. With the use of focused wave groups in this experiment, the reflection from the far end will not affect the measurements due to the given time of focus and the size of the individual frequency components when they reach the far end of the wave flume.

3.2.2 Experimental setup

Six resistance-type wave gauges were used to measure the time history of the different wave events. As some of the presented wave cases are reconstructions of previous experiments, the position of the six wave gauges is defined based upon Johannessen's experimental setup. The distance from the wavemaker and the distance between the wave gauges have been scaled up according to the respective water depth in the current test facility and Johannessen's facility. This gives a Froude geometric scaling factor of 1.833, which is applied to distances, time and frequencies throughout the thesis according to the laws of Froude-scaling [31]. Table 3 lists the positions of each wave gauge for both the present and previous experiments, as measured from the wavemaker.

Table 3: Longitudinal distance from the wavemaker for wave gauges in the present and previous experiments.

	Johannessen (1997)	**Present Study**
Wave gauge 1	4.80 m	8.80 m
Wave gauge 2	5.20 m	9.53 m
Wave gauge 3	5.50 m	10.08 m
Wave gauge 4	6.00 m	11.00 m
Wave gauge 5	6.30 m	11.55 m
Wave gauge 6	6.70 m	12.28 m

All of the wave gauges are positioned at the centre of the tank as illustrated in Figure 6. The towing carriage, which runs in the length of the tank, has been used to assemble the gauges. With this setup, the whole measurement area can easily be shifted up and down in the length direction of the wave flume while keeping the distance between the wave gauges constant.

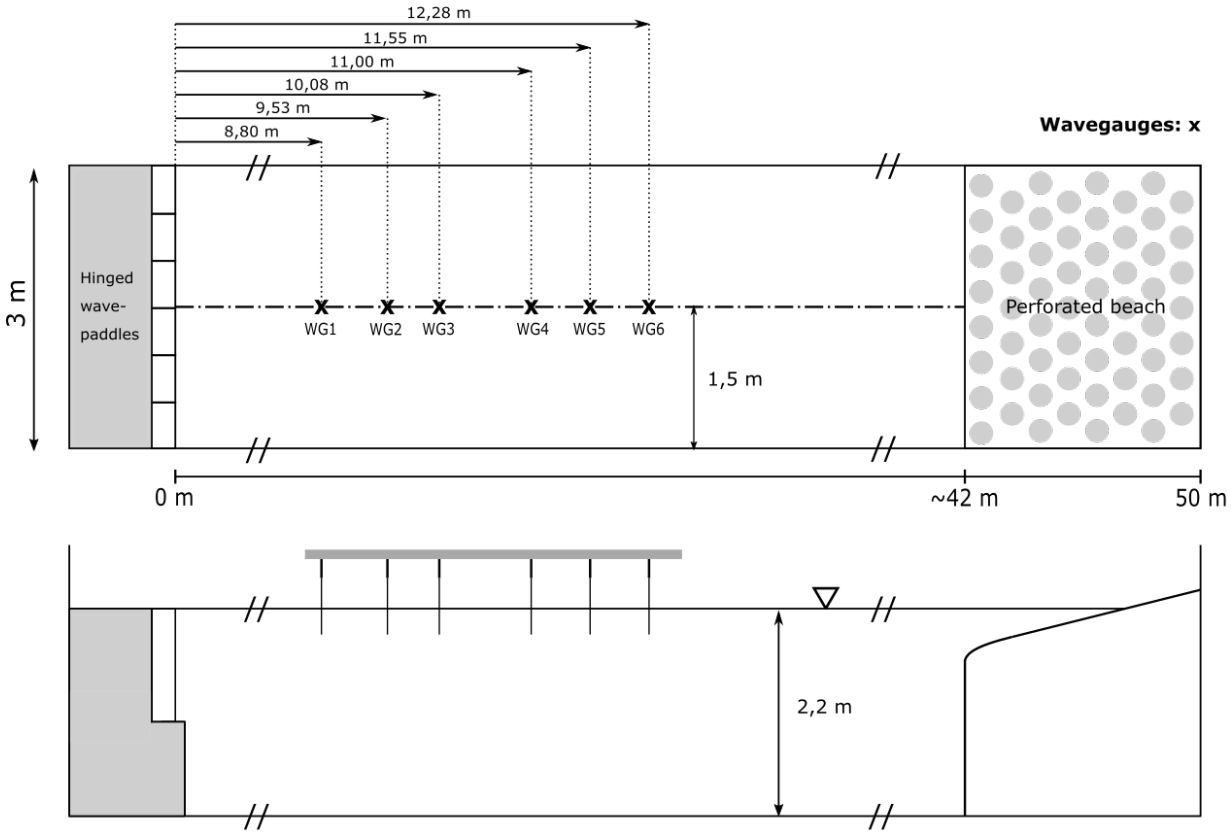

Figure 6: Experimental setup with wave gauges indicated with **X**.

The wave gauges used in the present study are provided by Edinburgh Designs and consist of a pair of parallel rods which are immersed in the water. The water conducts electricity between the two rods, so as the water level moves up and down, so does the circuit's conductive length, hence the resistance. The resistance in the circuit will, in turn, produce a voltage that can be linearly associated with the change in depth, allowing accurate tracking of the water surface with a sampling rate of 128 Hz. The probes are simple, low-cost and work well in large arrays [32]. However, one disadvantage is that the wave gauges experience relatively high hydrodynamic loads, particularly under large amplitude waves, which causes bending of the wave gauges, affecting their measurement accuracy.

The wave gauges can be calibrated using the same software that controls the wavemaker. This setup, which can be seen in Figure 7, enables the wave gauges to be synchronised with

the wavemaker, which in turn reduces hardware errors and uncertainty regarding the elapsed time in the wave event being measured. In all the experimental cases conducted in this study, the wave gauges have been configured to start and stop recording whenever the wavemaker receives the start or stop signal from the control software.

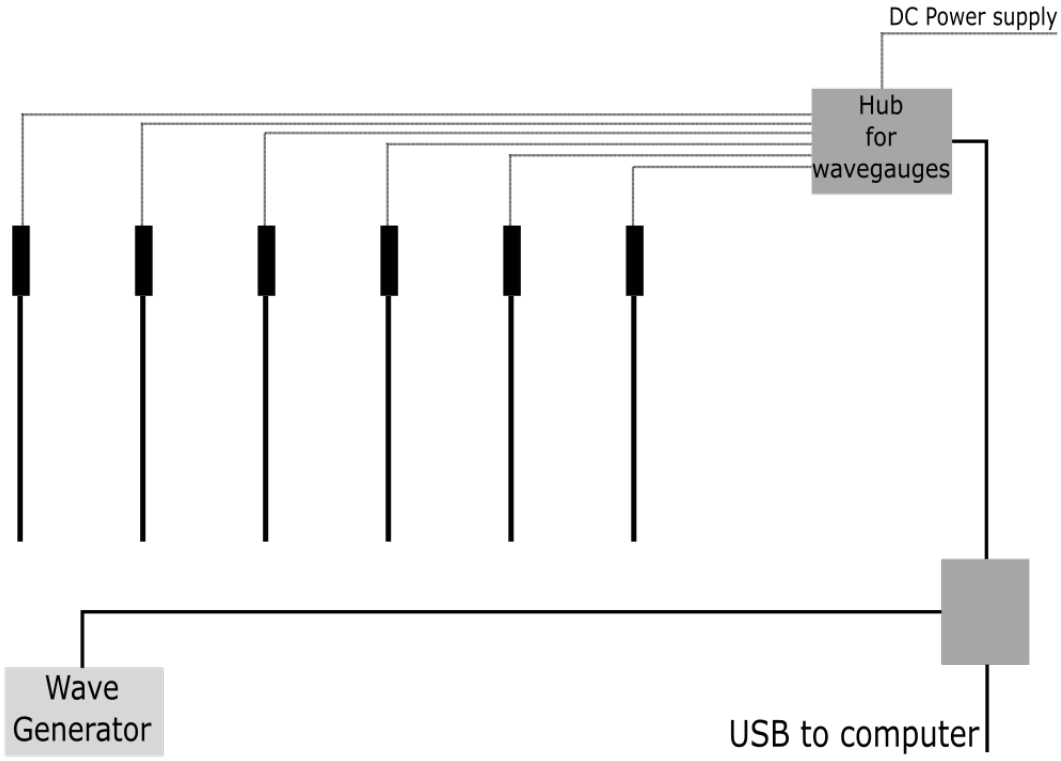

Figure 7: Wave gauge setup showing how the gauges are linked to the wave generator and vice versa.

The wave gauges were calibrated several times during the experimental campaign. With the configuration shown in Figure 7, the calibration can easily be done within the wavemaker control software. This process was conducted using three manual calibration points with a known distance between them. First, the wave gauges were immersed to their lowest setting, which was set to be equivalent to a surface elevation of 0.25 metres. Then, with the water surface calm and the wave probe in position, the resistance was measured and averaged over a period of three seconds. Following this, the wave gauges were raised 0.25 metres, equivalent to the still water level, before the resistance measurements were repeated. Finally, the wave gauges were raised to their maximum, equivalent to a surface elevation of

negative 0.3 metres with respect to the defined working depth. Resistance measurements were once again conducted, and the linear gain for the wave gauges was determined. With this procedure, the wave gauges were calibrated with a measurement range of 0.55 metres. Knowing that the listed measurement error for the wave gauges is 0.1 % of the full-scale measurement range gives an uncertainty of $\pm$ 0.55 mm for the measurements conducted in the following experiments. The linear offset value determined during calibration was reset before each wave run. Doing this ensured that the still water level would equal zero in all experiments, even if the water level in the tank had slightly decreased due to evaporation or spilling. The re-zeroing procedure also eliminates the possibility of zero-drift, which the wave gauges could potentially experience over time.

3.2.3 Test matrix and wave runs

The following section will introduce the different wave cases investigated in the present study. As discussed, a portion of the experimental investigation will aim to recreate some of the wave cases examined by Johannessen and Baldock et al. [1, 24]. This thesis has focused on the narrow banded spectrum D and the broad-banded spectrum B. Together, they account for nine individual wave events with different amplitude and frequency range. Table 4 summarises the six uni-directional D-cases and the three uni-directional B-cases conducted in the experimental campaign.

Table 4: Test matrix for reproduced wave cases DUD and BUD. The target amplitude is obtained from linear theory, and the number of frequency components that make up the given spectrum is listed.

Spectrum	**Spectral shape**	**Frequency range [Hz]**	**N. components**	**Amplitude [mm]**
D	$a_n \propto f^{-2}$	$0.6116 \leq f \leq 0.9232$	28	36.67
				73.33
				100.83
				111.83
				115.50
				121.00
B	$a_n \propto f^{-2}$	$0.5308 \leq f \leq 1.2232$	61	36.67
				73.33
				95.33

In addition to the recreated wave events in Table 4, two wave events defined by a JONSWAP spectrum will be investigated. Given that this thesis aims to create a database of surface measurements, it is relevant to include waves conditioned on a JONSWAP spectrum, as the JONSWAP definition is used widely for wave modelling in the North-Sea region. Contrary to the wave events described in Table 4, the two JONSWAP wave events are defined with significant wave height, H_s, and peak period, T_p. Furthermore, the JONSWAP wave events

are defined for the whole available frequency range for the wave generator, between 0 Hz and 2 Hz. The frequency range and the spectral shape distinguishes the JONSWAP wave events from the truncated spectra D and B. Table 5 summarises the JONSWAP wave events investigated in the following experimental campaign.

Table 5: Test matrix for the JONSWAP wave events investigated in the experimental campaign.

Wave case	**Peak period [s]**	**Significant wave height [m]**	γ
$H_s = 0.0326$ m, $T_p = 1.55$ s	1.55	0.0326	3.3
$H_s = 0.0326$ m, $T_p = 2.20$ s	2.2	0.0326	3.3

The parameters used to define the JONSWAP wave events are taken from a 50-year contour plot created with hindcast data for a specific location at the Doggerbank with a water depth of 80.6 metres [33]. The water depth at the given location, and the water depth of the wave tank present at HVL, corresponds to a scaling factor of 36.6 between the hindcast data and the model test. With the parameters defined in Table 5 and the aforementioned scaling factor, the wave events in the experimental campaign would correspond to a sea state with a significant wave height equal to 1.20 metres and with a peak period of 9.4 seconds and 13.3 seconds. Both of these wave events fall within the defined 50-year contour plot, indicating that these events represent actual sea states present at the Doggerbank location [33]. However, these two sea states represent calm weather conditions and are not representative of the mean occurrence. Nevertheless, the calm sea state ensures that no wave breaking occurs during the experimental testing of the JONSWAP events.

Table 6: Focal time and focal position for the different wave groups.

Wave group	**Focal time [s]**	**Focal position [m]**
DUD	20	8.8
BUD	20	10.08
JONSWAP	20	11.00

As all of the wave events listed in Table 4 and 5 are focused irregular wave events, each wave event is associated with a given focal location in space and time. Table 6 introduces the different focal positions and focal time for each group of wave events.

3.2.4 Generating input to wave generator

There are several ways of defining a wave event in the Njord wave software used in the wave laboratory at HVL. The one method used in the present study is to upload a spectrum table, which can be defined either with frequency and energy or frequency and amplitude. The latter being the case in the following experiments. To generate the wave generator input needed to recreate the experiments conducted by Baldock and Johannessen [24, 1], the exact same input must be generated before scaling to fit the dimensions of the HVL wave tank. The following section describes how the generation of wave input for the DUD37 wave event was conducted. The process is identical to what has been used in the BUD wave cases, but the frequency range has naturally been changed for the broadband BUD events.

Furthermore, the scaling factor used for scaling the previous experiments to MarinLab is calculated as the ratio of the water depths of the two tanks, i.e. $\lambda_s = 2.2/1.2 = 1.833$.

Define frequency range

Johannessen defined frequency range for the events within spectrum D in the way described by Equation (3.1). Here, the numerator represents a whole number that controls how many frequency components are included in the given range. The denominator represents the spectral repeat time and is equal to 64 seconds in Johannessen's experiments.

$$\frac{53}{64} \leq f \leq \frac{80}{64} \tag{3.1}$$

By defining frequency range as in Equation (3.1), the frequency steps are automatically bounded by the spectral repeat time, which is important considering frequency resolution error and the limits of the wave generator. For the wave generator at HVL, frequency

increments must match the spectral repeat time defined in the Njord wave software. Using the scaling factor of 1.833 and the Froude scaling laws, the spectral repeat time for the present experimental investigation is determined to be approximately 86.6 seconds. Defining the frequency range as in Equation (3.1) with the new and scaled up spectral repeat time yields the following:

$$\frac{53}{86.6} \leq f \leq \frac{80}{86.6}$$

The whole number in the numerator has not been changed in order to bind the frequency increments to the spectral repeat time. Practically, the new and scaled up frequency range is similar to the one in Johannessen's experiments. However, the individual components are shifted towards lower frequencies with a factor of $1/\sqrt{\lambda_s}$, according to Froude scaling.

The same procedure is applied when defining the frequency range for the BUD wave events. However, in the BUD events, the whole number in the numerator is changed from 53 and 80 to 46 and 106, respectively. This gives a broader frequency range of 61 individual frequency components compared to the 28 components in spectrum D.

Define spectral shape and amplitude

With the frequency range defined, the spectral shape can further be determined. The spectral shape in Johannessen's experiments was defined as $a_n \propto f^{-2}$. This expression states that each frequency components is inversely proportional to the square of the frequency. In order to define the spectral components given the requirements of the spectral shape, Equation (3.2) and (3.3) are used.

$$a_n = (2\pi f_n)^{-2} \tag{3.2}$$

$$A_n = \frac{a_n}{\sum a_n} \cdot A_{max} \tag{3.3}$$

First, Equation (3.2) is used to define a value for each frequency step that follows the re-

quirements of the spectral shape. Secondly, Equation (3.3) is used to normalise the values for each frequency step before they are multiplied with the target amplitude for the given wave event. This method will generate 28 individual spectral components which follow the defined spectral shape, and the sum of all the components will equal the target amplitude defined as A_{max}. In the case of DUD37, A_{max} is equal to 0.03667 metres, and for the other DUD events, this is the only parameter that changes when the wave input is defined.

Final input format

All the wave events conducted in the experimental study are defined using a spectrum table in the Njord Wave Synthesiser software. Keeping the frequency range constant for each wave event within a given spectrum, the difference between the wave events are the amplitudes calculated with Equation (3.3). Table 7 displays the ten first spectral components for DUD37 (a) and DUD112 (b). Calculating the spectral components in MATLAB offers the possibility of saving the variables in a CSV-formatted table that can be directly uploaded into the Njord software.

Table 7: Wave generator input data for wave event DUD37 and DUD112

(a) DUD37

Frequency [Hz]	Amplitude [m]
0.6116	0.001970
0.6232	0.001898
0.6347	0.001829
0.6462	0.001764
0.6578	0.001703
0.6693	0.001645
0.6808	0.001589
0.6924	0.001537
0.7039	0.001487
0.7155	0.001439

(b) DUD112

Frequency [Hz]	Amplitude [m]
0.6116	0.006009
0.6232	0.005789
0.6347	0.005580
0.6462	0.005382
0.6578	0.005195
0.6693	0.005018
0.6808	0.004849
0.6924	0.004689
0.7039	0.004536
0.7155	0.004391

The JONSWAP wave events are defined using Equation (2.15) from Section 2.4. Furthermore, supervisor David Lande Sudall has provided a MATLAB script that generates the spectral energy density for a given set of input parameters. The MATLAB code uses a given frequency range as input to define the spectral energy density within. With the limitations of the wave generator in mind, this range is set to be from 0 Hz to 2 Hz. As with the truncated wave events, the frequency increments are specified as the inverse of the spectral repeat time. In addition, significant wave height, H_s, peak period, T_p, and spectral peakedness parameter, γ, found in Table 5, are defined as separate inputs to the script. The resulting output from the MATLAB code consists of frequency and spectral components which make up the spectral energy density curve.

$$A_n = \sqrt{2S_n\Delta f} \tag{3.4}$$

With the spectral components corresponding to a given wave event, Equation (3.4) can further be used to translate spectral energy density components into amplitude components. The variables are saved in a CSV-formatted table before being uploaded as a spectrum table in the Njord software.

3.2.5 Calibration of wavemaker

This project aims to develop a database containing highly accurate surface measurements of different wave events. Before this can be done, it is of utmost importance to calibrate the wavemaker to ensure that the irregular wave groups generated at the location of measurement correspond to the prescribed input wave. Although, only in the case of low amplitude wave groups where linear behaviour is expected. Therefore, a significant portion of the time during experimental testing was dedicated to the calibration of the wavemaker. The goal of the calibration was to define a unique transfer function to each specific frequency range. The same transfer function would be used for every wave event defined by the same frequency range or peak period. Hence, one transfer function was generated for the DUD events, one

for the BUD events and finally, two separate transfer functions for the JONSWAP events specified to each peak period.

The calibration process used in this study can be divided into seven different parts, which will be described in the present section, and progresses as follows:

1. Use the wave input defined for the lowest amplitude case, where linear behaviour is expected, and conduct the wave run.
2. Use the measurements from the wave run and compare the calculated energy content with the target spectrum.
3. Create a gain correction transfer function and apply it to the input file before conducting a new wave run.
4. Check the measurements and energy content in the new wave run and repeat step 2 and 3 until the measurements are seen to agree well with the theoretical spectrum.
5. Now, use the measurements from the last wave run and calculate if the phases are correct with respect to a linear time series.
6. Compare target amplitude and measured wave amplitude in the wave group focus point, and perform minor gain adjustment to the transfer function to obtain the correct amplitude.
7. Save the transfer function.

Correction of spectral energy density

As the wave cases are defined with amplitude components, the theoretical energy spectrum can be determined using Equation (3.4) which states the relation between energy spectrum and amplitude spectrum. Hence, the first calibration method used for the wave events is energy spectral density calibration. This process is conducted using the MATLAB script provided by supervisor Øystein Lande to compute the energy content of each frequency

component. This MATLAB code uses a Fast Fourier Transform to extract the details about spectral energy. For more details about this MATLAB routine, check Appendix A.1.

Clearly, the first wave run, seen in Figure 8a, does not match the theoretical target spectrum marked by a solid black line. To calibrate the case displayed in Figure 8a, each frequency component was compared to its respective theoretical component. For most of the 28 components, the measured energy content was lower than the theoretical target. However, some of the frequency components' energy output was calculated to be higher than the theoretical target. Furthermore, the theoretical components were divided by the measured components, and a gain correction for each frequency component was determined. These 28 individual gain corrections were applied to the theoretical wave input, and the spectral energy for the new resulting wave run can be seen in Figure 8b.

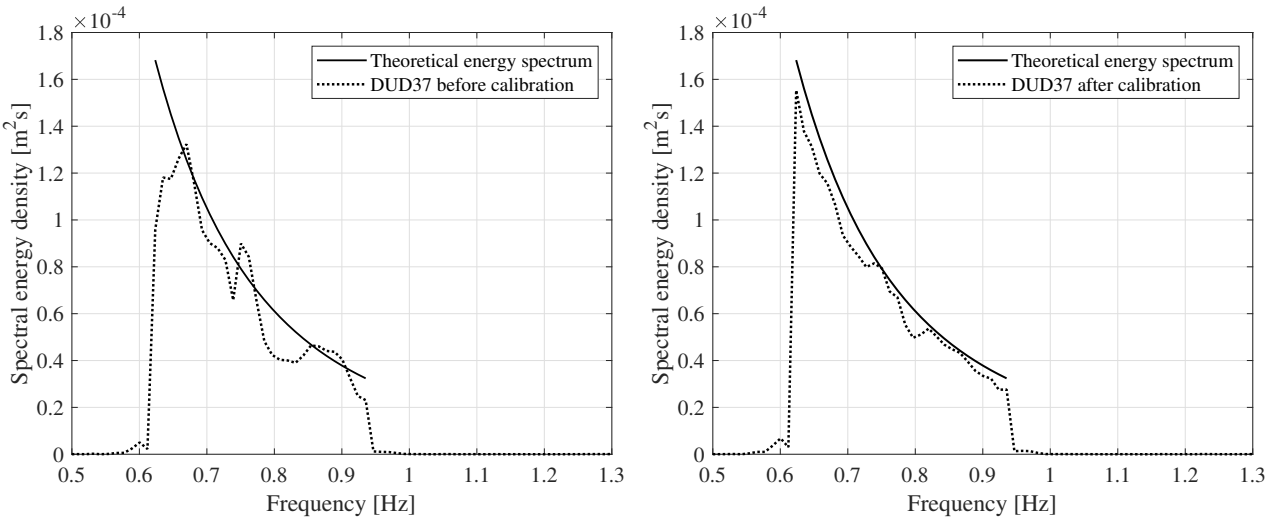

(a) DUD37 before calibration

(b) DUD37 after calibration.

Figure 8: Spectral energy density calculations for DUD37 before and after calibration.

When comparing the two situations in Figure 8, the impact of the applied gain correction becomes apparent. After the applied gain correction, the new measured energy spectrum exhibits a smoother transition from the top of the spectrum towards the maximum cut-off frequency. The fluctuations are smoothed out, and the overall peak is increased to match the theoretical peak. Notably, all the frequency components in the measured spectrum in Figure 8b demonstrate lower spectral energy content compared to the theoretical target spectrum.

As Figure 8b displays the energy content from the final calibrated time series, the amplitude correction process has been included, and the energy content for the whole spectrum has been reduced to match the linear target amplitude.

Furthermore, the gain corrections for each frequency component is calculated by comparing the theoretical energy content with the measured energy content. However, the input to the wave generator is defined with amplitude and not energy. This introduces a possible error in the transfer function as the gain correction applied is linear. At the same time, the relation between amplitude-component and energy-component is not linear, as defined in Equation (3.4). Therefore, the individual gain corrections for each frequency component is applied to the energy components before they are calculated to amplitude components and given as input to the wave generator.

Phase correction

All of the focusing events have a specific focal position both in time and space. This given location is defined in the software used to design the wave events. The software will calculate the phase for each wave component such that every component will experience a maximum at the given location. With this setup, there is no need to specify the phases for each wave component. However, it is advantageous to check if the measured phases for each frequency component match the theoretical phase specified by the software. If the phasing of the wave event is done incorrectly, the frequency components will not superimpose at the target location, and the focused wave group will not reach its maximum.

To check if the phases are correct, a MATLAB script generated by supervisor David Lande-Sudall has been used to compute the Fourier coefficients of the measured time series. The coefficients, a_f and b_f, which were found using the prior mentioned MATLAB script, fit a Fourier series of the sine-cosine form given by Equation (3.5), where P is the length of the analysis interval, i.e. the period of the Fourier series.

$$\eta_f(x) = \frac{a_0}{2} + \sum_{n=1}^{\infty} \left(a_f \cos\left(\frac{2\pi}{P} nx\right) + b_f \sin\left(\frac{2\pi}{P} nx\right)\right) \tag{3.5}$$

However, in order to determine if the phases in the measured time signal is correct, the Fourier series needs to be transformed from the sine-cosine form and into the amplitude-phase form. This can be achieved using the trigonometric identity in Equation (3.6), and the definition $A_f = \sqrt{a_f^2 + b_f^2}$ and $\varphi_f = \arctan 2(b_f, a_f)$.

$$A_f \cdot \cos\left(\frac{2\pi}{P}nx - \varphi_f\right) = \underbrace{A_f \cos(\varphi_f)}_{a_f} \cos\left(\frac{2\pi}{P}nx\right) + \underbrace{A_f \sin(\varphi_f)}_{b_f} \sin\left(\frac{2\pi}{P}nx\right) \tag{3.6}$$

The sine and cosine pairs can now be expressed as a single sinusoidal with a phase offset and amplitude as shown in Equation (3.7), which is the same form as required by the wavemaker software. Note that the Fourier series is now expressed as a function of t rather than x like in Equation (3.5). To check if the calculations are done correctly, the time series can be recomposed and plotted using the amplitude-phase form of the Fourier series. This should yield an identical representation of the measured time series.

$$\eta_f(t) = \frac{A_0}{2} + \sum_{n=1}^{\infty} A_f \cos(\omega t - \varphi_f) \tag{3.7}$$

The phase for each frequency component, φ_f, can now easily be obtained. If the same procedure is conducted for a linear time series, the measured phase can be compared with the theoretical. For example, in Figure 9, the measured phases from the DUD37 event are compared to the phases extracted from the linear time series of DUD37.

Almost all of the calculated phases from the measured time series are shifted slightly above the theoretical phases, except the final frequency component, which is approximately equal to the theoretical phase but with a negative value. For the last frequency component, the negative phase value would have no practical impact as the difference compared to the theoretical is almost equal to 2π, in other words, a full wavelength. Furthermore, the deviations observed for the remaining frequency components are almost constant. However, when positioning the wave gauge, a minor position error will cause an overall phase shift in the measured time

series compared to the linear. Hence, misalignment of the wave gauge can explain why all the phases for the measured frequency components slightly deviate from the theoretical in Figure 9.

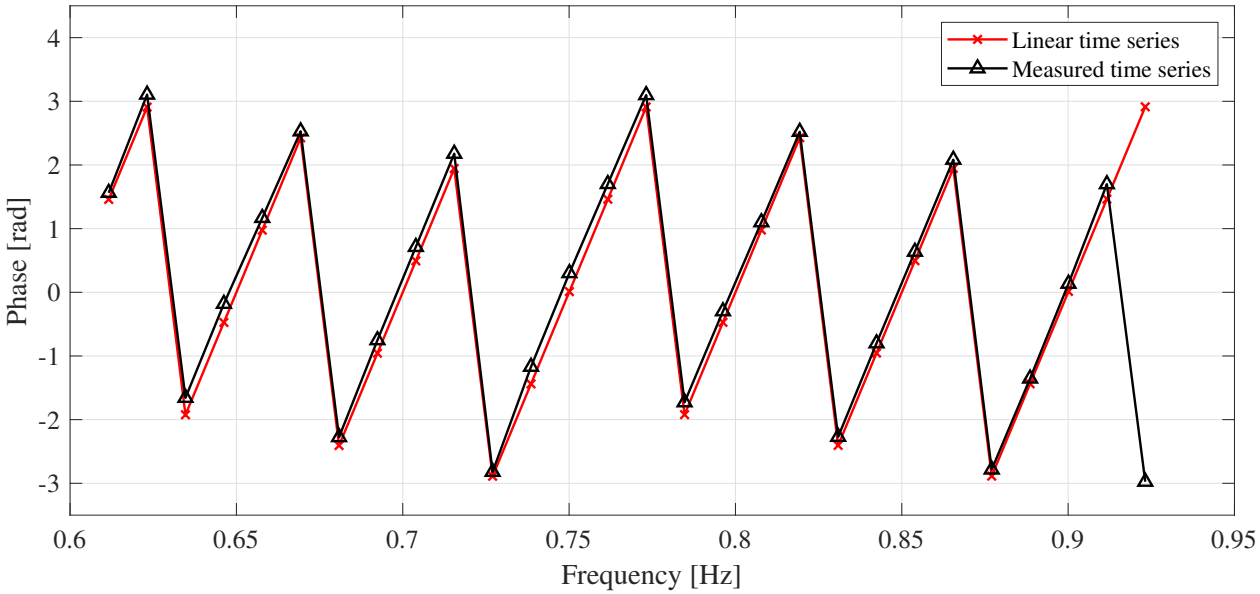

Figure 9: Calculated phases for each frequency component in both measured time series and linear time series of DUD37.

During the experimental testing, several ways of calibrating the wave events were investigated. Controlling if the phases were correct was initially a step prior to the energy calibration. When investigating the phases for a wave event that had not been calibrated in terms of spectral energy density, it was observed that the phases did not match the theoretical target. However, when investigating the phases after the spectral energy density calibration, it was found that the gain correction applied to the frequency components amplitude also corrected the phases. This finding resulted in a new order when conducting the calibration of the wave events, and spectral energy calibration was performed before the phase correction for every wave event. As can be seen, in Figure 9, the phase of each frequency component in the measured DUD37 event fits well with the target phases generated from the linear time series. Therefore, no further considerations were taken into correcting the individual phases with a gain correction, and the phase calculations done by the wavemaker software were considered precise.

Amplitude correction

When the spectral energy content and the phases are checked and corrected, the final step in the calibration process can be started. For the low amplitude wave events, where linear behaviour is expected, the amplitude in the measured time series should equal the target amplitude. DUD37 is assumed to be linear, and the target amplitude of 36.67 mm is what should be expected from the measured time series. However, the first time series measured after the energy calibration showed a measured focal peak higher than the target peak. To correct the amplitude, a gain correction was applied to all the frequency components. By applying the same correction to all of the components, the relationship between the frequency components will not be affected. The overall energy content in the wave run is practically shifted up or down depending on the measured amplitude.

The DUD37 case obtained a higher measured amplitude than the target amplitude. Hence, several new attempts, with gain corrections between 0.9 and 1, were conducted until the measured amplitude was equal to the target amplitude. The same procedure was used in the BUD37 case, as this wave event is also considered linear. However, this step was not included when calibrating the two JONSWAP events as none of them can be considered to be linear.

Final transfer function

With the energy content, phases and amplitude corrected, the final transfer function is extracted. By comparing the theoretical input used in the first wave run and the final input used in the last wave run after amplitude correction, the transfer function is easily obtained. Dividing the mentioned inputs will give the effective gain correction for each frequency component. Figure 10 shows the two different transfer functions generated for the DUD and BUD events.

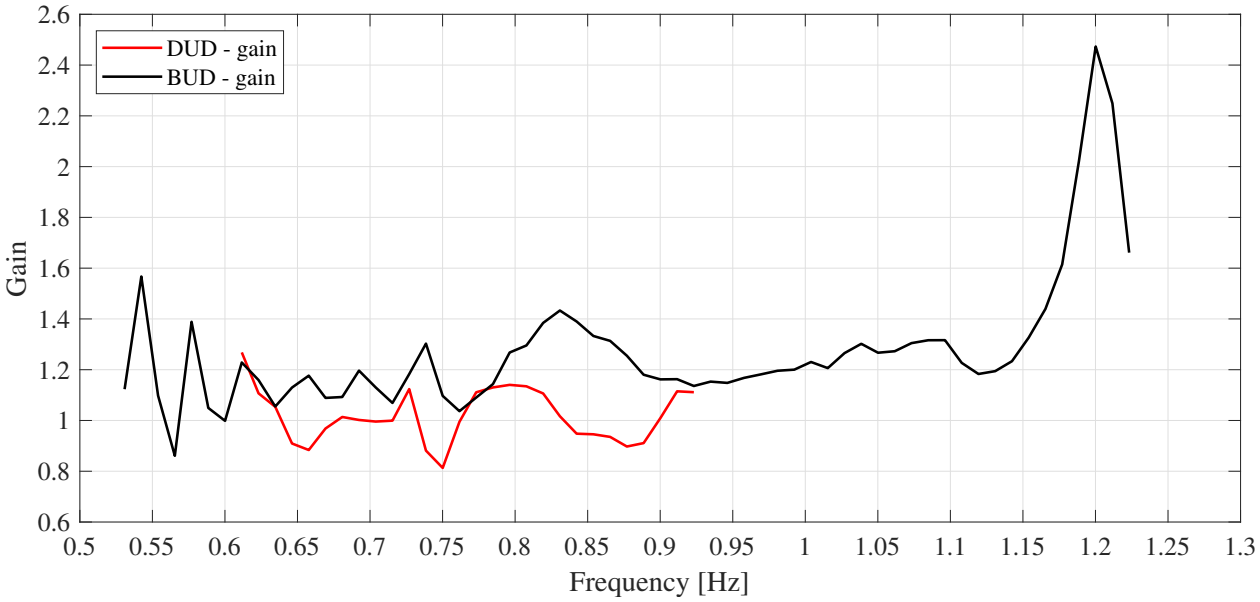

Figure 10: Gain corrections applied for frequency components in both DUD and BUD wave cases.

Both of the transfer functions act relatively similar in the shared frequency range. However, the BUD transfer function consists of higher gain corrections compared to the DUD transfer function. Furthermore, the BUD transfer function reaches a maximum gain correction of approximately 2.5 towards to higher frequency area. The cut-off frequency observed in the uncalibrated BUD37 time series was lower than the desired cut-off frequency of approximately 1.23 Hz. Hence, the transfer function for the BUD events exerts a relatively high gain on the last frequency components to shift the cut-off frequency higher and towards the target of 1.23 Hz.

3.2.6 Sources of uncertainty

Results obtained from experimental testing will always be associated with some degree of uncertainty. The following section highlights some of the primary sources of uncertainties associated with the current experimental campaign. Some of the sources for uncertainty can more or less be eliminated in advance of the experimental tests, such as making sure the wave gauges are calibrated prior to the tests. However, some of these sources have been identified during the testing and are therefore defined as the primary sources of uncertainty regarding the experimental results.

The primary sources of uncertainty that are identified are listed as following.

1. Manually measuring the distance between the wave gauges with a measuring tape.
2. Tank water containing old seeding particles which gathered on the wave gauges.
3. Effects caused by the side walls of the wave tank.
4. Frequency resolution error associated with frequency increments and spectral repeat time.

Distance between wave gauges

When the experimental setup was assembled, the distance between the wave gauges was measured using a measuring tape. Wave gauge number one, positioned at 8.8 metres, was the first wave gauge installed. After that, the following wave gauges were mounted using the previous wave gauges as a reference and the known distance between them. This particular way of mounting the wave gauges introduces a possibility that the measurement errors will escalate from the first wave gauge and all the way to the last wave gauge.

When investigating the results from the measurements, there is no indication that the measurement error has escalated for each wave gauge. However, when comparing the previous results of Johannessen and the present, some discrepancies are found for all the wave gauges.

It is believed that the distance between the wave gauges in Johannessen's setup was measured to a much more accurate extent, thus, leading to the conclusion that the discrepancies are caused by inaccurately measuring the distance between the gauges. In hindsight, a laser measuring tool positioned at the first wave gauge should have been used to measure the distance between the gauges.

It is challenging to quantify the impact of this effect in terms of percentage error. As the wave gauges are coarsely spaced, there is no way of knowing the actual wave height between the gauges. Nonetheless, the error associated with the position of the wave gauge would yield the most significant impact on the largest wave events, where strong nonlinear behaviour is present and rapid growth of the crest occurs.

Unwanted particles in the tank water

The wave tank at HVL is used for several different research projects, and many of them use Acoustic Doppler Velocimeter (ADV) or other forms of particle tracking tools. Common for particle tracking tools is the need for seeding particles in the water. As many of the projects need these seeding particles, and the cost of seeding material is high, the wave tank has not been cleaned, and the water has not been changed in between different projects.

After periods of inactivity, the seeding material floats and gathers on the water surface in patches, further depositing a fine layer on the wave gauges as observed in the wave tank at HVL. As a result of surface tension and capillary forces, these patches gather around the part of the wave gauge which pierces the water surface. With distortions of the water surface, these particles stick to the probes and form a band of seeding particles with length proportional to the wave height. This can be seen in Figure 11 where two wave gauges are photographed.

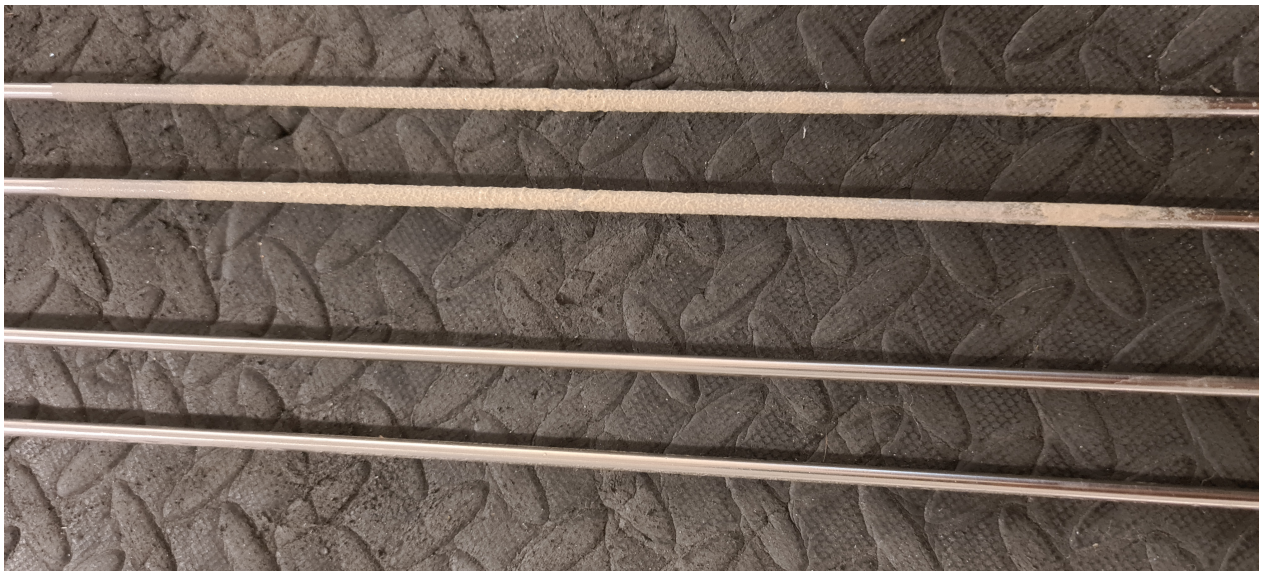

Figure 11: Two different wave gauges with the upper wave gauge showing how the seeding particles have gathered on the probes near the water surface.

As a result of these particles gathering on the wave gauges, the wave gauges were wiped clean at least one time each day. However, there are uncertainties associated with how the formation of these particles affects the measurements collected from the wave gauges. Furthermore, a reasonably sizeable regular wave event was run once a day to facilitate a rough cleaning of the wave gauges. The regular wave train was run for approximately 5 minutes to break up the formation of patches at the water surface and remove some of the particles from the wave gauges.

Side wall effects

When recreating experiments conducted in a wide wave basin, the effects of the tank wall in the narrow wave tank at HVL has to be mentioned. Friction forces between the water and the concrete walls will drain energy from the waves, and in an infinitely long wave tank, the wave would eventually dissipate. However, with the measurement area being a maximum of 12.3 metres away from the wave generator, it is uncertain how much the friction forces will affect the measured energy content of the sea state. To reduce the friction forces present on the tank walls, the same regular wave train used to wash the wave gauges is used to wet the tank walls. This will reduce the friction forces throughout the length of the wave tank.

Another phenomenon that can affect the measurements is reflections from the side walls. The width of the wave tank is 3 metres, and a small cross-tank wave with a wavelength equal to an integer of the width would effectively act as a stationary wave, thus proving hard to dampen out. Furthermore, a wave with a wavelength of 3 metres is, by linear wave theory, equal to a wave with a frequency 0.72 Hz. This is known as the cross-tank frequency. Reflected waves from the side walls with this particular frequency will resonate and generate an energy contribution at the frequency area around the cross-tank frequency.

From investigations into the spectral energy density, a small peak around 0.75 Hz can be seen. This can be observed in both Figure 8a and 8b. The transfer function for each wave group contributes to the dampening of this effect. However, the reflective waves can not be removed without using a wave/energy absorber in the cross-tank direction.

Frequency resolution error

The frequency resolution, or frequency increments, are determined by the spectral repeat time for the given wave events, thus defined by Equation (3.8). Here, T_{dur} represents the spectral repeat time, while i_n denotes the integer introduced in Equation (3.1), and N is the total number of samples.

$$\Delta f = \frac{i_{n+1} - i_n}{T_{dur}} \qquad i_n = 0, 1, 2, 3, ..., N-1 \tag{3.8}$$

In the Discrete Fourier Transform (DFT) process, which is the process used to calculate the spectral energy density of the time series, the time series is correlated with sinusoids whose frequencies are integer multiples of the inverse of the sampling duration, or spectral repeat time [34]. Hence, if the time series is sampled for a duration of T_{dur}, it will be correlated with sinusoids of frequencies given by Equation (3.9).

$$f_{DFT} = \frac{i_n}{T_{dur}} \tag{3.9}$$

Scaling the spectral repeat time from Johannessen's experiments, where the spectral repeat time was 64 seconds, a decimal error is introduced in the frequency resolution. The new and scaled up spectral repeat time is approximately 86.66 seconds. However, when performing the scaling calculation, which is defined as $T_{scaled} = T_{orig} \cdot \sqrt{\lambda_s}$, the resulting spectral repeat time is given with 15 decimals. This is no problem in terms of calculations in MATLAB as the whole number is used as a variable, but the process of calibrating the wave generator is affected.

The command signal sent to the wavemaker is computed by Inverse Discrete Fourier Transform (IDFT), and therefore, the frequency components will match the defined spectral repeat time. However, the wave generator software cannot define a spectral repeat time with 15 decimals and uses the rounded number of 86.65625 seconds. This slight discrepancy between the spectral repeat time of the wave generator, and the scaled-up experiments, introduces a problem when the gain correction for the different frequency components are generated. The effect of this deviation can be described mathematically in the following way:

$$T_{DFT} \neq T_{WG}$$

$$f_{DFT} = \frac{i_n}{T_{DFT}} \neq \frac{i_n}{T_{WG}} = f_{WG}$$

$$f_{DFT} \neq f_{WG}$$

Clearly, with the different definitions of the spectral repeat time, the frequency increments for the calculations and the wave generator becomes different. Furthermore, the input components defined in the wave generator software will not be identified correctly by the wave generator. In other words, the gain correction applied to the spectral component is applied to frequencies that the wave generator cannot identify. However, the difference between the target frequencies and the frequencies identified by the wave generator are minor, meaning that the gain correction is still effective. However, if the process of applying a gain correction is repeated several times, the resulting energy spectrum will become *spiky*, and the deviations will grow for each repetition. This results from the gain correction being applied to

an adjacent frequency rather than the frequency intended. Further attempts to correct this deviation will therefore only increase the deviation, thus giving a *spiky* energy spectrum.

In hindsight, the scaled-up frequency range should have been slightly altered such that the spectral repeat time for both the wave generator software and the DFT calculations were equal. This would, in turn, mean that the scaling of previous experiments would not follow the exact rules of Froude scaling. When both definitions of the spectral repeat time are equal, the calibration steps described in Section 3.2.5 can be performed multiple times without experiencing frequency resolution errors. Therefore, it is of utmost importance that the definition of spectral repeat time is consistent for future investigations involving wave generator calibration.

3.3 Numerical approach

The following sections will give a brief introduction as to how the numerical simulations were conducted and the theory behind the applied CFD code. As this thesis mainly focuses on the experimental result and the accuracy of the wave generation, the numerical simulations of the wave groups in this thesis will serve as an example of how the experimental measurements can be used. The numerical tool used in the present study is an open-source code called Basilisk. The code used to simulate the wave tank in MarinLab is provided by external supervisor, Øystein Lande. It has been edited to resemble the experimental setup described in Section 3.2.2. This CFD code, *waveflume.c*, is found in Appendix A.2.

3.3.1 Wave flume code

Basilisk is an open-source library of partial differential equation solvers for various types of meshes. The solver utilised in the present thesis is the two-phase flow Navier-Stokes solver. The two fluids are separated using the finite volume, Volume-of-Fluid method [35], and the surface is reconstructed at every time-step using a Piecewise Linear Interface Construction

(PLIC). Notable for the chosen code is that Adaptive Mesh Refinement (AMR) is used, which allows for high resolution where needed, and coarsening elsewhere, which improves calculation times and increases accuracy. In the case of wave propagation, the high mesh resolution is concentrated close to the free-surface.

The solver approximates numerically the incompressible, variable-density Navier–Stokes equation given by Equation (3.10). Equation 3.11 represents the continuity equation which is a statement for the conservation of mass, i.e. mass can not be created nor cease to exist.

$$\rho\left(\frac{\partial \boldsymbol{u}}{\partial t} + \boldsymbol{u}\nabla\boldsymbol{u}\right) = \nabla p + \nabla(2\mu\boldsymbol{D}) + \boldsymbol{a} \tag{3.10}$$

$$\nabla\boldsymbol{u} = 0 \tag{3.11}$$

$$\boldsymbol{D} = \frac{1}{2}\left(\nabla\boldsymbol{u} + (\nabla\boldsymbol{u})^{T_i}\right) \tag{3.12}$$

The Navier-Stokes equation is expressed with $\boldsymbol{u}$ being the fluid velocity vector, ρ the fluid density and μ the viscosity of the fluid. $\boldsymbol{D}$ is the deformation tensor defined as in Equation (3.12)[36]. Furthermore, the face field $\boldsymbol{a}$ in Equation (3.10) is defined as the acceleration term [36]. This term practically expresses additional external forces and is by default set to zero. However, in the simulations conducted for this study, both surface tension and gravity is included as external forcing terms within the Navier-Stokes solver.

Furthermore, a wave event conducted in the wave tank at HVL is a two-phase process with both air and water present. Hence, the Navier-Stokes equation is set up with an additional function that can describe the two-phase process, see [35]. For non-breaking and two-dimensional waves, air as an additional phase has no impact on the results or computational time. However, the CFD code used in the present numerical study has previously demonstrated excellent abilities to predict wave propagation, and with no impact on either results or computational cost, the two-phase function is also applied in the present numerical investigation. Consequently, the density of fresh water has been set to 1000 kg/m^3, and 1.225 kg/m^3 for air. The Navier-Stokes solver estimates velocity and pressure for each cell defined

by the mesh structure in the simulations and a surface profile for the free-surface defined by the interface of the two fluids.

The main code applies a combination of Dirichlet and Neumann boundary conditions on the top and left boundaries. These boundary conditions restrict the normal velocity at the surface, relative to the surface profile, to be zero. Also, the top boundary is defined with a constant pressure condition to avoid pressure buildup. This particular boundary condition avoids escalating back-circulating flows in the top boundary. Furthermore, the left boundary is where the wave kinematics are generated, and a Dirichlet boundary condition is applied here, where the horizontal and vertical velocity components are prescribed using the CFD-wavemaker library [37]. This library provides second-order irregular wave kinematics, which is especially important for generating steep waves where linear wave theory is inaccurate.

Table 8: Input parameters used to simulate the wave tank at HVL.

Input parameter	**Value**
Run time	30 seconds
Maximum Δt	0.1 seconds
Domain dimensions	50 m $\times$ 2.95 m
Depth	2.2 m
Gravitational acceleration	9.81 m/s^2
Density water	1000 kg/m^3
Density air	1.225 kg/m^3
Maximum refinement	13
Minimum refinement	6
Initial refinement	8
Number of threads	18

The simulations are only run for 30 seconds to save computational time, less than half of the run-time of 86 seconds used in the experimental wave cases. However, the run time was assessed to be adequate as the time of focus is set to 20 seconds, allowing the waves to pass the focal position well before the simulation was ended. Table 8 summarises the main input parameters used in the numerical simulations of the HVL wave tank.

3.3.2 Mesh generation

The CFD-simulations in Basilisk have been run using an Adaptive Mesh Refinement (AMR) implementation. This dynamic mesh generation enables a maximum level of refinement around the free-surface and can reduce the computational time significantly compared to a static grid [18]. A given level of refinement controls the mesh size, and in simulations conducted in this study, the minimum and maximum level of refinement are defined in the wave flume code. To illustrate this mesh structure, Figure 12 shows the two-dimensional structure of a tree-based grid, i.e. a quadtree [38].

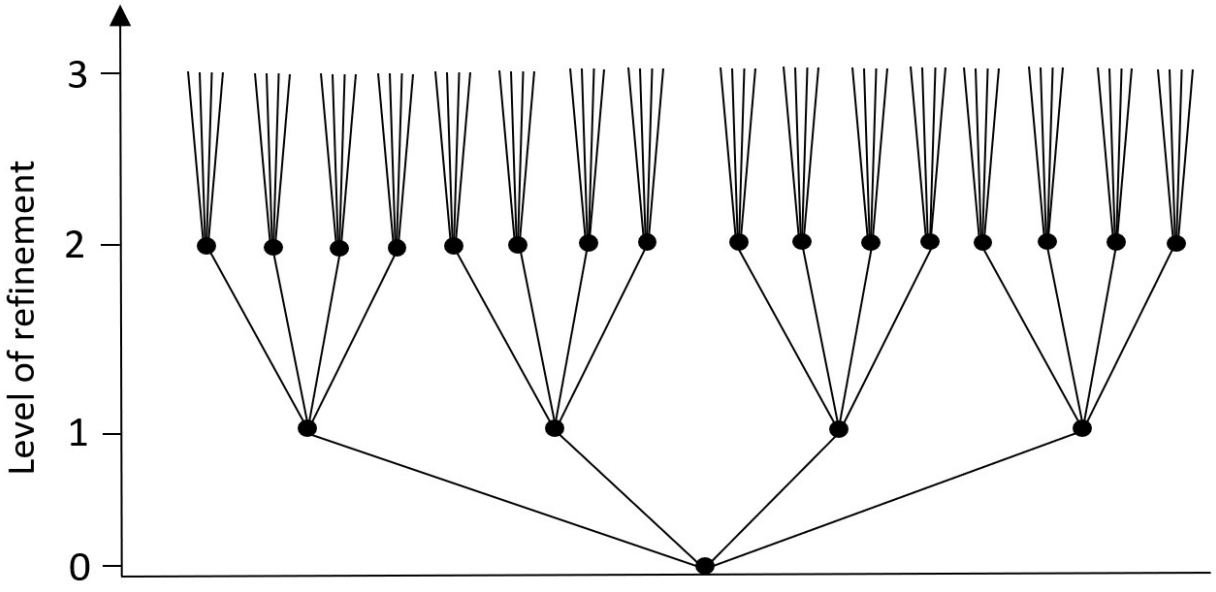

Figure 12: Tree structure illustrating how the mesh is divided into cells by adjusting the levels of refinement parameter.

Figure 12 basically describes a multi-resolution grid, which has no variable resolution on the spatial domain [39]. In a square domain with the levels of refinement defined as in Figure 12, the whole domain would be split into $2^3 \times 2^3$ cells, in other words, 64 cells. However, the tree-grid structure used in the simulations in this thesis has a variable resolution in the spatial domain. Hence, not all the cells in the domain need to be refined to the maximum level given. This can be thought of as a hierarchy where the four different cells on refinement level one are called parent-cells, and each of them having four children-cells on refinement level two. Each of the children-cells on refinement level 2 can again be called parent-cells, as each of them has four children-cells on refinement level 3 and so on. To achieve a variable resolution in the mesh structure, some of the parents at a given level will not have their children-cells initialised.

The Basilisk solver allows neighbouring cells in this tree based grid to vary up to one level of resolution and each level of refinement differs by a factor of two [38]. The main advantage of this setup is that the number of cells is significantly reduced. This can be seen in Figure 13 where Figure 13a represents the variable resolution, while Figure 13b represents the domain fixed to a level of refinement of three as in Figure 12. Figure 13a consist of 16 cells while the static grid in Figure 13b consists of 64 cells.

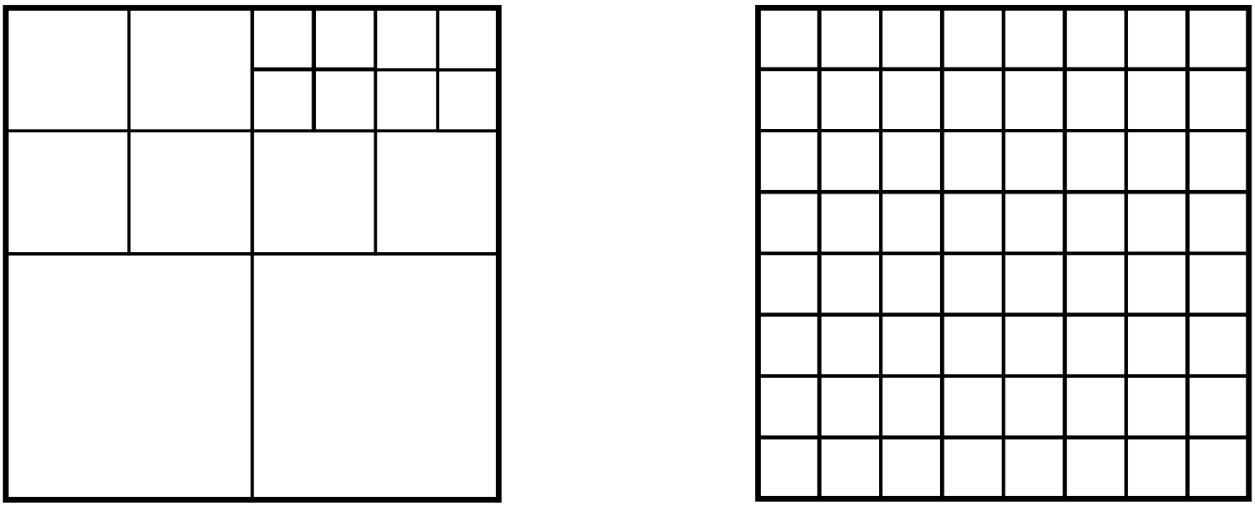

(a) Variable levels of refinement

(b) Fixed level of refinement.

Figure 13: Domain with variable levels of refinement (a) compared to the same domain with a fixed level of refinement (b).

In Figure 13a, the maximum level of refinement is set to three, and the minimum level of refinement is one. Furthermore, the mesh is refined to the maximum at the point of interest. The Basilisk solver determines the cell refinements within the given minimum and maximum levels by estimating the cell values from an up-sampling and down-sampling perspective. The error between these two approaches will determine if the cell is split into a finer refinement or merged to a coarser level [38]. If the error between the two approaches is above a given error range, the cells will split into a new refinement level, i.e. the children-cell of the parent-cell will initialise. However, if the calculated error is less than the given error range, the children-cells will deactivate, and the cells will merge into one parent cell. In other words, one refinement level down. In a case where the calculated error between the up-sampling approach and the down-sampling approach lands within the desired error range, the cell structure will remain at the same level of refinement it initially had. Following this criterion, the cells can split and merge freely as long as the process does not violate the general grid-structure requirements [38]. As mentioned, the resolution of neighbouring cells can only vary up to one level.

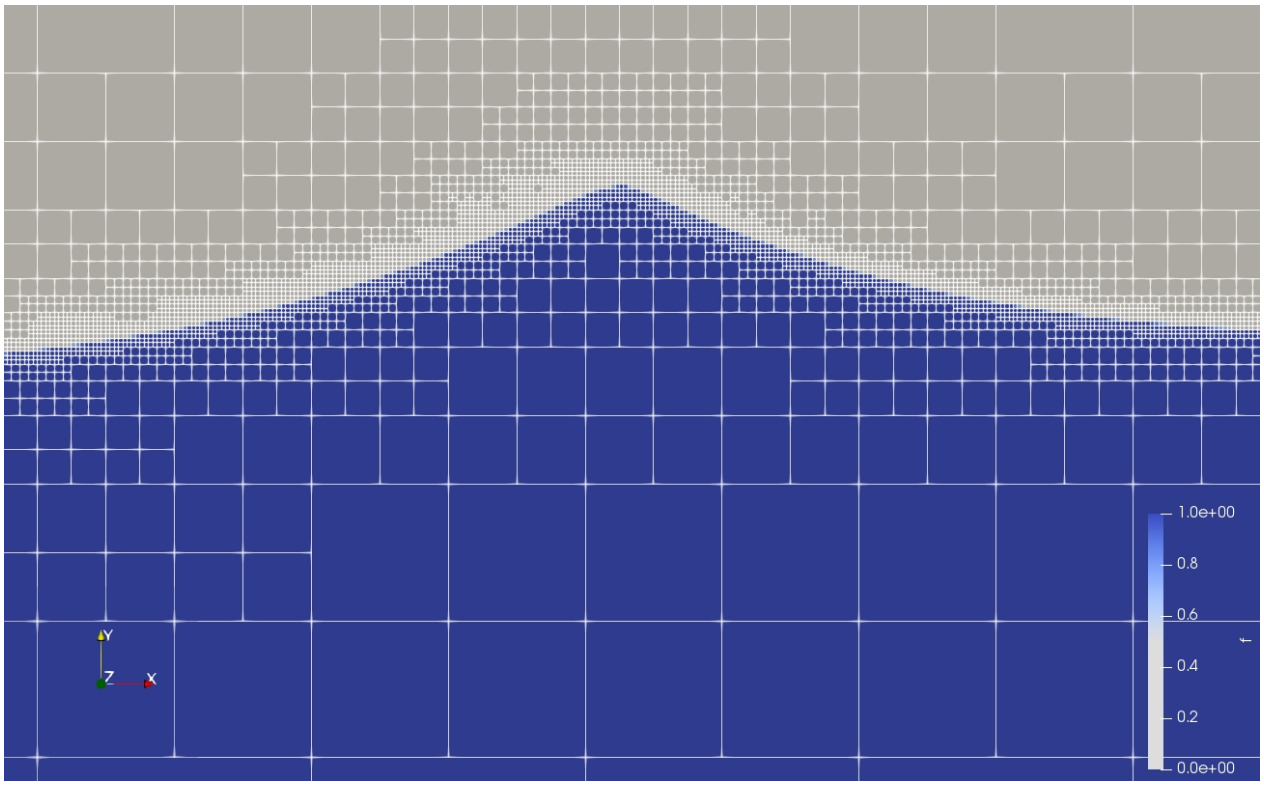

Figure 14: Mesh and grid structure at the focal peak of numerical wave event DUD112.

The mesh structure used in simulations for this project is set to be at its finest level of refinement around the free-surface. Figure 14 displays the mesh and grid-structure for the numerical wave event DUD112. The varying levels of refinement, and the hierarchy discussed, can be seen to increase from the bottom of the numerical wave tank and towards the surface.

3.3.3 Convergence testing of refinement levels

The minimum and maximum levels of refinement discussed in Section 3.3.2 is further investigated in order to determine a suitable mesh structure for the simulations of the wave events. To investigate this, the DUD112 wave event has been simulated repeatedly with varying levels of refinement from 8 to 14. The resulting measurements of the numeric time series have been analysed, and the surface elevation for the focal peak has been extracted for each run with a different level of refinement. Figure 15 illustrates how the measured peak height converges towards a height of 0.1746 metres.

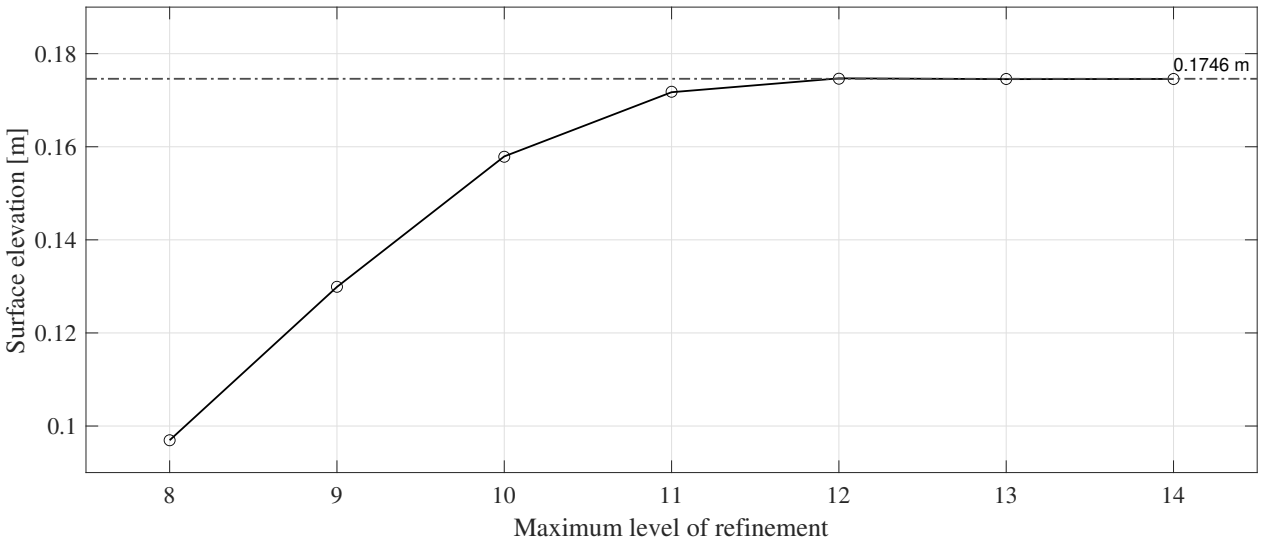

Figure 15: Measured peak height for the numerical DUD112 event with different levels of refinement.

It can be seen in Figure 15 that there is no change in the measured amplitude when changing the level of refinement from 12 to 13 and 14. This indicates that a maximum refinement level of 12 is suitable for the given wave event and that increasing the refinement level to 14

would yield no benefit and substantially longer computational time. However, as can be seen in Figure 16, where the time series of the different convergence tests are plotted, there is a minor phase shift between the two highest peaks being refinement level 13 and 12. Based on this observation and the convergence plot in Figure 15, the maximum level of refinement which was assessed to be suitable was changed from 12 to 13.

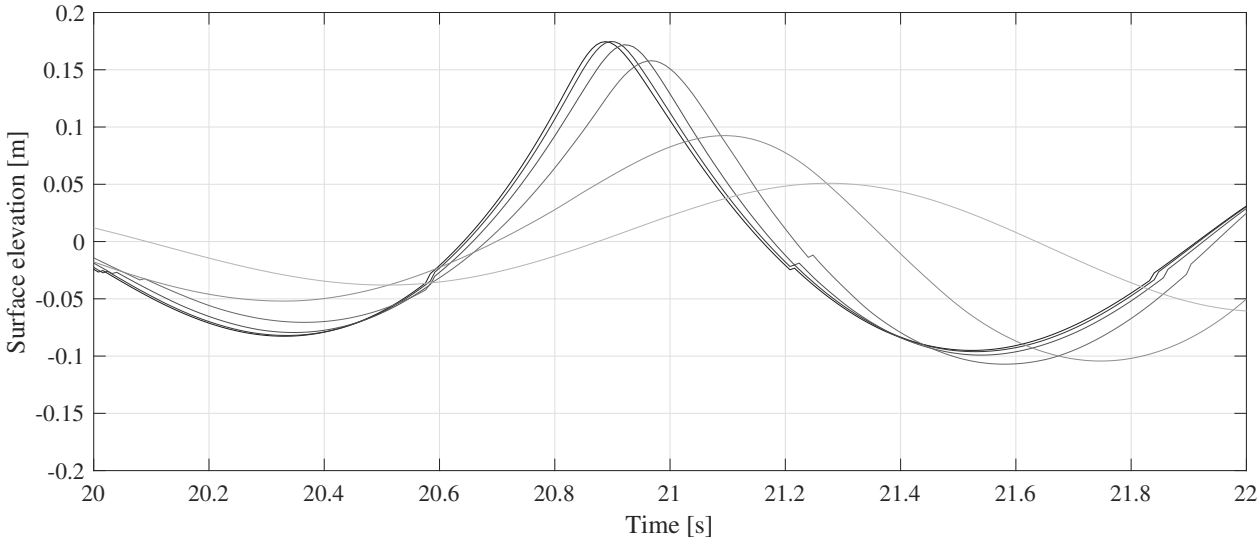

Figure 16: Numerical time series with increasing levels of refinement from 8 to 13. Refinement level 8 is coloured in the lightest colour with increasingly darker colour up to refinement level 13.

During the convergence testing, the impact of the minimum level of refinement was investigated. As the maximum peak height displayed in Figure 15 did not change when the minimum level of refinement was changed, the minimum level of refinement was determined to be at 6. The maximum level of refinement, being 13, used in the numerical simulations, with the wave tank at HVL as domain, will give a cell size of approximately 6 mm $\times$ 6 mm. The cell size corresponding to the minimum level of refinement, being 6, and therefore also the largest cells in the domain, are approximately 78 cm $\times$ 78 cm. The highest mesh resolution will correspond to approximately 433 cells per wavelength, while the lowest resolution will correspond to approximately three cells per wavelength. Here, the wavelength is defined as the mean wavelength among the input components that make up spectrum D and is calculated to be 2.6 metres.

3.3.4 Numerical wave input

The input file used to define the wave kinematics is structured according to the requirements of the Dynamic Link Library (DLL) called CFDwavemaker [37]. This wavemaker library, developed by supervisor Øystein Lande, provides several higher-order wave theories that allow for the generation of irregular waves and short crested wave fields in a numerically efficient way. In this project, the wavemaker library has been utilised to generate second-order wave kinematics at the inflow boundary in the CFD code. For a further description of what is included in the wavemaker library and how it can be used, see [37] and [18].

In the wave input file, second-order wave kinematics have been defined as described in Section 2.2. General data input such as depth and mean wave direction is defined, but in the case of a wave flume with uni-directional and long-crested waves, such as in the present experiment, the mean wave direction is zero. Furthermore, amplitudes of the different wave events can be controlled by a normalising function. This feature makes for a smoother completion of an experiment with multiple wave events with different target amplitudes within the same spectral shape, as the relationship between the different frequency components only needs to be specified ones. This is ideal for wave experiments where the spectral shape remains constant while the amplitudes are increased, such as the DUD and BUD events.

The frequency components of both spectrum B and D are defined with angular frequency, ω_n, amplitude,A_n, wavenumber, (k_n), and angular phase, φ_n. However, as the input file enables the specification of a wave reference point, in other words, a focal point in time and space, the phases for the focused wave events are set to zero. Table 9 displays the eight first frequency components, of a total of 28, used to define wave event DUD112.

Consequently, the input file used to define the kinematics at the inflow boundary of the CFD domain is now defined in the same way as the input to the wave generator used in the experimental investigation. However, the input to the numerical wave events is defined with the theoretical wave input. In contrast, the experimental cases are defined using theoretical input and the calculated transfer function. The input file used for the numerical investigation

of DUD112 can be seen in Appendix A.3.

Table 9: Eight first frequency components used to define the numerical wave event of DUD112.

$\boldsymbol{\omega}$ [rad/s]	Amplitude [m]	$\boldsymbol{k}$ [$\mathbf{m^{-1}}$]	Phase [rad]
3.8429	0.006009	1.5093	0.0
3.9154	0.005789	1.5660	0.0
3.9879	0.005580	1.6236	0.0
4.0604	0.005382	1.6827	0.0
4.1329	0.005195	1.7428	0.0
4.2054	0.005018	1.8040	0.0
4.2779	0.004849	1.8664	0.0
4.3504	0.004689	1.9300	0.0

3.3.5 Numerical output

The CFD code used in the present investigation yields two types of output. The main loop in the CFD code is programmed to save unstructured VTU-files with a given time interval. For example, in the following numerical investigation, the VTU-files are saved with a time interval of 0.1 seconds. These files can be uploaded and viewed directly in ParaView [40], where figures and animations of the wave events can be created.

Furthermore, the CFD code uses a function that can place wave gauges at given locations within the domain. This function uses the built-in height function in the Basilisk solver to calculate the surface elevation. This is defined as a vector field that gives the distance, along each coordinate axis, from the centre of the cell to the closest interface defined by a volume fraction field [41]. This function is only defined in the three to five cells closest to the surface. For further information about the built-in height function in the Basilisk solver, see [42].

Furthermore, the wave probes upper and lower height limit is defined, and the wave probe is discretized over a given number of points along the length of the probe. As the height function is only defined in the cells closest to the surface, at least one of the discretized points on the wave probe needs to be within this region to retrieve the surface elevation. Numerical wave events simulated in this thesis have been run using 450 discretized points along the length of the wave probe, which is defined between 20 cm below still water level, and 25 cm above still water level. Knowing that the smallest cells in the domain are 6 mm $\times$ 6 mm, this fine spatial resolution of the discretized points will guarantee that at least one of the points, at all times, falls within the three to five cells closest to the surface.

A fine spatial interval of wave gauges poses a challenge when conducting experimental testing in the wave tank. However, in the following numerical wave events, the wave gauge function enables the measurement area to be padded with numerical wave gauges. The numerical wave simulations performed in this thesis have the same measurement area as the experimental cases, but the distance between the wave gauges is reduced to 10 cm. Wave gauges have also been positioned at the exact location as the ones in the experimental tests, and the total number of wave gauges in the numerical wave simulations is 36. This fine spatial interval of wave gauges makes investigations into the true focal position an easier task. Figure 17 displays measurements from all the wave gauges used in the numerical simulation of the DUD112 wave event. The first wave gauge positioned at 8.8 metres is coloured black and with fading colour for each wave gauge all the way to the last wave gauge positioned at 12.28 metres.

Notably, one of the wave gauges displayed in Figure 17 has recorded the same surface elevation as the adjacent wave probe. This error has caused a gap in the surface profile, which can be seen throughout the time series. A similar type of error can be seen in other places around the crest where the elevation change is rapid and significant. The cause of this error is believed to be related to the mesh adaptation and changing refinement levels.

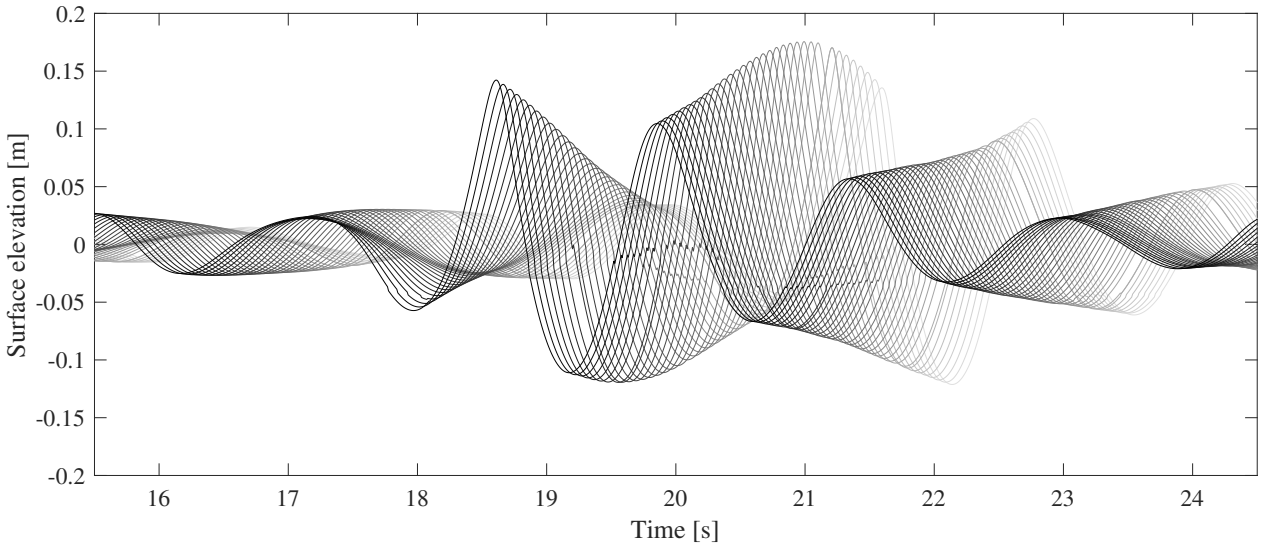

Figure 17: Numerical wave event DUD112 with all 36 wave gauges positioned between 8.8 metres and 12.28 metres.

4 Experimental Results and Discussion

Within the present section, the properties and non-linearity of the different wave groups will be analysed. This chapter aims to validate how the experimental cases resemble previous experiments by Johannessen [1] and Baldock et al. [24], as well as to assess the repeatability of the given wave groups. Properties such as spectral energy density, crest steepness, maximum height, and shift in focal location will be examined, amongst other parameters. These results may be used directly to validate numerical wave tanks and can serve as a guideline for verifying the accuracy of modelling for design waves for a given project.

One of the main objectives of this study is to examine how reproducible the focused wave groups are. By reproducing Baldock and Johannessen's experiments, it is possible to investigate how the given wave groups evolve and what effect Froude scaling has on the main experimental cases. Thomas B. Johannessen has kindly shared some of his experimental data from his PhD research [1], which is compared directly with the data from the present study. However, as Johannessen's work consists of a much more comprehensive experimental campaign, some of his results cannot be directly compared to the present study. Therefore, the validation of the model test is limited to uni-directional wave groups from spectrum D with a given set of wave gauges as presented in Section 3.2.2.

All of the BUD wave runs will be investigated in much of the same way as the DUD wave events but without the direct comparison with data from Johannessen's experiments. The spectral energy density for both the DUD and the BUD wave events will be presented together in Section 4.1. The spectral energy density for the two JONSWAP wave events will be presented together with the surface measurements in Section 4.4. Furthermore, the surface measurements from the JONSWAP-focused wave groups will be analysed in much the same way as the DUD and BUD wave groups.

Following this, the repeatability and the stability of all the focused wave groups will be presented in Section 4.5, and finally, a short explanation of the measurement database will

be given in Section 4.6.

4.1 Spectral energy density

Calculating energy in the sea state for each run will not be an accurate way of validating the model test. Since spectral energy density and irregular sea states are often associated with at least a 3-hour interval, the model test time series, each lasting about one minute, will be too short to determine the given sea state's energy accurately. However, comparing the present study and Johannessen's experimental data using the same calculations and parameters, it is possible to see how the present scaled-up study resembles the 1997 experiment.

All spectral energy calculations in this thesis were performed using a fast Fourier transform and a MATLAB script generated by external supervisor Øystein Lande. See attachment A.1 for more details.

4.1.1 DUD wave cases

As discussed in Section 3.2.5, DUD37 acts approximately linearly compared to the higher DUD and BUD waves. Because of this property, DUD37 was the wave case used to calibrate and generate the transfer function for all the DUD wave runs. Being the reference wave when calibrating in regards to spectral energy density, it is expected that this case will be the case that closest resembles the theoretical energy density. From Figure 18a it is clear that the measured spectral energy takes almost the same form as the theoretical. However, the energy level is slightly lower than the theoretical over the entire frequency range. Amplitude correction during the calibration process, where the spectral energy was lowered to give the linear amplitude, is the reason for this. The measured spectral energy in Figure 18a ensured a stable amplitude for DUD37 close to the target amplitude of 36.667 mm.

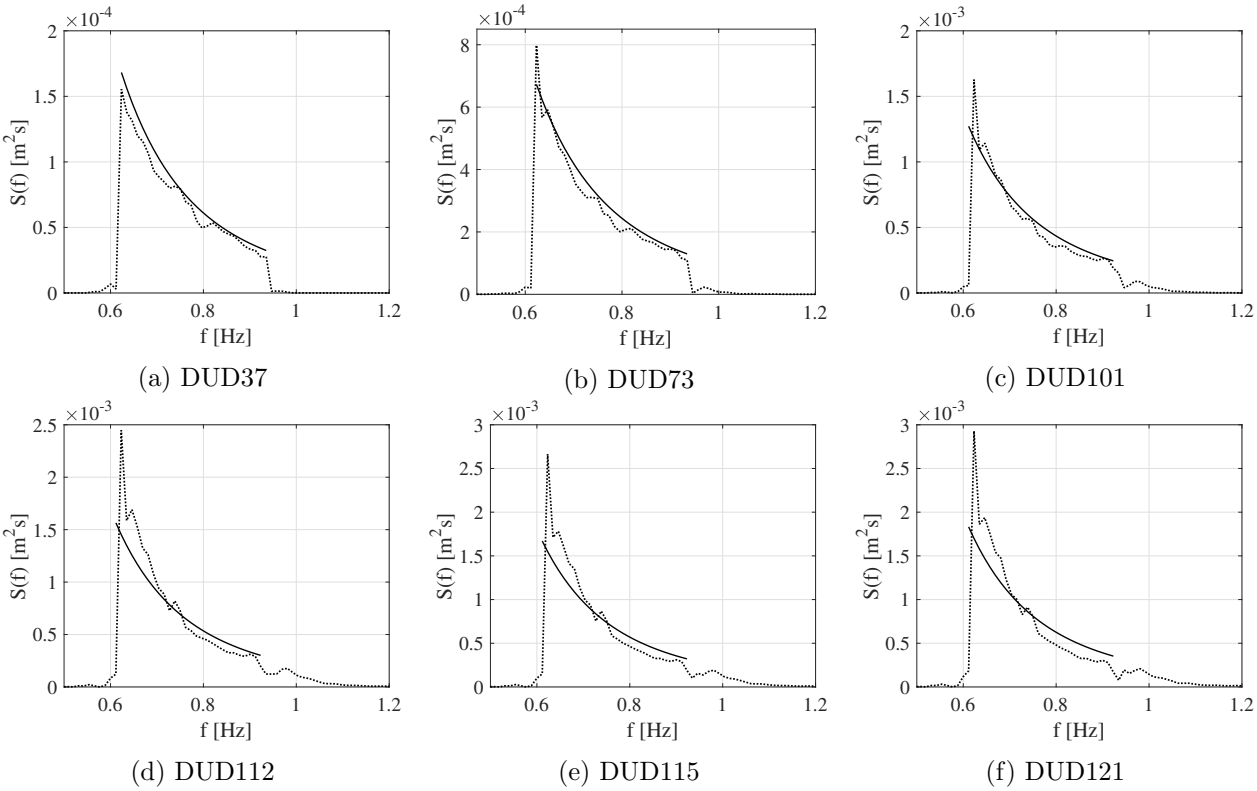

(a) DUD37 (b) DUD73 (c) DUD101

(d) DUD112 (e) DUD115 (f) DUD121

Figure 18: Spectral energy density calculations for all DUD wave events. Dotted line indicates the calculated spectral energy density from the measured time series, while solid line represents the theoretical spectrum.

With DUD37 being the reference wave for calibration and generation of the transfer function, it is expected that the differences and errors in measured and theoretical spectral energy density only will increase with increasing amplitude. This can be observed when examining Figure 18 and the higher wave events such as Figure 18d, which displays the measured spectral energy density for wave gauge 1 in the DUD112 case. A linear gain correction has been applied to the DUD112 case visualised in Figure 18d in addition to the original transfer function. All frequency components have been multiplied by 1.09 to increase the overall energy so that the measured maximum amplitude corresponds to Johannessen's results. This linear gain correction might explain why the measured spectral energy density experiences a relatively large overshoot at its maximum, around 0.61 Hz.

Even though the transfer function satisfies the case of DUD37, it was expected to generate more significant deviations with increasing amplitude. That is why the additional linear gain

correction was applied for the three largest events being DUD112, DUD115 and DUD121. Therefore, measurements from the DUD112 wave run are captured with both the original input and the transfer function with the additional gain correction of 1.09. This applies to DUD121, DUD115, and DUD121, as mentioned.

Some similarities between Figure 18a and 18d can be observed, but the distinct difference between them is the prominent peak visible in the DUD112 case. For all wave groups, a small peak in energy at approximately 0.75 Hz was observed. This corresponds to the tank width's transverse standing wave frequency, so despite extensive calibration and fine-tuning of the DUD37 case, the peak appeared. This region in the frequency range proved to be hard to calibrate for the DUD37 run, and the transfer function for the DUD waves might not be a good fit for the higher amplitude wave runs. The transverse standing wave frequency can go a long way in explaining why this region in the frequency range proved hard to calibrate. It is also believed that with increasing amplitude, the cross-tank reflections will also increase and thereby affect the measurements and energy calculations in a greater manner than what the transfer function can correct.

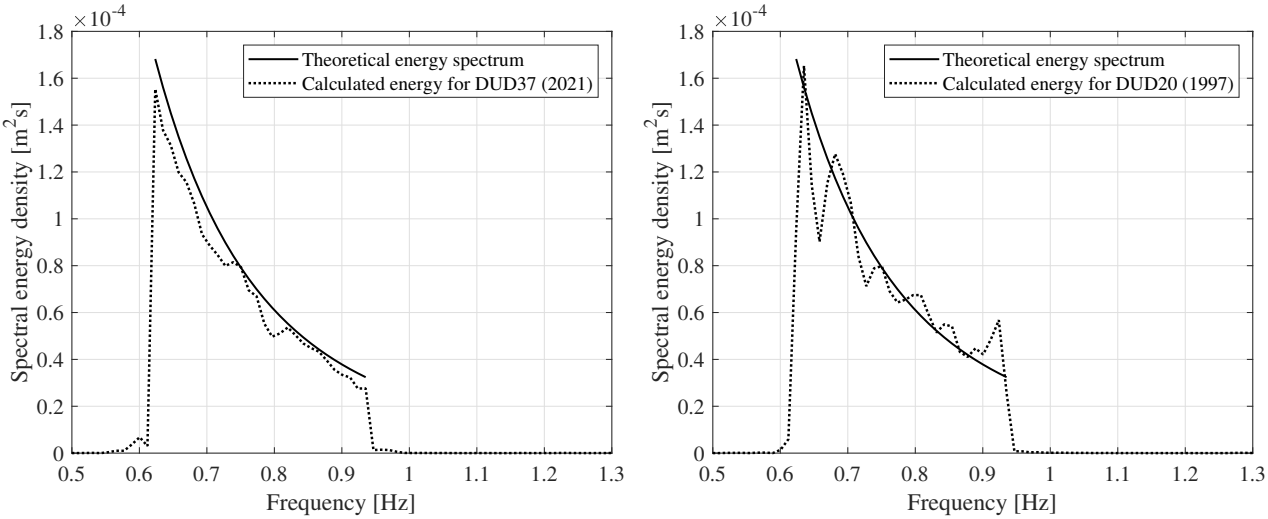

(a) DUD37 wave event in 2021

(b) DUD20 wave event in 1997 [1]

Figure 19: Energy calculations for previous experiment and present experiment, with the DUD20 wave run from 1997 scaled up in advance of the energy calculations.

As Johannessen conducted his experiments in a wide wave basin, the cross-tank effects will

not be present in his measurements or energy calculations. This can be observed in Figure 19 where the energy from the DUD37 wave run and Johannessen's original DUD20 wave run from 1997, scaled to match DUD37, is displayed side by side in Figure 19a and 19b respectively. The energy content for both wave runs is calculated using the same routine as mentioned previously.

Some of the same effects observed in Figure 19 can be seen in the higher amplitude wave runs such as DUD61 and the corresponding DUD112. In DUD20 and DUD37, there is little to no contribution from higher frequencies than the cut-off frequency of 0.923 Hz. This is not the case for the higher amplitude events such as the DUD61 and DUD112. In Figure 20, the two higher amplitude events are displayed in the same way as DUD20 and DUD37, with DUD112 and DUD61 corresponding to Figure 20a and 20b, respectively.

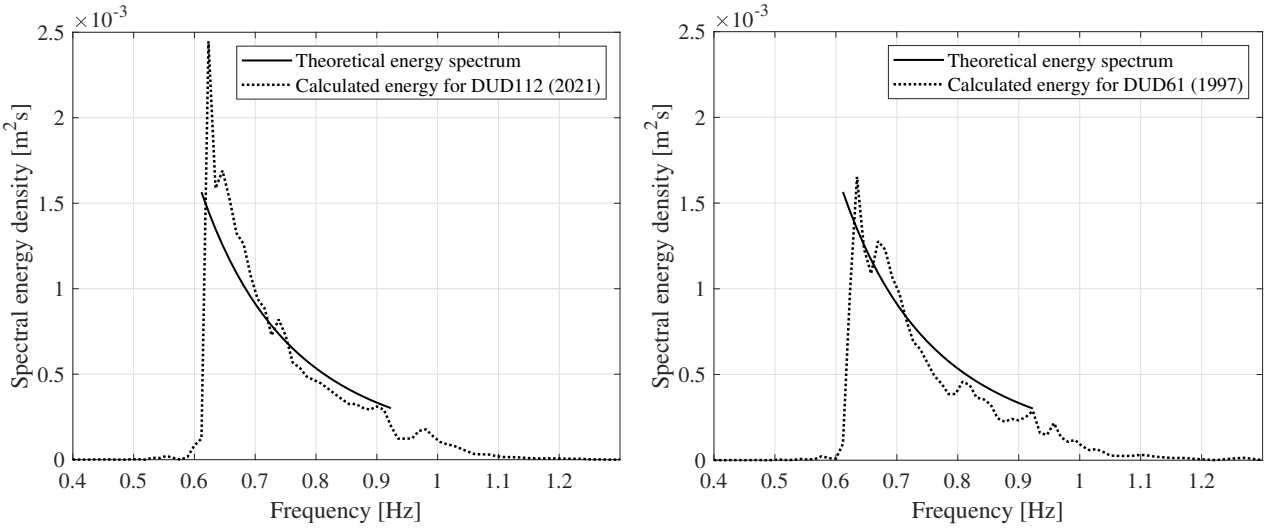

(a) DUD112 wave event in 2021

(b) DUD61 wave event in 1997 [1]

Figure 20: Energy calculations for previous experiment and present experiment, with the DUD61 wave run from 1997 scaled up in advance of the energy calculations.

In Figure 20 it is visible that there is a significant contribution from frequencies above the cut-off frequency compared to the lower amplitude cases. Energy calculations for the present experiments demonstrate that the transfer function for spectrum D works well for the lower amplitude cases but struggles more with the higher amplitudes like DUD112, DUD115, and DUD121. This is similar to what is observed in Johannessen's data, where energy calculations

for DUD20 fit well with the desired spectrum while the higher amplitude cases like DUD61 experience more deviation compared to the theoretical and desired spectrum.

All the results from the energy calculations are summarised in Table 10. Table 10 contains parameters such as Root Mean Square Error values (RMSE), deviation in the zeroth-order moments, and maximum crest elevation measured in the time series as a percentage of the linear target amplitude of the given wave event.

Table 10: Comparison of energy calculations with present study and Johannessen's experiment. RMSE-value is calculated with respect to the theoretical spectrum for the given wave event. Maximum crest is given as a percentage deviation of the linear prediction and m_0 deviation is given as a percentage deviation between theoretical zeroth-order moment and the measured one.

	Present Study			**Johannessen 1997**		
Wave case	**RMSE** [$\mathrm{m}^2\mathbf{s}$]	**m_0 deviation** [%]	**Max crest** [%]	**RMSE** [$\mathrm{m}^2 s$]	**m_0 deviation** [%]	**Max crest** [%]
DUD37/20*	$3.15 \cdot 10^{-5}$	- 11.2	+ 0.0	$3.51 \cdot 10^{-5}$	- 7.1	+ 0.8
DUD112/61*	$3.62 \cdot 10^{-4}$	+ 0.7	+ 45.3	$3.18 \cdot 10^{-4}$	- 16.0	+ 47.3

*All of Johannessen's time series [1] were scaled up prior to the energy calculation.

The RMSE-values and the maximum crest deviation percentage given in Table 10 indicates that the present investigation is well in line with the 1997 experiment. A lower RMSE-value for the DUD37 event than the DUD20 event shows that the energy content in the present wave run is closer to the theoretical target than what Johannessen achieved in his investigation. However, the RMSE-value of the higher amplitude cases, DUD112/61, is lower for Johannessen's DUD61 than the present case DUD112. This indicates that Johannessen's experiment is closer to the theoretical energy spectrum for the DUD112/61 case. The calculation of the RMSE-values is only done for energy content within the frequency range of spectrum D, in other words, between 0.6116 Hz and 0.9232 Hz. For the DUD37/20 case, this will be a good approximation as there is little to no energy contribution by frequencies above or below the desired frequency range, as shown in Figure 19. However, for the DUD112/61 event, the given way of calculating the RMSE-value will not give an equally accurate ap-

proximation. This is mainly due to energy contribution from frequencies above the cut-off frequency of 0.9232 Hz, which can be seen in Figure 20.

By looking at the zeroth-order moment of the theoretical spectrum and comparing it to the zeroth-order moment for the measured and calculated energy spectrum, it is possible to quantify how well the measurements compare to the theoretical spectrum. The spectral moments in a Gaussian wave field are defined by Equation (2.16).

When examining the zeroth-order moment, the expression reduces to the integral of $S(\omega)$ due to n equal zero, which equates to the area under the curve of the theoretical spectrum. Thus, if the energy content in the measured time series exactly matched the theoretical spectrum, the difference in the two zeroth-order moments would equal zero. In other words, zero percent deviation. Hence, this parameter serves as an indication of how well the measurements resemble the desired theoretical spectrum. However, the calculations do not explain where in the frequency range the deviations are present.

From Table 10 both DUD37 and DUD20 have somewhat similar deviation between the two zeroth-order moments, with DUD20 being the most accurate. However, the values and the difference between the present study and Johannessen's data increase in the case of DUD112 and DUD61. This is expected due to more significant energy content in these wave runs and well in line with observations from Figure 19 and 20. Here, fluctuations in the energy content are observed as well as energy contribution from outside the desired frequency range, and as a result, the overall error in regards to the theoretical spectrum increases. Nonetheless, the deviation in zeroth-order moments for DUD112 is reduced to less than 1 %. The implementation of the additional gain correction of 1.09 for the largest wave events explains this reduction.

Based solely on the zeroth-order moment parameter, it is fair to say that the present study is equally accurate as Johannessen's experiments. However, a wide wave basin, such as the one used in Johannessen's experiments, will feature stronger three-dimensional effects which are not present in the wave tank at HVL.

4.1.2 BUD wave cases

With no available experimental data from T. Johannessen's investigation, the spectral energy density for the BUD wave events cannot be compared to previous experiments. Therefore, the spectral calculations from the BUD events are only compared against the theoretical energy spectrum. Figure 21 displays the three different BUD wave events and their calculated spectral energy density.

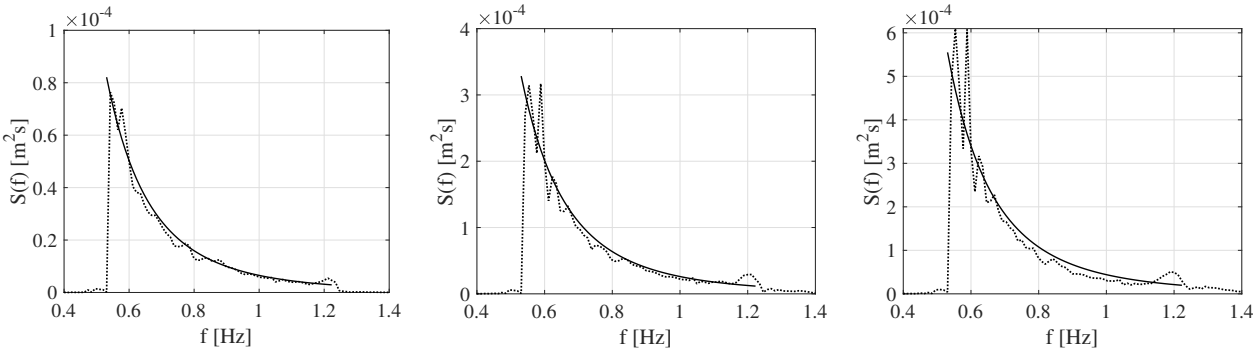

(a) BUD37 (b) BUD73 (c) BUD95

Figure 21: Spectral energy density calculations for all BUD wave events. Dotted line indicates the calculated spectral energy density from the measured time series, while solid line represents the theoretical spectrum.

Spectrum B is defined with the same spectral shape as spectrum D, but the difference between the two can clearly be identified when comparing Figure 18 and 21. Introducing a wider frequency range, with 61 frequency components compared to 28 for spectrum D, the energy density for the individual frequency components of the BUD events will be lower than the comparable event for the DUD cases. For instance, the peak value observed in Figure 21a is approximately half of what is observed in Figure 18a for the DUD37 event.

Some of the same effects seen for the DUD events, when the amplitudes and energy content is increased, can be seen in BUD73 and BUD95. An overshoot around the peak frequency increases with increasing amplitude, indicating that the transfer function for the BUD event struggles with the higher amplitude cases, just as the DUD transfer function. Furthermore, the energy contribution from frequencies outside of the defined frequency range is significantly

less than for the DUD cases. Based solely on visual inspection, it seems that the BUD events are more in line with the theoretical energy target than the DUD cases.

The deviations observed in Figure 21 are further quantified and listed in Table 11. Notably, the RMSE-values for the BUD events are lower than for the DUD events, which are listed in Table 10. However, the individual frequency components are also lower, meaning that the BUD and the DUD events cannot be compared directly using this parameter.

Table 11: Spectral energy density parameters for BUD wave events. RMSE-value is calculated with respect to the theoretical spectrum for the given wave event. Maximum crest is given as a percentage of the linear prediction and m_0 deviation is given as a percentage deviation between theoretical zeroth-order moment and measured.

Wave event	**RMSE** $[m^2 s]$	m_0 **deviation** [%]	**Max Crest** [%]
BUD37	$1.08 \cdot 10^{-5}$	− 9.4	+ 0.6
BUD73	$4.55 \cdot 10^{-5}$	− 9.1	+ 17.1
BUD95	$8.21 \cdot 10^{-5}$	− 9.5	+ 41.0

Examining the zeroth-order spectral moment will indicate how much energy is present in the wave event. For the BUD events, the deviation between the theoretical and measured spectral moment is surprisingly stable. All of the wave events in Table 11 display a measured energy content approximately 9 % less than the theoretical energy content. This is partly because the overall energy content in the wave event BUD37 was lowered such that the measured amplitude would equal the desired target amplitude. The same deviation can be seen for the DUD37 event in Table 10, with the measured energy content being 11.2 % lower than the theoretical target.

Nonetheless, all of the wave events, both DUD and BUD, demonstrate good agreement with the theoretical target spectrum. Observations indicate that energy contribution from outside the frequency range can be expected for the most narrow banded wave events. With increasing bandwidth, these contributions are, to some extent, negligible. Investigations into the zeroth-order spectral moment reveal that the target frequency range's energy content is

lower than the theoretical one for almost all the wave events. However, for the largest DUD wave events, the additional gain correction of 1.09 gives a measured energy content closer to the theoretical target.

4.2 DUD - Surface measurements

Within the present section, the time series of the different wave events are analysed. Amplitudes for the DUD events range in size from the almost linear DUD37 to the highly nonlinear DUD121. All the wave events will be compared against linear theory and Johannessen's experimental data. Focal quality for the different wave groups, as well as nonlinear behaviour, is also examined.

4.2.1 Surface elevation at the focal location

As mentioned previously, the focus location for all the wave events within the D-spectrum is set to wave gauge 1, located 8.8 metres from the wavemaker, and the time of focus is set to 20 seconds. Therefore, all the figures and data in the present subsection are extracted from the wave gauge positioned at the focal location.

DUD37

Being the event with the smallest amplitude, the surface elevation of DUD37 can, to some extent, be accurately predicted by linear wave theory. This can be observed in Figure 22 where the surface measurements of DUD37 is compared with linear theory.

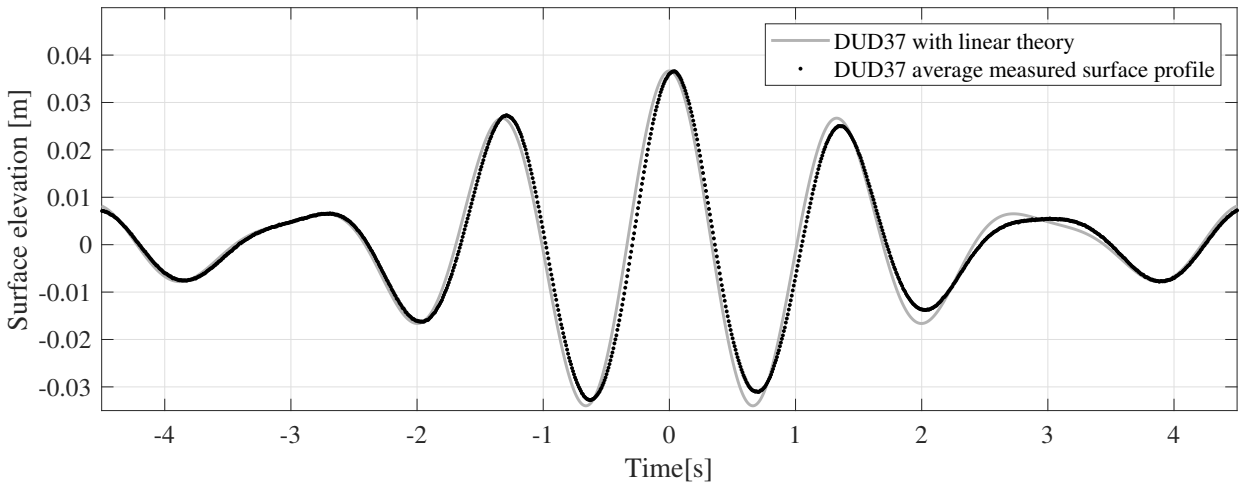

Figure 22: Measured time series of DUD37 at focal location plotted against the linear time series of DUD37. Time is centered around the desired focus time of 20 seconds.

As the transfer function was generated using the DUD37 wave run, the maximum peak in the measured time series achieves almost precisely the same height as the linear prediction. The average maximum wave height in the measured time series is 36.6058 mm, which results in a difference of 0.06084 mm compared to the linear time series. This difference is smaller than the given measurement uncertainty of the wave gauges, which is $\pm$ 0.1% of the measurement area. As the wave gauges were calibrated using a measurement range of 0.55 metres, this results in a measurement uncertainty of $\pm$ 0.55 mm, as mentioned in Section 3.2.2.

The transfer function for the wave tank was developed, assuming that DUD37 was a linear wave event. However, as shown in Figure 22, the troughs on both sides of the maximum crest do not reach as low as predicted by linear theory. This proves that the assumption of DUD37 being entirely linear is not correct. Measurements can be seen to match the linear prediction well before the time of focus but deviate more the seconds after the focus time, as can be seen in Figure 22. The time of focus is also slightly shifted compared to linear prediction and given focal time. These observations result from minor non-linear effects present in the DUD37 wave case. However, the slight phase shift compared to linear theory can also be caused by hardware error, in other words, the wavemaker, or inaccuracies in the placement of wave gauges. The wave gauges are conditioned to start recording simultaneously as the wavemaker starts. However, minor deviations between the start of data recording and the start of the wavemaker can be expected. Distances between the wave gauges were also measured by hand, and a slight deviation in actual position compared to target position can be expected. In DUD37, the measured crest reaches its maximum approximately 0.04 seconds after the given time of focus, thus making hardware error a probable cause of the slight phase shift.

Many of the mentioned effects observed in the DUD37 time series are also present in Johannessen's DUD20 wave case from 1997. Both DUD37 and DUD20 are compared in Figure 23. DUD20 is scaled up to match the present experiment and the linear prediction.

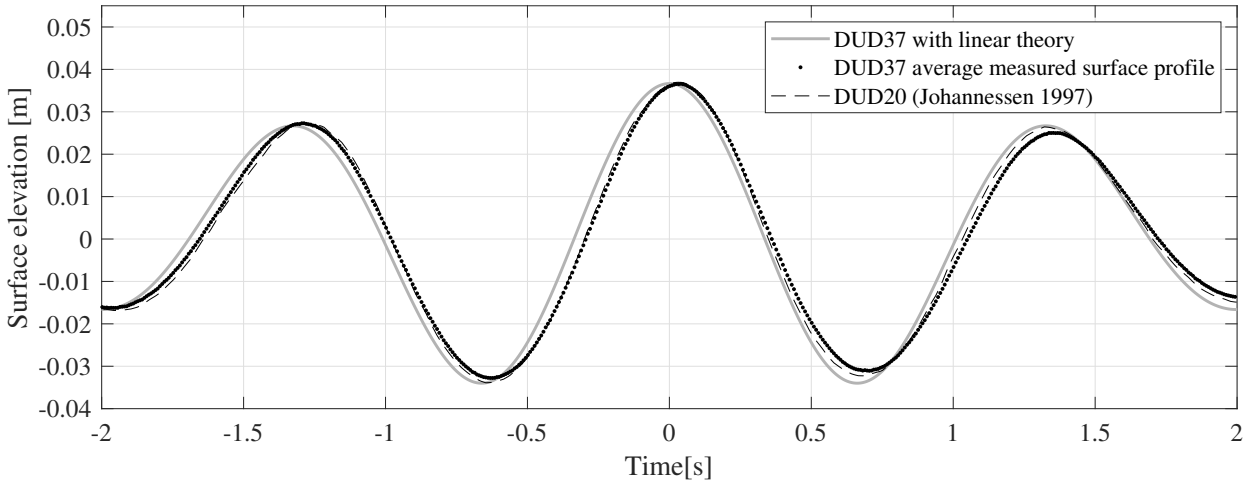

Figure 23: DUD37 and DUD20 (1997) plotted against linear theory. DUD20 is align with the peak of DUD37 to make differences more identifiable.

Figure 23 shows that the same asymmetric behaviour on each side of the maximum crest identified in the current experiment is also present in Johannessen's data. Thus, even though Johannessen's data might align better with the linear prediction, the same nonlinear behaviour, namely minor wave amplification and shallower troughs, is observed in his data.

DUD73

The wave case of DUD73 is effectively a doubling of the DUD37 case in respect to amplitude. While DUD37 acts as a close to linear event, the same can not be said for the DUD73 case. Figure 24 shows the measured surface elevation of DUD73 in the focal location of 8.8 metres from the wavemaker.

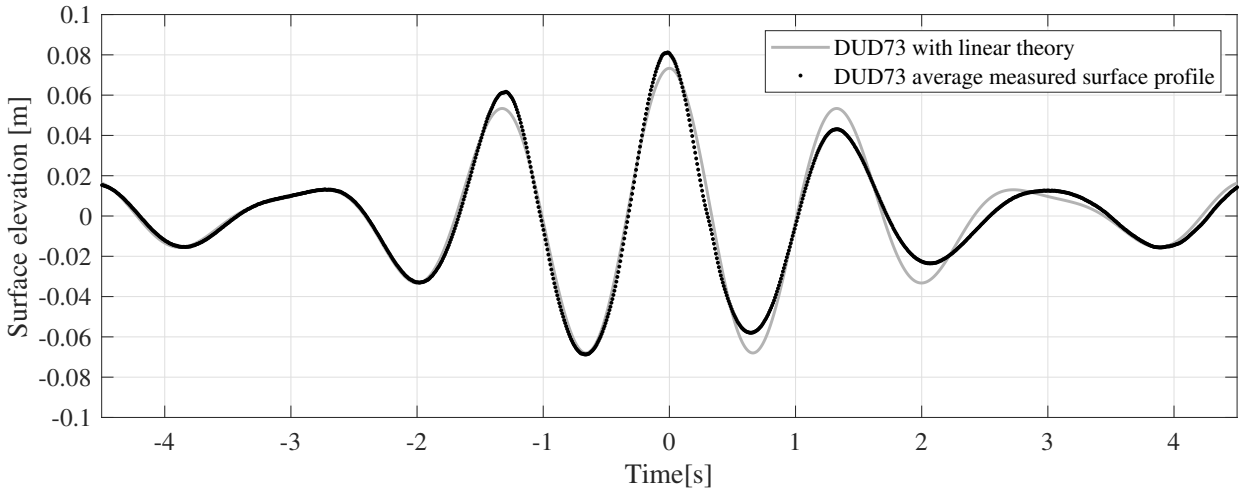

Figure 24: Measured time series of DUD73 at focal location plotted against the linear time series of DUD73. Time is centred around the desired focus time of 20 seconds.

The wave event DUD73 deviates more from the linear prediction compared to DUD37. Most notably is the overshoot at its peak around the time of focus. Compared to DUD37, it seems that the given wave event reaches its maximum before the desired time of focus. However, this is not the case. The increasing nonlinear wave-wave interactions will shift the focus location in both time and space. As a result, the location of focus and the position of the maximum crest are shifted just beyond the wave gauge positioned at 8.8 metres, which makes it undetectable for the wave gauges. Hence, the maximum wave height in the time series displayed in Figure 24 will not be the overall maximum in the wave tank for the given wave case. In other words, if the number of wave gauges was increased and the distance between them reduced, the overall maximum wave crest would be identifiable.

Johannessen's experimental campaign was conducted with a far more extensive setup of wave gauges [1]. This enabled him to measure the actual overall maximum to a more accu-

rate extent than the present study. By comparing the measurements from this study with Johannessen's data for the same corresponding wave gauges, it can be observed that the same effects of shifting focus location and a maximum crest prior to the focal time are present. This can be seen in Figure 25 where Johannessen's DUD40 is scaled up and plotted against the present DUD73 and a linear prediction of DUD73.

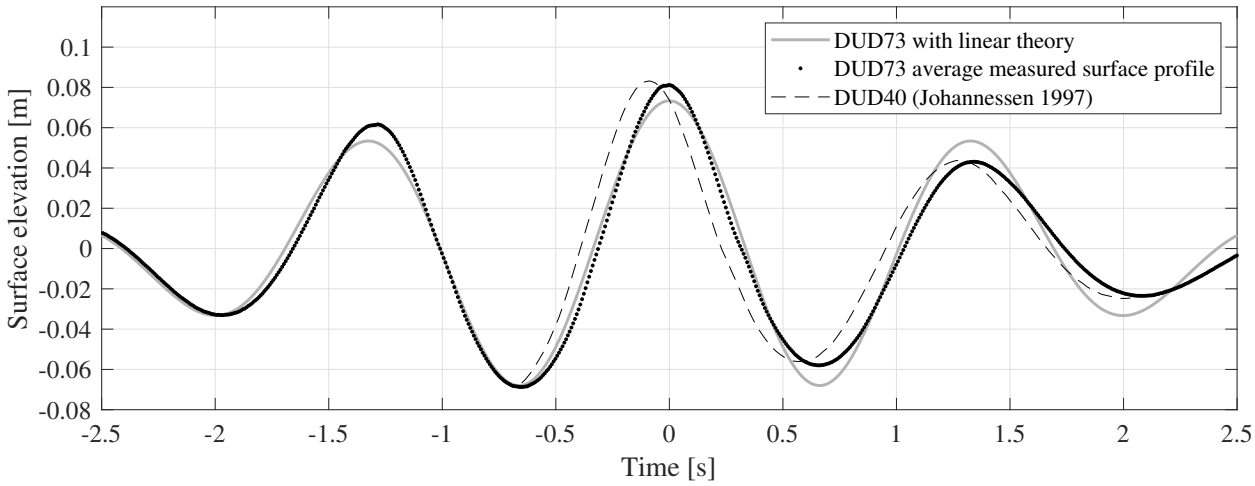

Figure 25: DUD73 and DUD40 (1997) plotted against linear theory. The provided data from Johannessen's experiments does not contain a full time series of DUD40, thus limiting the comparison of data to just around the time of focus.

Data from DUD40 in 1997 is limited to measurements just around the time of focus and is the reason why DUD40 is only plotted between approximately 0.5 seconds prior to time of focus and 2 seconds after the time of focus is Figure 25. In Figure 23, the measurements from 1997 are aligned with the results from the present study in order to compare the two cases in closer detail. This is not the case for Figure 25 where none of the time series is shifted, and there is a distinct phase difference between the DUD40 case and the DUD73 case. As mentioned previously, this is believed to be mainly due to hardware error such as misalignment of the wave gauge. However, if the measurements from DUD40 is shifted and aligned with DUD73, little to no deviations between the time series is observed, although the maximum wave height of DUD40 is measured to be marginally higher than for the DUD73 case.

DUD101

In the wave event of DUD101, the presence of nonlinear effects becomes clear. In this wave run, the target amplitude is almost triple that of the close to linear event of DUD37. In Figure 26, the measurements of the time series taken from the wave gauge in the focal location clearly deviate from the linear prediction. Most notably is the increase in the neighbouring peak to the left of the focal location. Compared to the previous wave cases of DUD37 and DUD73, this peak increases while the peak at the time of focus remains relatively stable. The trough in between these two peaks is also increasing.

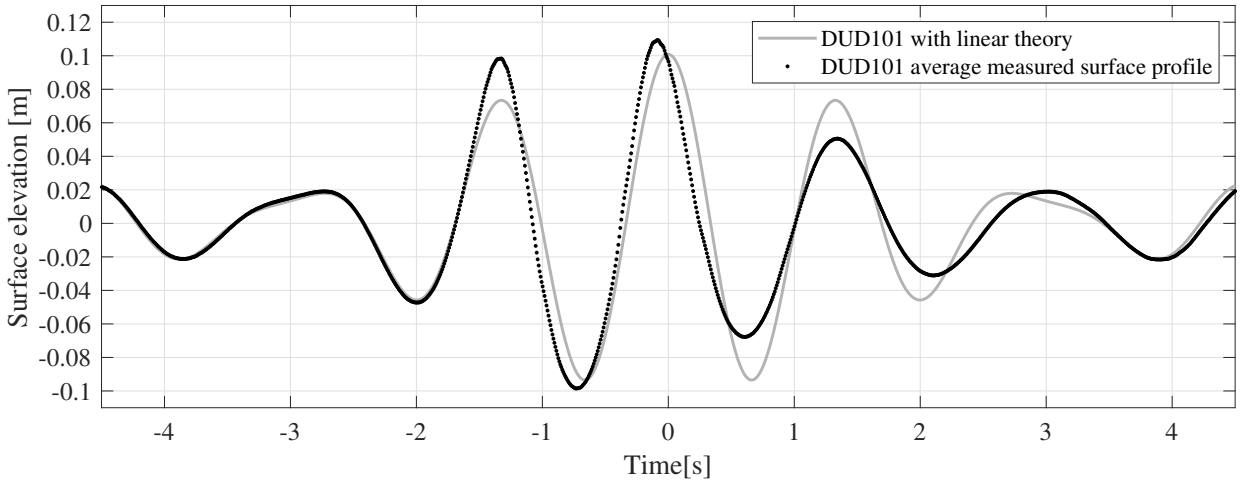

Figure 26: Measured time series of DUD101 at focal location plotted against the linear time series of DUD101. Time is centered around the desired focus time of 20 seconds.

The focus location of the DUD101 event is moved even further down the wave tank compared to DUD73, thus making the peak around the time of focus appear smaller than expected and in advance of the focal time. It becomes clear that linear wave theory is unsuitable for modelling this wave event with its given amplitude and steepness.

Same as for the previous event, the DUD101 case is plotted against DUD55 from 1997. In Figure 27 the DUD55 event is seen to match DUD101 and no distinct phase-shift is observed. As all the wave gauges are mounted to the towing carriage, and this carriage has been observed to slightly shift its position, even when turned off, this could be an explanation as to why DUD101 and DUD55 are now aligned contrary to the time series in Figure 25.

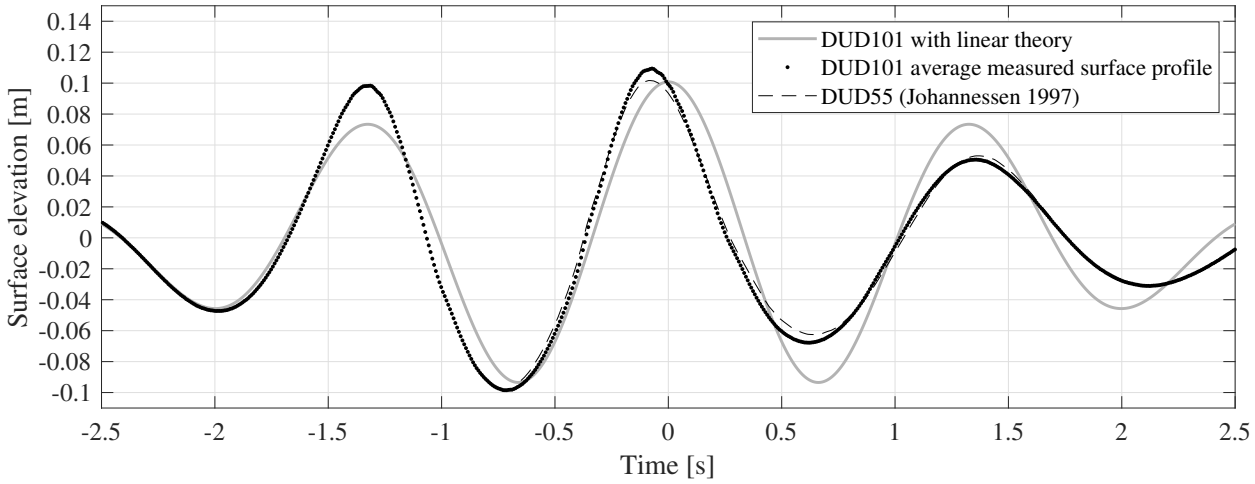

Figure 27: DUD101 and DUD55 (1997) plotted against linear theory. The provided data from Johannessen's experiments does not contain a full time series of DUD55, thus limiting the comparison of data to just around the time of focus.

The scaled-up DUD55 experiences a lower peak compared to DUD101 around the focal time. It is expected that the measurements from the present study and Johannessen's experimental data will deviate more as the amplitude for each wave event is increased.

DUD112

DUD112 is the wave case that corresponds to Johannessen's DUD61. With a 61 mm amplitude, this wave event was the highest wave Johannessen managed for a uni-directional wave in spectrum D without experiencing wave breaking. In this wave event, the nonlinear wave-wave interactions generate extensive deviations in terms of wave amplification and phase modulation from the linear prediction, as can be seen in Figure 28. The peak in the focal position stays relatively constant compared to previous wave runs. However, the neighbouring peak prior to the time of focus is increasing drastically compared to previous cases.

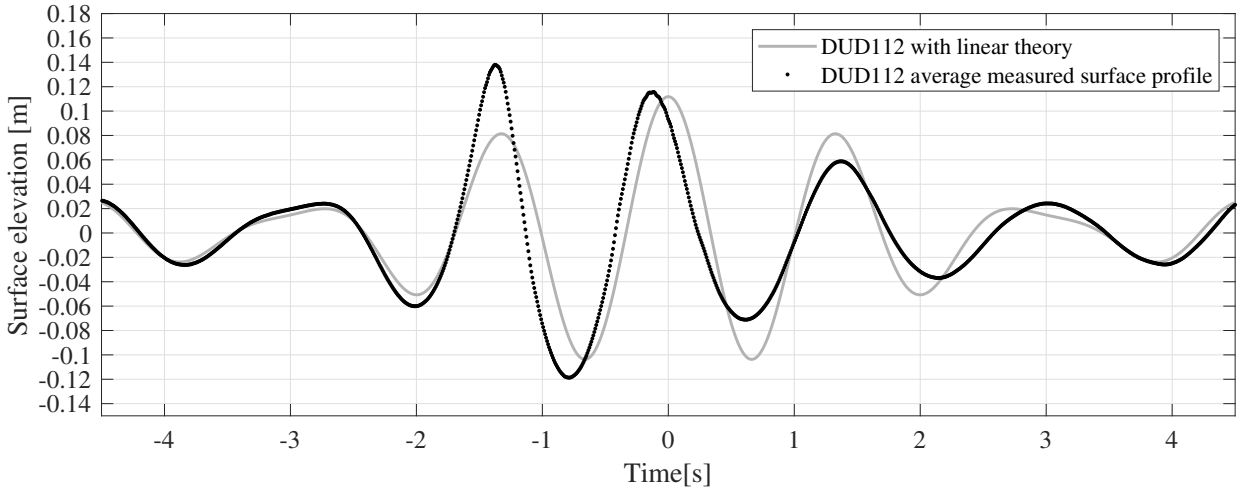

Figure 28: Measured time series of DUD112 at focal location plotted against the linear time series of DUD112. Time is centered around the desired focus time of 20 seconds.

In the event of DUD112, no wave breaking or spilling of the wave crest is observed. This is well in line with Johannessen's observations with the DUD61 event. The present study and data from the 1997 experimental campaign are compared in Figure 29. For the DUD61 wave case, the provided data from Johannessen covers the whole time series of the given event, thus giving a more comprehensive comparison compared to the two previous events.

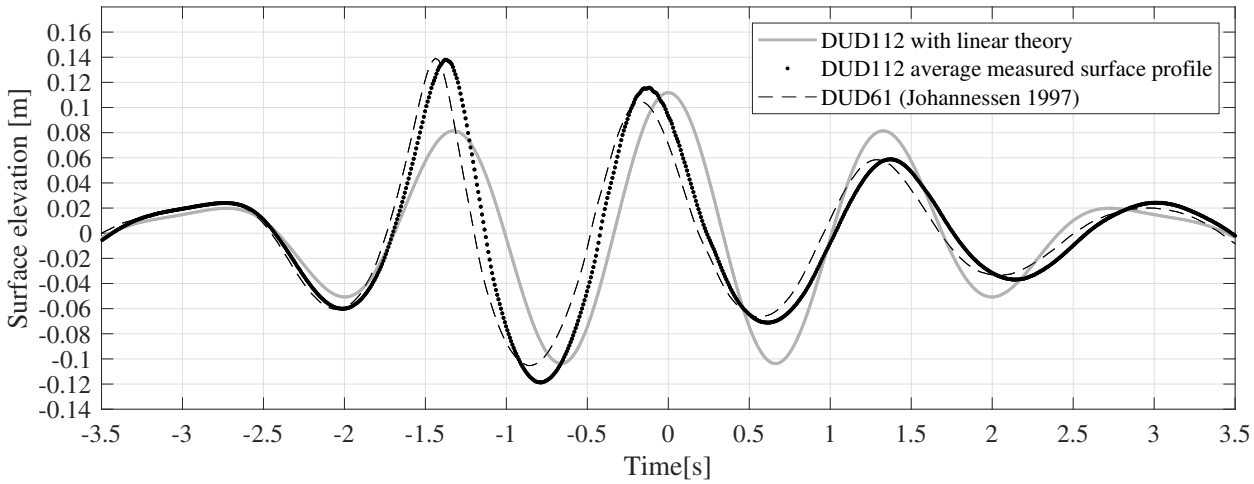

Figure 29: DUD112 and DUD61 (1997) measured at the focal location plotted against linear theory.

Once again, hardware errors such as the placement of wave gauges in the present study seem to generate a phase shift in the measurements compared to Johannessen's experimental data.

This is probably most notable in the third peak around 1.5 seconds after the time of focusing. If this peak in the present data were aligned, the rest of the measurements would more or less align perfectly with Johannessen's previous experiment. Apart from the small phase-shift, the peaks measured in the present experiment match the scaled up peaks in the 1997 data quite well. The most prominent peak in the time series, around 1.5 seconds prior to the time of focus, is measured to 0.1379 metres in the present experiment. Johannessen's scaled-up data reaches a maximum of 0.1391 metres in the same location, resulting in a difference of 0.0012 metres, or about 1.2 mm. With the wave event not being entirely focused, and the maximum measured wave crest still extends beyond the input amplitude of 112 mm, it is assumed that when the wave case actually focuses, the peak will reach even higher due to the presence of strong nonlinear wave-wave amplification.

DUD115 and DUD121

The DUD115 and DUD121 events are new experiments conducted only in this study. Johannessen stopped increasing the amplitude when he reached DUD61 and concluded that the steepness of the focused wave was just at the point before it experienced spilling or breaking. In this study, the amplitude was increased beyond this critical point to observe how the waves acted. Thus, DUD115 and DUD121 would, in Johannessen's experiments, correspond to a wave event with 63 and 66 mm amplitude, respectively. Figure 30 displays both of these wave events with DUD115 on top and DUD121 at the bottom.

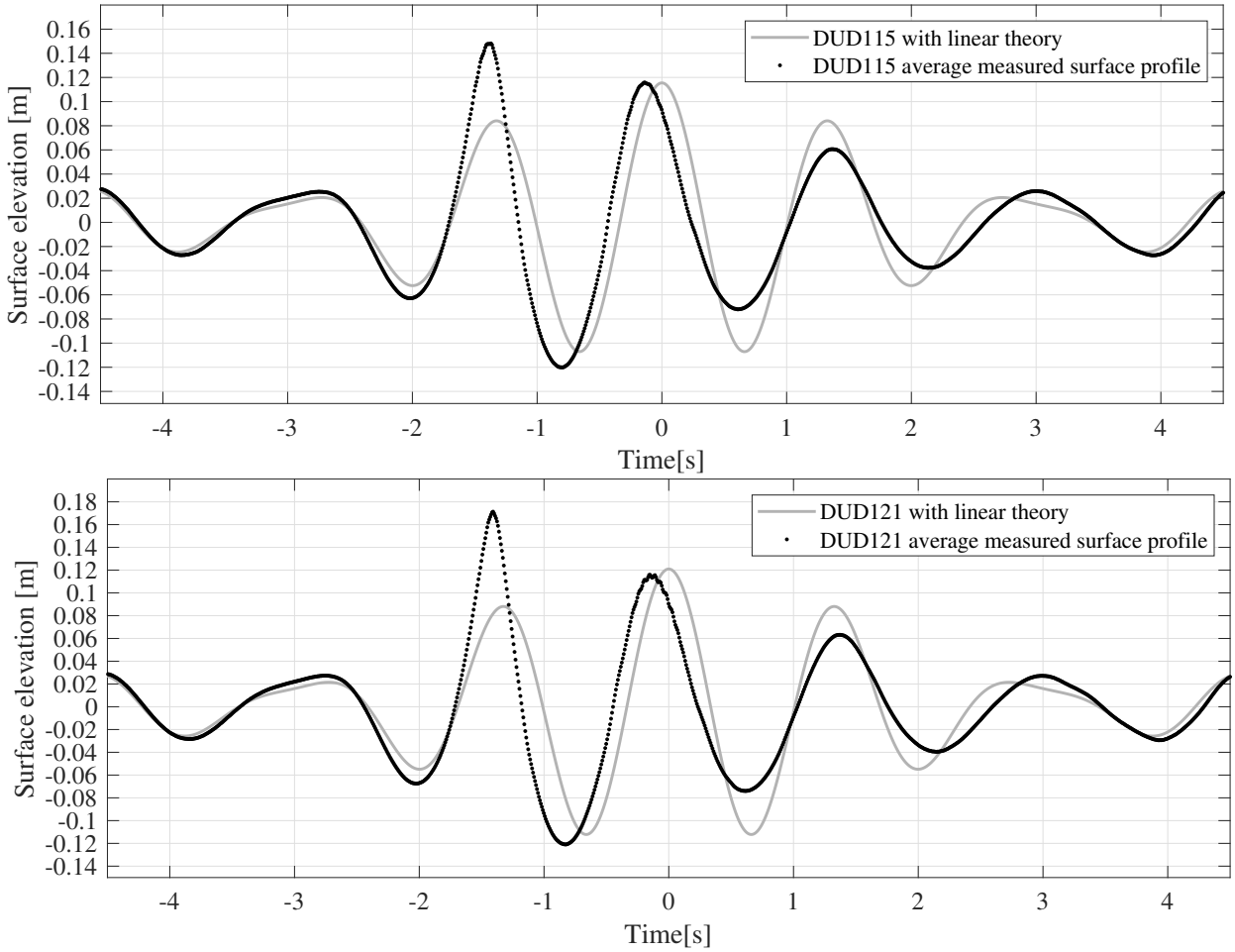

Figure 30: Measured surface elevation for both DUD115 (top) and DUD121 (bottom) compared against its respective linear prediction.

The peak around 1.5 seconds in advance of the focal time is again seen to increase in line with the increasing input amplitude. Regarding time, neither of the two troughs on each

side of this peak is seen to shift with increasing input amplitude. The trough locations in time, negative 2 seconds and close to negative 1 second, is relatively constant throughout the DUD wave events. The stable time difference between the two troughs and the increasing maximum of the peak in between results in a steeper and steeper wave for each wave case as the amplitude is increased. However, the steepness for this particular peak did not reach a critical level, and no observations of wave breaking or spilling around the focal location were made.

As discussed previously in this section, the maximum wave height measured at the focal location is not necessarily the maximum in the wave tank. This is especially true for DUD115 and DUD121 as they are the most nonlinear wave events in this study, and their respected focus location in the tank is shifted downwave the most. Further investigation of the other wave gauges is necessary to determine the overall maximum wave amplitude for the different wave events, and this will be analysed in the next section.

Summary of all DUD measurements from the focal location

All the different wave events have been normalised to compare them in regards to the desired input amplitude. Figure 31 shows all the wave runs with their measured surface profile normalised. This figure does not contain any legend, but the measurements are organised so that DUD37 is displayed in the lightest tone of grey and DUD121 is displayed in the darkest colour.

Being normalised with respect to the linear target amplitude, Figure 31 visualises the nonlinear wave amplification experienced in the focal location. This is most obvious for the first peak, which clearly increases for each run and slightly shifts its time of maximum. The centre peak at the desired focal time does, however, not change drastically with respect to wave height. This observation may seem counterintuitive but is merely a result of the degrading focal quality, i.e. shifting focal location.

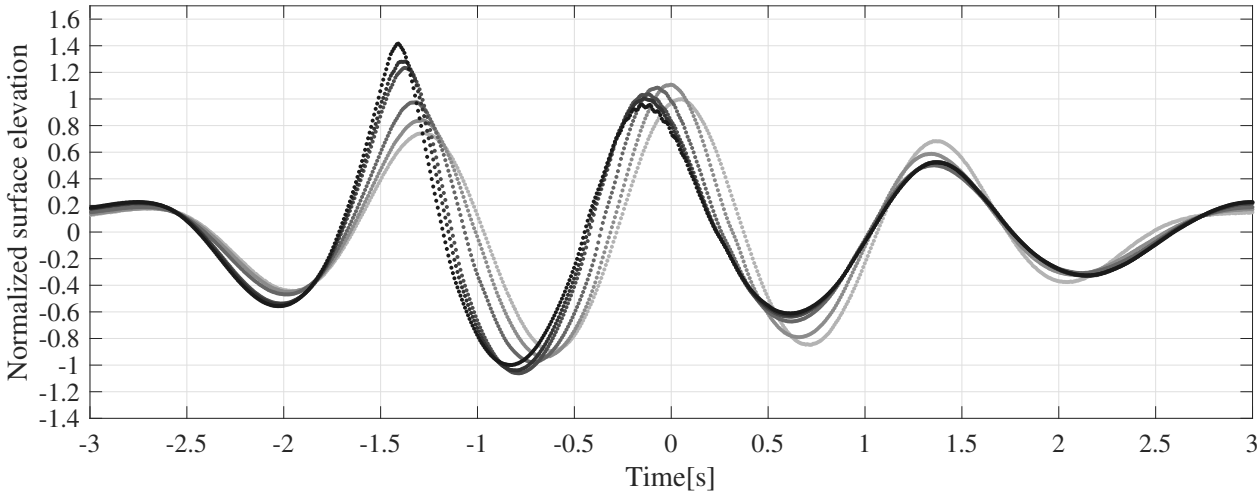

Figure 31: All the different wave events normalised with respect to their different linear target amplitude. The data is coloured with the lowest amplitude case of DUD37 being light grey and with increasing level of darkness as amplitudes increase all the way to DUD121 being coloured the darkest.

Table 12 summarises all the wave cases with different parameters. The measurements so far are only collected for the first wave gauge placed at the focal location of 8.8 metres and 20 second and is the basis for all the calculations in Table 12. From Figure 31 three distinct peaks can be observed and in Table 12 they are named Peak I, Peak II and Peak III.

Table 12: Analysis of the three most prominent peaks in all wave runs seen in the data for the focal location.

	Peak I ($t \approx$ -1.3 s)			**Peak II ($t \approx 0$ s)**			**Peak III ($t \approx$ 1.3 s)**		
Wave Case	**Amplitude** [m]	**Linear deviation** [%]	**ϵ (ka)**	**Amplitude** [m]	**Linear deviation** [%]	**ϵ (ka)**	**Amplitude** [m]	**Linear deviation** [%]	**ϵ (ka)**
DUD37	0.0273	+ 2.29	0.062	0.0366	0	0.083	0.0250	- 6.33	0.057
DUD73	0.0617	+ 15.59	0.142	0.0812	+ 10.75	0.193	0.0431	- 19.26	0.086
DUD101	0.0983	+ 33.92	0.241	0.1094	+ 8.53	0.249	0.0506	- 31.06	0.090
DUD112	0.1379	+ 69.39	0.367	0.1157	+ 3.49	0.234	0.0588	- 27.77	0.102
DUD115	0.1481	+ 76.14	0.407	0.1158	+ 0.26	0.234	0.0606	- 27.93	0.106
DUD121	0.1713	+ 94.48	0.471	0.1159	- 4.21	0.225	0.0632	- 28.25	0.109

The theoretical limit as to how steep an ocean gravity wave can be was first proposed by

Stokes [5]. The Stokes' limit is regarded as the relation between wave height and wavelength and is set to be approximately one over seven respectively, or more precisely, 0.1412. Defining Stokes' limit in the form of wavenumber and amplitude gives a limit of approximately $ka = 0.44$. However, studies done more recently propose a different limit to how steep an ocean gravity wave can become. Toffoli et al. argue that the ultimate threshold for the wavenumber and amplitude parameter is 0.55, which is notably higher than the Stokes' limit [2]. However, this is given as the threshold for the front-face steepness, and the rear-end steepness is still considered equivalent to Stokes' limit of approximately 0.44. In this study, the maximum limit of the steepness parameter is therefore considered to be $ka = 0.55$.

The steepness for the individual peaks in the DUD wave events is calculated using the time difference between the troughs. Linear theory and the relation between wavelength, λ and wave period for finite water depth, given by Equation (2.6), is used further to determine the wavelength of the different peaks. Finally, k is determined using the relation $k = 2\pi/\lambda$, and the steepness, ka, can be determined by multiplying k with the measured amplitude.

From Table 12 it is clear that none of the peaks in the data exceeds the threshold for steepness. However, the first peak in the DUD121 wave run, with a calculated steepness of $ka = 0.4708$, is the closest to the threshold but still within the limit. Notably, this is above the maximum threshold proposed by Stokes [5], which indicates that the threshold proposed by Toffoli et al. [2] might be more accurate. As mention, the measurements from the focal location do not indicate the overall maximum for any of the wave events, except for the fairly linear DUD37 case. Furthermore, higher wave amplitudes and steeper waves are expected to be observed for the other wave gauges downwave of the focal position, especially for the most nonlinear cases like DUD112 and upwards. The following section analyses the overall maximum measured in the wave tank.

4.2.2 Surface elevation at point of maximum crest

The previous section covered all the measurements at the focal location for the DUD cases. Due to increasing nonlinear behaviour and degrading focal quality, the focus location is shifted downwave for the highest amplitude cases. This means that the highest measured surface elevation could be at wave gauge 1, 2, 3 or 5. Therefore, this section will look at the highest measured surface elevation, regardless of the position of the wave gauges. This will give a good indication as to how far downwave, in both time and space, the focal position has shifted.

Figure 32 displays measurements from all the wave gauges used in the DUD37 wave event. In this fairly linear wave event, the highest measured crest height is in the focal location and the first wave gauge, as can be seen. The crest from the first peak at approximately 1.3 seconds before the time of focus can be traced as it passes the other gauges downwave in the tank, and by doing so, it can be observed that it decreases as it moves away from the focus location.

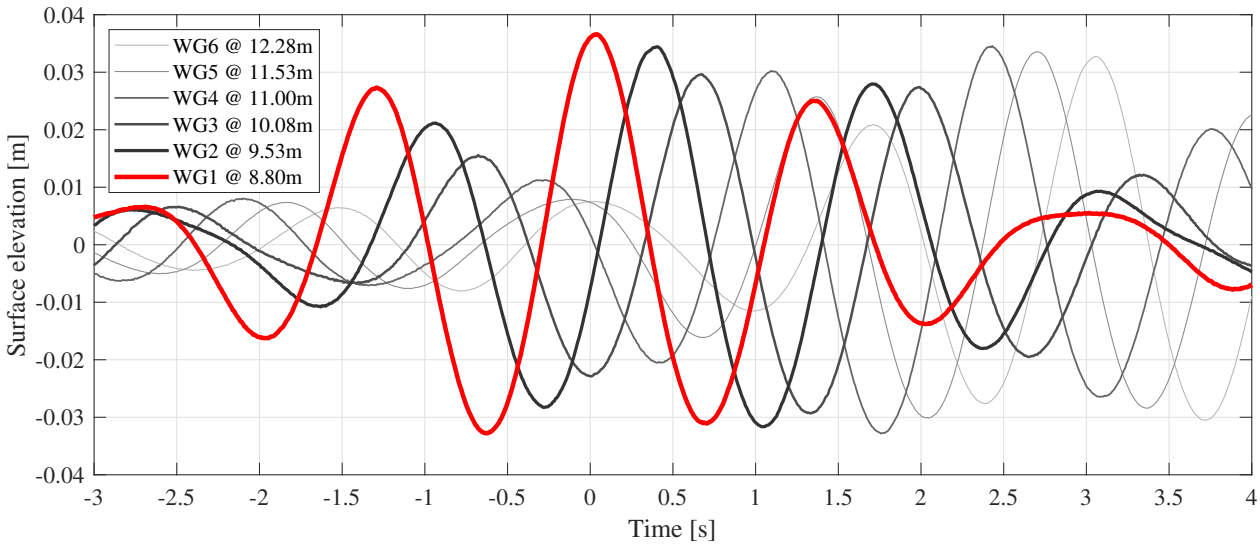

Figure 32: Surface profile measurements for all six wavegauges used in he DUD37 wave event.

The next peak, and the highest, at around 0 seconds, can similarly to the first peak be seen to decrease as it is traced down the wave tank. Contrary to the two first peaks, the third

peak is increasing as it is traced down the tank. This is explained by frequency components travelling with different speeds. Frequency components present in the focus location catch up with the frequency components in the third peak and add up to a higher and higher measured crest. The same can be observed at the first peak, where the frequency components with the greatest velocity travel away from the peak and make the measured crest lower as it passes down the wave tank with more and more frequency components leaving the location of this peak.

The same visualisation is done for the other wave cases and displayed in Figure 33, 34, 35, 36, and 37, being DUD73, DUD101, DUD112, DUD115 and DUD121, respectively. The time series with the highest measured peak is indicated with the colour red.

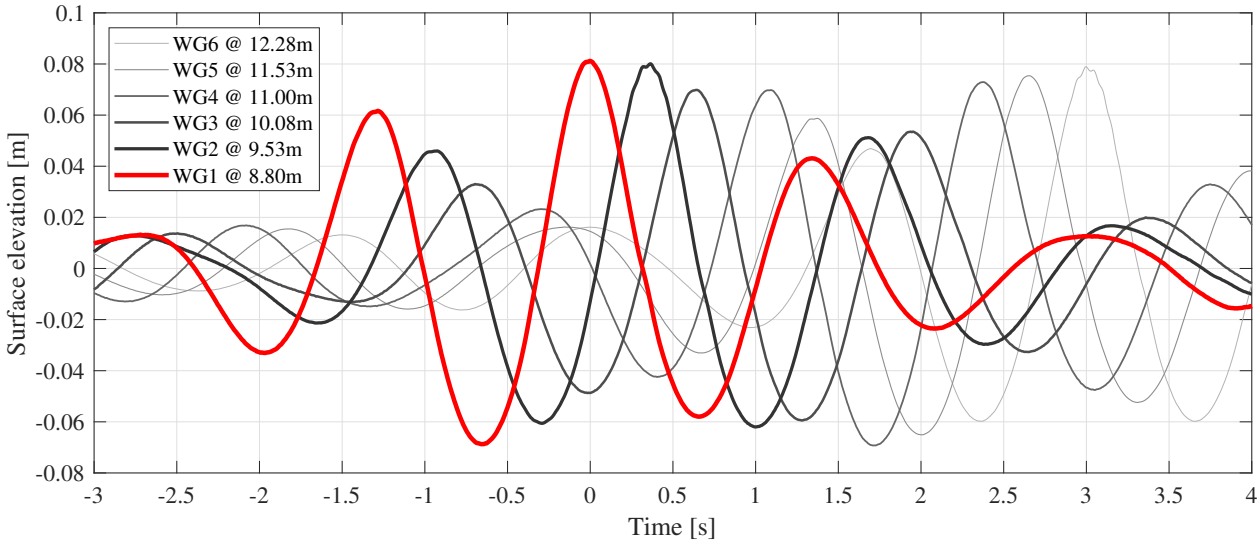

Figure 33: DUD73 wave event with all six wave gauges.

As mentioned, the close to linear DUD37 case focuses as intended at the focal position. The DUD73 event, however, also registers its maximum at the focal position, but as can be seen in Figure 33, the second wave gauge measures almost the same height. This indicates that the focal position has shifted downwave and is now somewhere between the first and second wave gauge.

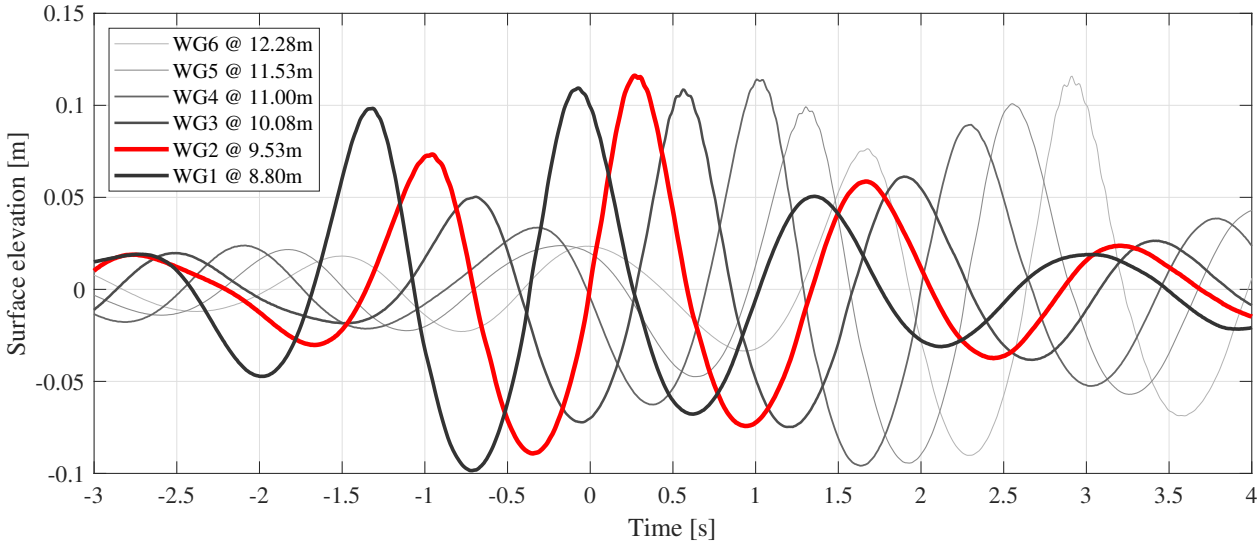

Figure 34: DUD101 wave event with all six wave gauges.

Looking at Figure 34, the highest measured peak is now located at the second wave gauge positioned at 9.53 metres. However, this does not mean that the focal location for DUD101 has shifted to exactly 9.53 metres but indicates that the focal location is somewhere in the close vicinity of this wave gauge. The symmetry between the troughs can indicate how good the focal quality is for the different wave gauges. In the case of DUD101, the first trough is lower than the one at the opposite side of the focal peak, thus indicating that DUD101 is not entirely in focus.

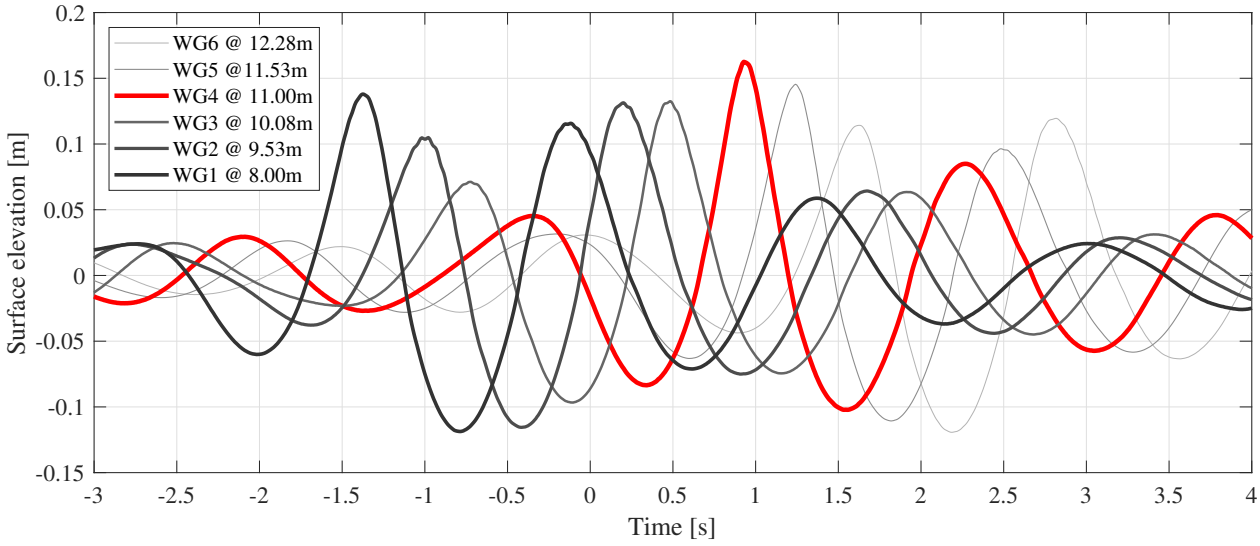

Figure 35: DUD112 wave event with all six wave gauges

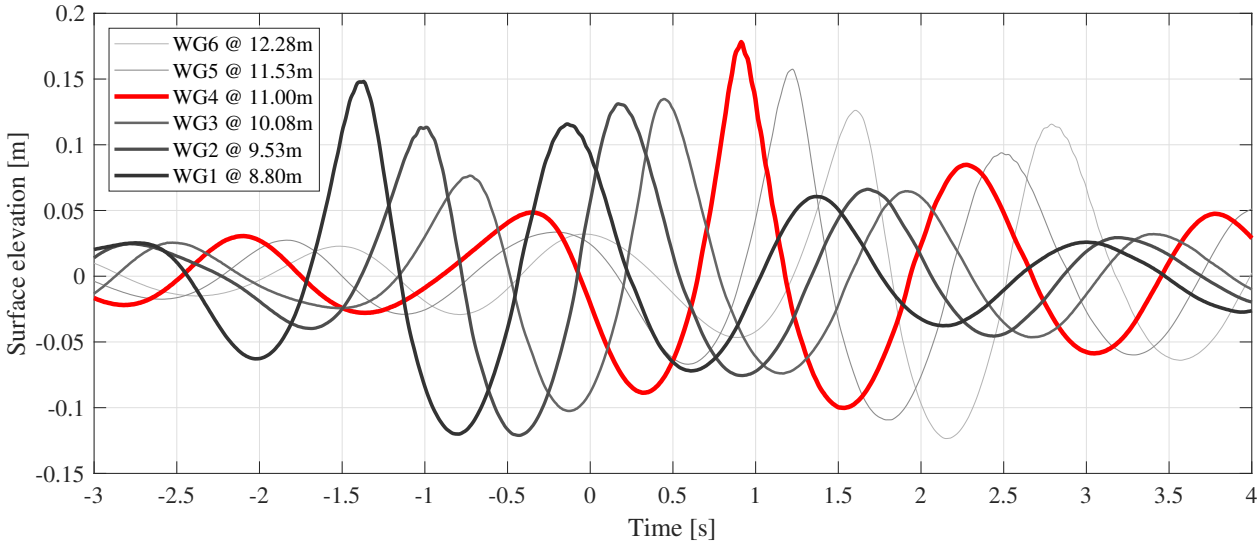

Figure 36: DUD115 wave event with all six wave gauges.

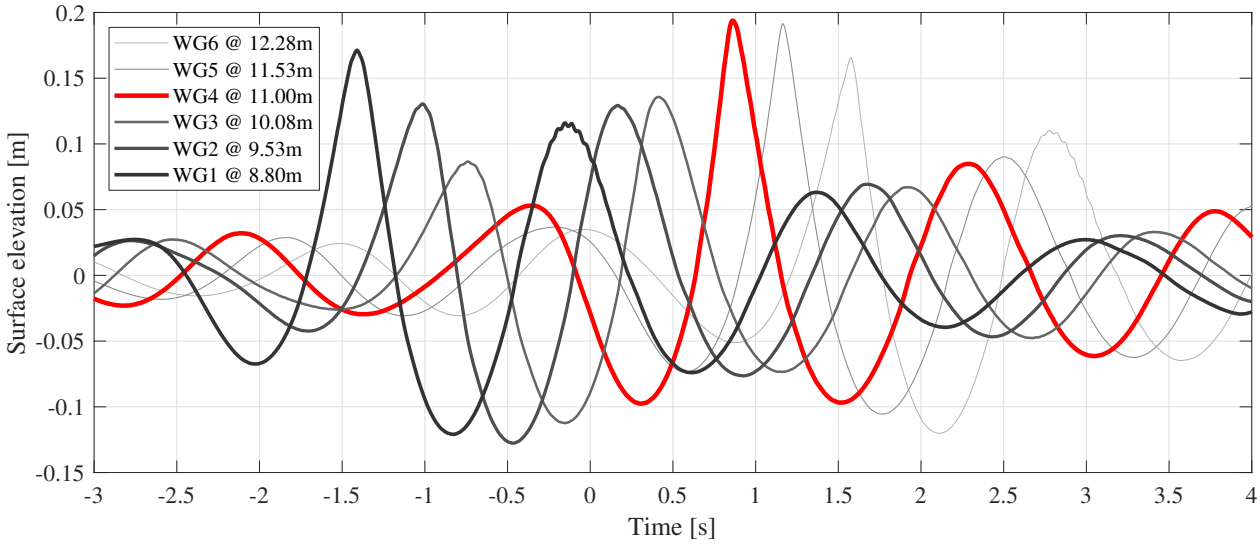

Figure 37: DUD121 wave event with all six wave gauges.

In the DUD112, DUD115 and DUD121 events, the highest measured crest is registered at wave gauge number four, located at 11.00 metres. By comparing Figure 35, 36 and 37, it can be observed that the symmetry between the troughs increases as the amplitude is increased. The troughs on each side of the prominent peak in the DUD121 event are close to symmetrical regarding surface elevation. This might indicate that the focal position for this given event is shifted to more or less precisely 11.00 metres, 2.20 metres downwave from the target location.

Table 13 contains different parameters for the different wave runs. Contrary to Table 12, which analysed the three most prominent peaks in the vicinity of the focal area, Table 13 only considers the maximum peak for each wave case regardless of its position in the wave tank.

Table 13: Different parameters for the maximum wave crest measured in all wave cases.

Wave Case	**Maximum amplitude** [m]	**Linear deviation** [%]	**Calculated steepness** (ka)	**Wavegauge number**	**Time since focal time** [s]
DUD37	0.0366	0	0.083	1	+ 0.04
DUD73	0.0812	+ 10.73	0.193	1	+ 0.00
DUD101	0.1161	+ 15.14	0.281	2	+ 0.27
DUD112	0.1625	+ 45.30	0.447	4	+ 0.93
DUD115	0.1781	+ 54.20	0.481	4	+ 0.91
DUD121	0.1938	+ 60.17	0.533	4	+ 0.86

Both DUD37 and DUD73 experience their maximum crest at the focal location and the first wave gauge. However, the higher amplitude cases experience a shift in the focal location due to nonlinear wave-wave interactions, and this causes the maximum crest to appear further down the wave tank. The case of DUD101 only shifts its maximum to the second wave gauge, while the three higher wave runs reach their maximum at the fourth wave gauge positioned at 11.00 metres. These higher amplitude wave events experience higher and steeper waves compared to the measurements from the focal location. The maximum crest measured for the DUD121 case is over 60 % larger than its linear input amplitude, and its steepness parameter, calculated to be approximately 0.53, approaches the ultimate threshold of $ka = 0.55$.

None of the wave events experienced any form of wave breaking within the measurement area. However, for the two largest events, DUD115 and DUD121, some minor spilling of the wave crest was observed at approximately 18 to 19 metres from the wavemaker, well beyond

the last wave gauge positioned at 12.28 metres. Visual observations of the wave height in this position indicate that it was well below the maximum height measured at the fourth wave gauge, making wave height an improbable cause for wave spilling.

4.2.3 Non-linearity and focus location

As discussed in the previous sections, the focal quality degrades with increasing amplitude, and the location is shifted downwave due to nonlinear wave-wave interactions. The nonlinear wave-wave interactions effectively redistributes the spectral energy over different frequencies and wavenumbers, generating phase modulation and shifting focal location [43]. This section will try to visualise the nonlinear behaviour present in the different wave events. This will be done by looking at which wave gauge experiences the maximum wave height, thus indicating how far the focal location has shifted. Comparing the maximum measured amplitude with the linear input amplitude will also indicate how much the wave event is affected by nonlinear wave amplification.

Figure 38 shows the different wave events and their measured focal peak at different locations within the measurement area. All the values are normalised with respect to the wave cases' theoretical target amplitude.

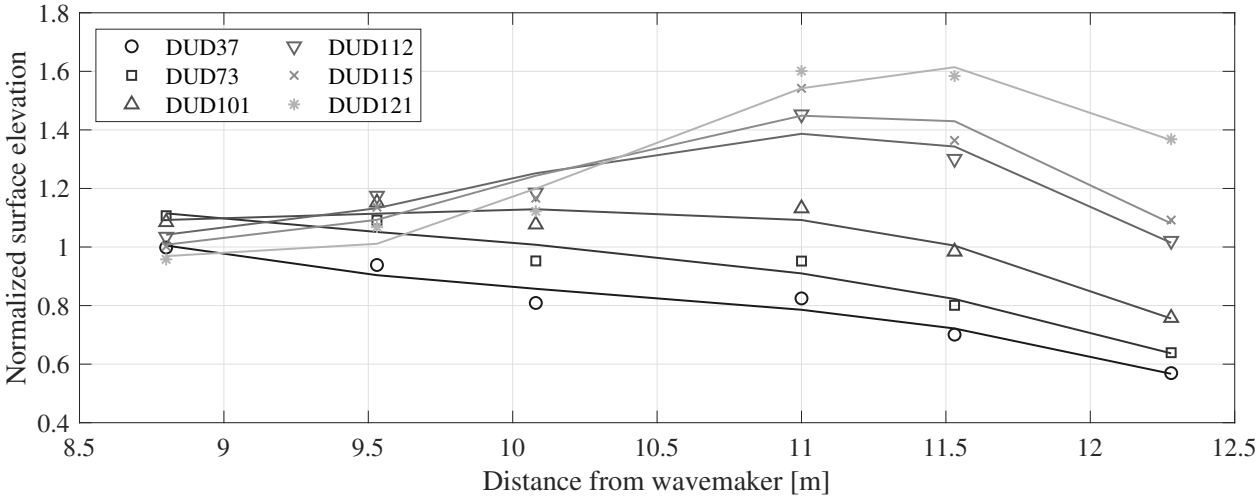

Figure 38: Normalised surface elevation of the focal peak for each DUD wave event at different positions from the wavemaker. Solid line represents a curve fitting for each wave case.

Figure 38 illustrates the nonlinear behaviour. With no presence of nonlinear wave-wave interactions, all the wave events would, to some extent, have followed the DUD37 case marked with circles. However, it can be seen that the top point of the curve shifts in positive x-

direction, which illustrates the downwave movement of the focal position. In addition, the normalised value at the top point of the curve increases for each wave case and is a result of nonlinear wave amplification.

The coarse spatial intervals of the wave gauges in this experiments pose a challenge when trying to follow the focal peak throughout the measurement area and determining the actual focal location. A finer spatial interval of the wave gauges would make the trend observed in Figure 38 clearer. This is, however, challenging due to practical reasons and hardware limitations. However, with the flexibility of numerical wave tanks, this can be achieved, and the actual focal location can be determined with reasonably good accuracy.

Due to the coarse interval of wave gauges, the focal position seems to have shifted the same amount for the three largest events, as can be seen in Table 14. However, the truth is that the actual focal location has probably not been measured due to the relatively large distance between the gauges. The same can be said for the shift in focal time.

Table 14: Nonlinear amplification and shifting in both time and space for the focal location of each experimental DUD wave event. Focal location is defined as the location where the wave events experience their maximum crest.

Wave Case	**Nonlinear amplification** [%]	**Shift in focal position** [m]	**Shift in focal time** [s]
DUD37	+ 0.00	+ 0.00	+ 0.04
DUD73	+ 10.73	+ 0.00	+ 0.00
DUD101	+ 15.14	+ 0.73	+ 0.27
DUD112	+ 45.30	+ 2.2	+ 0.93
DUD115	+ 54.20	+ 2.2	+ 0.91
DUD121	+ 60.17	+ 2.2	+ 0.86

The shift in focal time seems to be decreasing for each wave case that has the same amount of shift in the focal position. Take DUD37 and DUD73 for an example. Here, both wave cases seem to be focusing in the same location. However, the larger DUD73 event, with more

nonlinear behaviour, seems to focus earlier in time and precisely at the desired focal time compared to DUD37. This seems counterintuitive, assuming that more nonlinear behaviour shifts the focal location more in time and space. However, as discussed in Section 4.2.1, this is explained by the actual focus location being somewhere in between the two wave gauges and that the measurements are not the maximum wave height, but measurements close to the maximum.

4.3 BUD - Surface measurements

The surface elevation of the different wave events within the B spectrum is analysed in the present section. Contrary to the DUD events, the target amplitudes in the BUD events consist of only 37, 73 and 95 mm, but the frequency range for this spectrum is significantly larger. This increase in frequency range makes the BUD events evolve differently than the DUD events, even though the same target amplitudes are used in both the D and the B spectra. As well as a broader frequency band, the target focal position for all the BUD cases is changed to 10.08 metres, i.e. wave gauge number three. The target focal time remains at 20 seconds, just like the DUD wave runs. The BUD events will be analysed in the same way as the DUD events. However, the following cases will not be compared directly with Johannessen's experimental data. The BUD cases will to some extent be compared against the DUD cases, and notable differences between such as BUD37 and DUD37 will be addressed.

4.3.1 Surface elevation at the focal location

The focal point for all the BUD cases has been changed to 10.08 metres, where wave gauge number three is located. In the following section, the third wave gauge is, therefore, the only one considered.

BUD37

Similarly to the DUD37 case, BUD37 acted as the reference wave for the calibration and generation of the transfer function for spectrum B. This wave case is assumed to be close to linear, and as Figure 39 shows, the measurements agree well with the linear prediction.

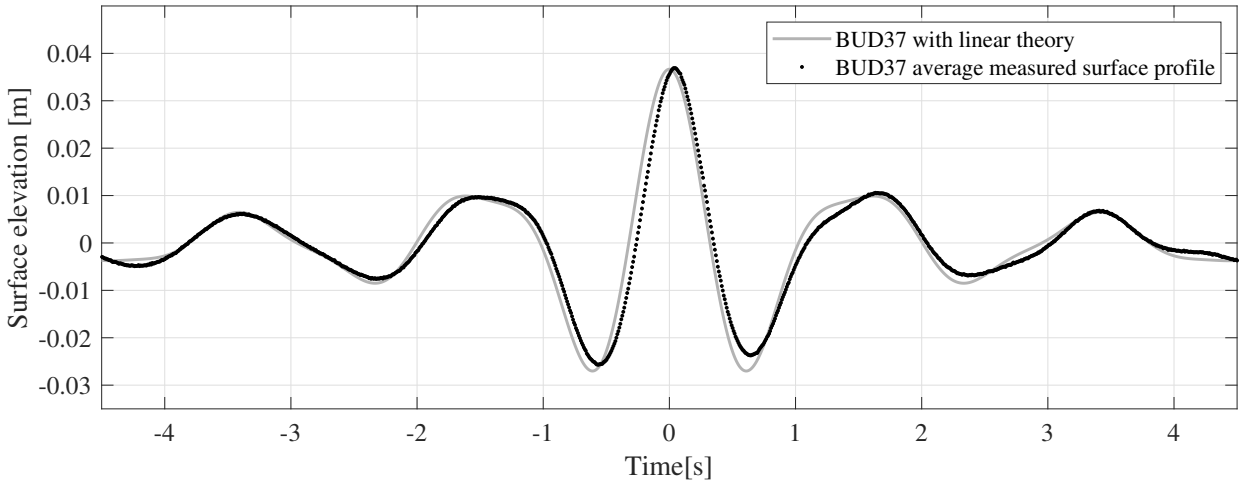

Figure 39: Measured time series of BUD37 at focal location plotted against the linear time series of BUD37. Time is centred around the desired focus time of 20 seconds.

Just as the DUD37 event, the measured time series in Figure 39 experiences a phase shift compared to the linear time series. Once again, this is believed to be caused by hardware errors related to the placement of the wave gauges. As all the wave gauges are mounted to the towing carriage, a slight shift in the position of the carriage will shift all the wave gauges simultaneously. The similarities between the phase shift in Figure 39 and the one observed in the DUD37 case indicates that the distance between the wave gauges is correct, but the placement of the towing carriage might be wrong.

BUD37 is also just considered to be relatively linear, but not exactly linear. The most notable sign of this is the asymmetry at the troughs on each side of the focal peak. Furthermore, minor deviations from the target focal time can not be regarded as a result of nonlinear behaviour when the uncertainty of the wave gauge position is taken into consideration. Hence, the focal quality of the BUD37 wave case is considered to be good. The amplitude of the focal peak is measured to be 36.89 ± 0.55 mm, thus giving a deviation to linear theory of 0.6 %.

BUD73

In the BUD73 case, small nonlinear amplifications start to form. Even though the broad-banded spectrum B results in a significantly different surface profile compared to the cases with the narrow-banded frequency spectrum D, the same nonlinear effects observed in DUD73 can be seen in BUD73. In Figure 40, it can be observed that the focal peak seems to align better with the linear prediction, thus hitting the desired focal time better than the BUD37 event. This is the same as what can be observed for the DUD73 event in Figure 24. Similarly to DUD73, this is explained by the shifting of the focal position and that the maximum measured crest in the target focal position is effectively just a measurement of the surface close to the actual focal peak.

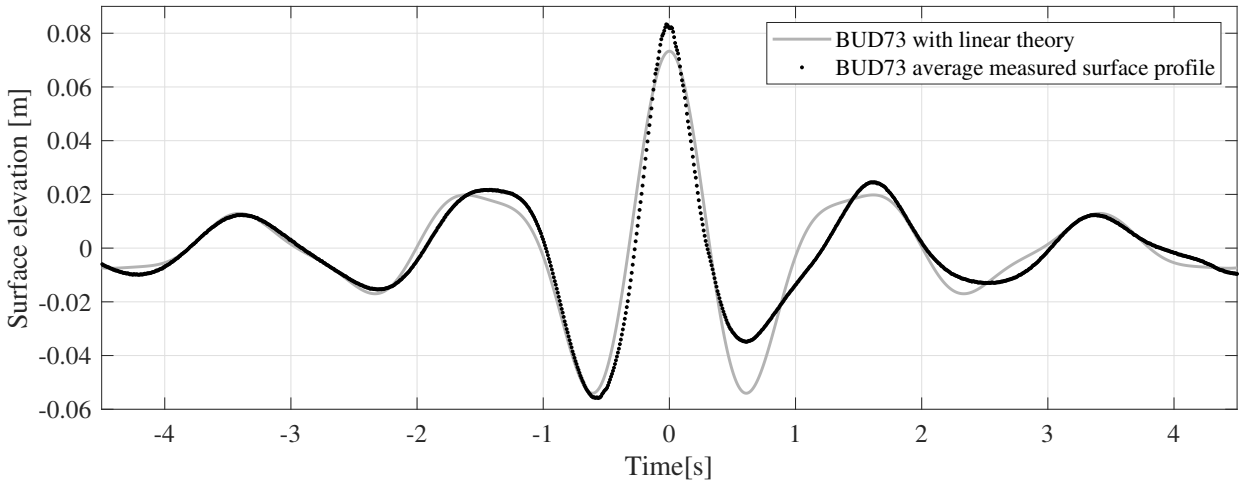

Figure 40: Measured time series of BUD73 at focal location plotted against the linear time series of BUD73. Time is centered around the desired focus time of 20 seconds.

Nonlinear amplification of the crest is also visible in the BUD73 wave run, just as the DUD73 event. The height of the peak in the focal position is measured to be 83.30 ± 0.55 mm, which is equivalent to a deviation to its linear prediction of 13.6 %. This is a more significant deviation compared to the DUD73 event, which has the same target amplitude. From laboratory experiments conducted by Baldock et al. [24], the deviation from the linear prediction should decrease with increasing bandwidth of the input spectrum. This is contrary to what is observed when comparing the crest height in the focal position for the narrow banded event of DUD73 and the broad-banded event of BUD73. However, it is necessary to further investigate

the maximum crest elevation at the actual focal position to determine if the same effects observed by Baldock et al. can be observed in the present experiments.

BUD95

The BUD95 case can not be directly compared to any other event due to its unique target amplitude. Naturally, DUD101 with its target amplitude of 101 mm would be the closest case for comparison. Although the DUD wave runs all have three prominent peaks in the vicinity of the focal position and the BUD events have more or less one single prominent peak, the same effects observed in DUD101 can, to some extent, be seen in the BUD95 event. Figure 41 shows the measured time series for BUD95 at the focal position of 10.08 metres. Just as in the DUD101 case, the focal peak can be seen to reach its maximum prior to the target focal time.

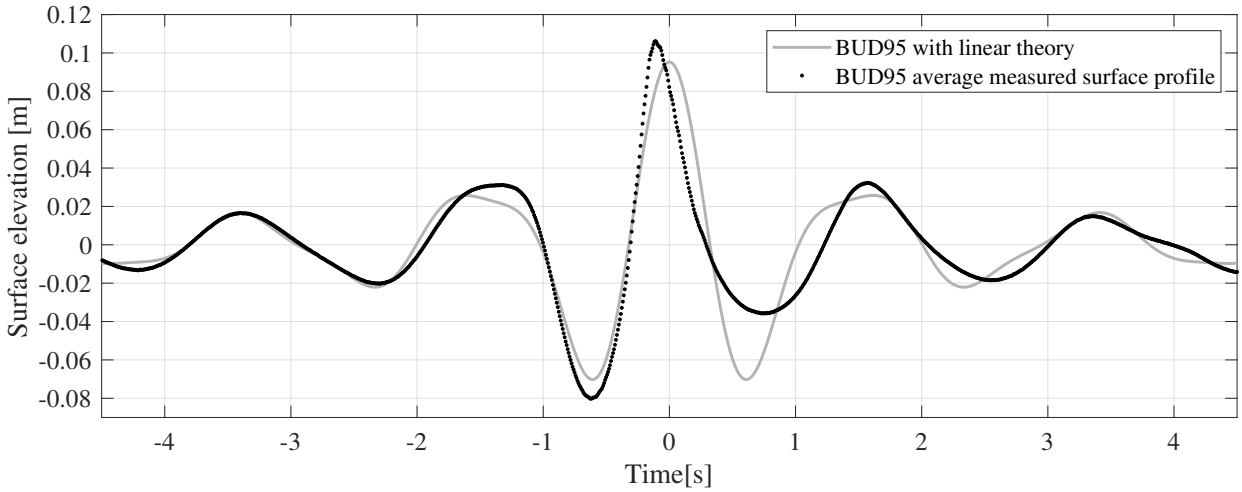

Figure 41: Measured time series of BUD95 at focal location plotted against the linear time series of BUD95. Time is centred around the desired focus time of 20 seconds.

Once again, the asymmetry between the adjacent troughs increases as the target amplitude is increased. This serves as a reasonable prediction that the actual focal position has shifted downwave from its target location. The first peak at approximately 1.3 seconds prior to the focal time was observed to amplify rapidly with increasing target amplitude in the DUD events. This behaviour is not as apparent for the BUD events as the same peak does not appear as prominent. However, it can be observed that this peak is increasing compared to

the linear prediction. It is assumed that by increasing the target amplitude further, the same peak would experience an even higher amplitude, just as in the DUD wave runs.

Summary of BUD wave events at the focal position

The same as with the DUD wave runs, the three BUD wave cases have been normalised to directly compare the differences and effects observed when the target amplitude is increased. This normalised comparison can be seen in Figure 42 where the three BUD time series are displayed. The event with the highest target amplitude, BUD95, is coloured in black, and the two lower events are coloured in lighter shades of grey.

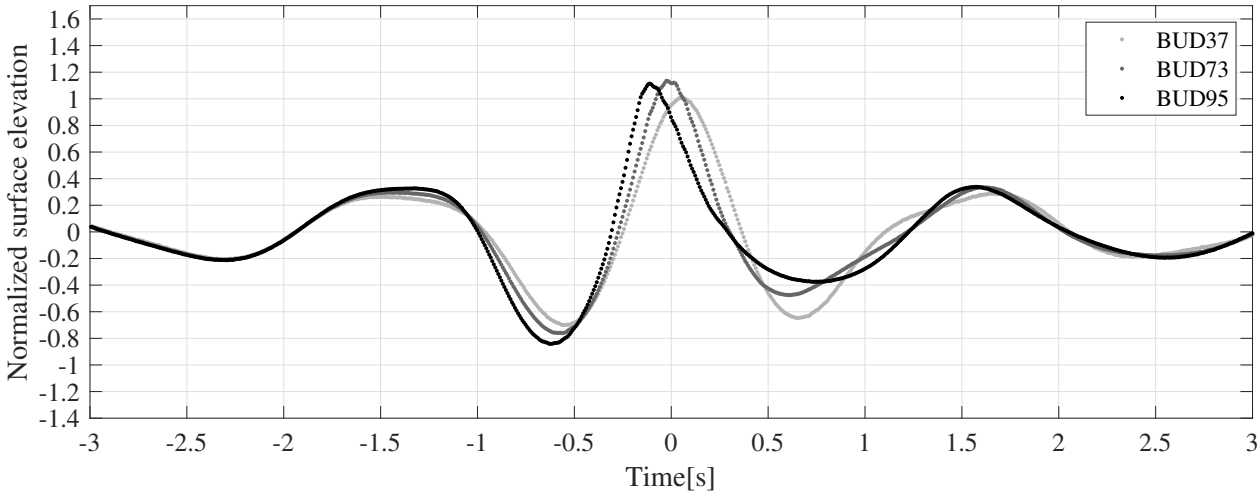

Figure 42: BUD wave events measured at the focal position and normalised with respect to their linear target amplitude.

The gradual widening and decreasing of the adjacent trough, at approximately 0.5 seconds after the target focal time, shows that not all the frequency components are superimposed at the desired focal location. Hence, the assumption of shifting focal location with increasing target amplitude is further strengthened. However, further investigation into the maximum measured crest is necessary to determine how much the focal location has shifted. Table 15 displays different parameters such as crest height at focal location and percentage of deviation to the linear prediction. Contrary to Table 12, only the focal peak has been considered in Table 15. Similar to the same parameters for the DUD events, the calculated deviation in the focal crest remains quite stable and starts to drop off in the cases with the highest target

amplitude.

Table 15: Different parameters for the maximum wave crest measured at the focal position for the BUD wave events.

Wave Case	**Amplitude** [m]	**Linear deviation** [%]	**Calculated steepness** (ka)
BUD37	0.03689	+ 0.61	0.103
BUD73	0.08330	+ 13.59	0.241
BUD95	0.1062	+ 11.40	0.224

Both BUD37 and BUD73, which can be directly compared to DUD37 and DUD73, experience greater steepness than their counterpart. This is a result of both higher linear deviation of the crest and shorter wave periods. The wave period of BUD37 is measured to be approximately 1.18 seconds, which is less than the DUD37 case, which had a wave period of approximately 1.33 seconds. This leads to the assumption that BUD wave cases will reach the ultimate threshold for steepness at lower target amplitudes than the DUD wave events. This will be addressed in the following section.

4.3.2 Surface elevation at point of maximum crest

The previous section covered all the measurements at the focal location for the BUD wave cases. In order to determine the actual focal location and the overall maximum wave crest, it is necessary to investigate measurements from the other wave gauges. As the focal position for the BUD cases is set to 10.08 metres, there are only four wave gauges between the focal position and the end of the measurement area, including the wave gauge at 10.08 metres. This setup limits how much the focal position can shift and still be detected. However, with the increase in bandwidth, the focal position is assumed to shift to less extent than the narrow banded DUD events.

As can be seen in Figure 43, the measured time series at the focal position is more or less symmetrical on each side of the crest. This particular time series were analysed in Section 4.3.1 and its maximum crest was measured to be 36.89 ± 0.55 mm, just above its linear target amplitude of 36.67 mm.

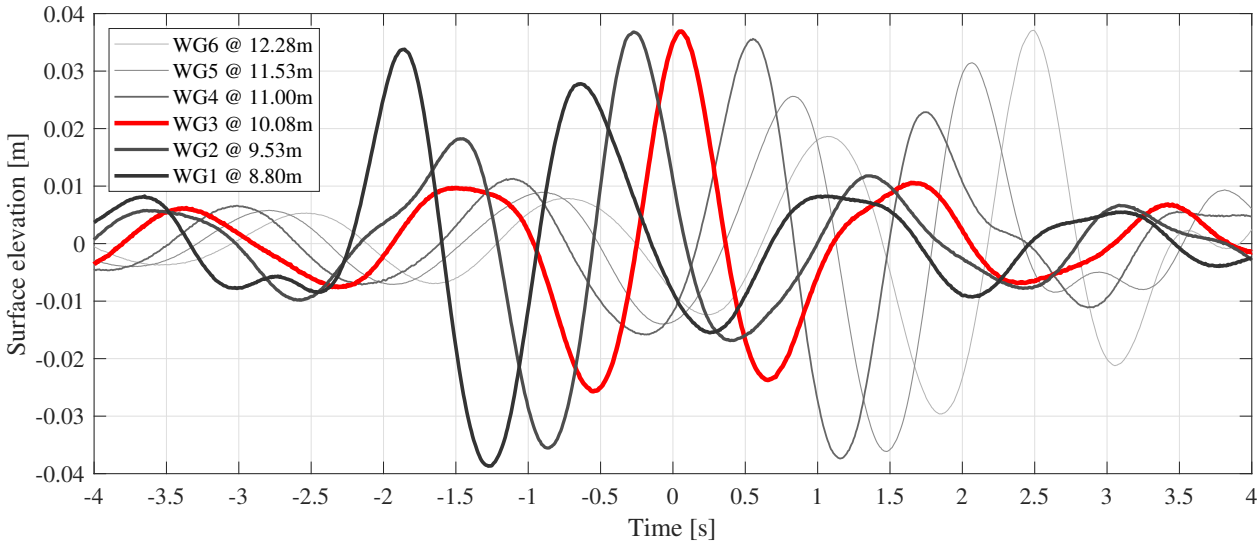

Figure 43: BUD37 wave event with all six wave gauges

The more interesting observations can be done in Figure 44 and 45. These time series marked in red display the maximum crest elevation measured for all the wave gauges. Contrary to the BUD37 event, these two wave events are measured to be maximum at the fourth wave gauge positioned at 11.00 metres. In the BUD73 event, the maximum crest elevation is measured to be 85.93 ± 0.55 mm, somewhat higher than the measurements from the focal location displayed in Table 15. With maximum crest elevation measured to be slightly above the measurements in the focal position, it is fair to assume that the actual focal position and the point of maximum crest elevation are located about halfway between wave gauge 3 and wave gauge 4. This assumption is further strengthened by looking at Figure 44, where a hypothetical wave gauge position in between the third and fourth wave gauge probably would have measured a higher crest elevation.

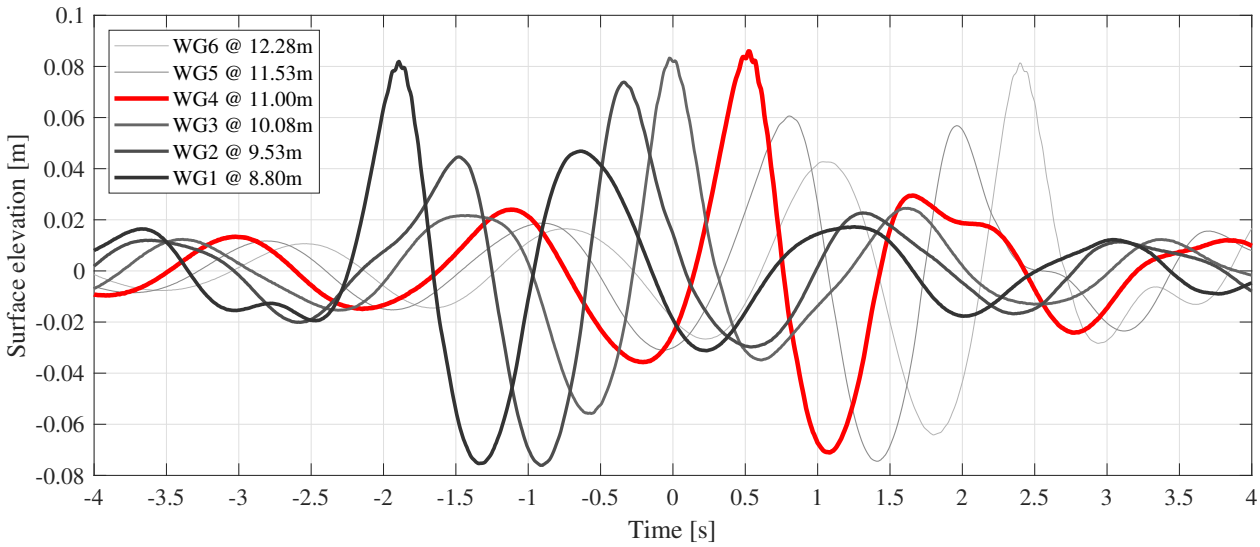

Figure 44: BUD73 wave event with all six wave gauges

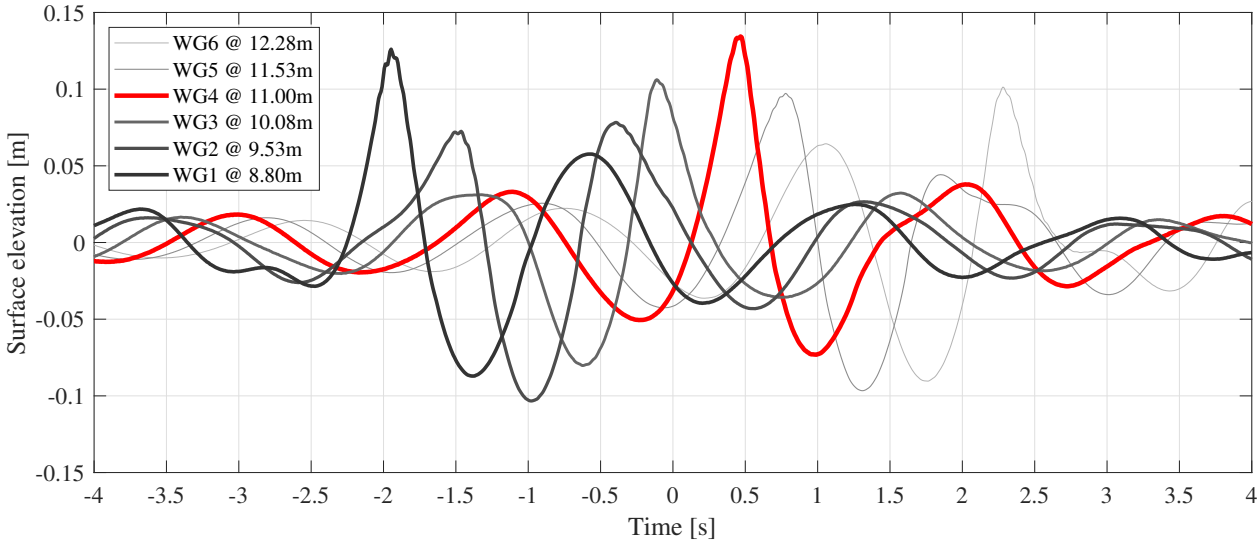

Figure 45: BUD95 wave event with all six wave gauges

By applying the same way of thinking on Figure 45, it becomes clear that the time series marked with red is measured just in the vicinity of the actual focal position. The maximum crest elevation measured for this time series is 134.4 $\pm$ 0.55 mm and is believed to be more or less the actual maximum crest height experienced in the wave tank. Table 16 summarises the different wave events and measurements from the wave gauge which experiences the maximum crest.

Table 16: Different parameters for the maximum wave crest measured in all BUD wave cases.

Wave Case	Maximum amplitude [m]	Linear deviation [%]	Calculated steepness (ka)	Wave gauge number	Time since focal time [s]
BUD37	0.0369	+ 0.61	0.103	3	+ 0.04
BUD73	0.0859	+ 17.18	0.208	4	+ 0.52
BUD95	0.1344	+ 40.98	0.376	4	+ 0.47

All the BUD events experience steeper waves compared to the DUD cases with the same target amplitude. Notably, BUD95 has a steepness parameter calculated to be 0.3756, which is significantly higher than for the maximum peak in the DUD101 event, where the same parameter is calculated to be 0.2808. Also, the linear deviation is, in general, higher compared to the narrow banded DUD events. This is in contrast to observations done by Baldock et al. [24], which highlights that nonlinear wave-wave interactions are strongly bandwidth dependent and that the largest nonlinear wave-wave interactions occur at the narrow-banded spectrum D. However, with a coarse spacing of the wave gauges, it is believed that the actual maximum wave crest has not been measured. This might be the cause of the discrepancies between the present experiment and the investigation carried out by Baldock et al. [24].

4.3.3 Non-linearity and focus location

According to Baldock et al., the broadening of the frequency range will reduce the down-shift of the focal point. Contrary, an increase in the target amplitude will shift the focal position downwave in the tank [24]. As spectrum B represents a more broad-banded spectrum, it is expected that the extent of the downstream shifting of the focal position will be less than for the narrow-banded spectrum D events. By investigating the focal crest of the three different BUD events, it is possible to determine how much the focal position has shifted. Figure 46 shows the three BUD events normalised and how the crest elevation of the focal peak changes as it passes through the measurement area.

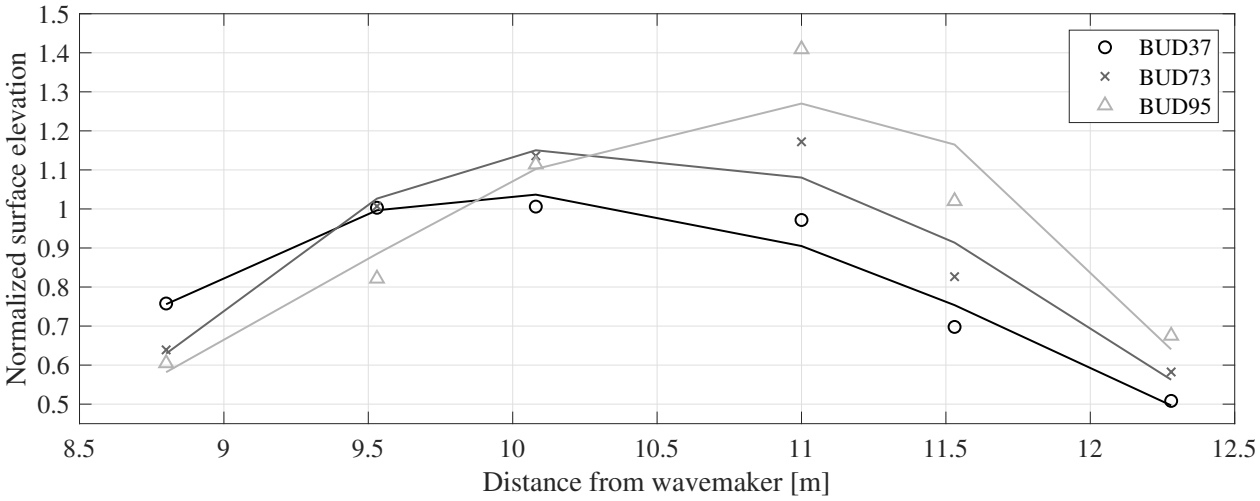

Figure 46: Normalised surface elevation of the focal peak for each BUD wave event at different positions from the wavemaker. Solid line represents a curve fitting for each wave case.

As the focal location for the BUD wave events is changed to 10.08 metres, it is expected that a close to linear event would act symmetrically about this point. BUD37 is seen to almost take this shape, but with the wave gauges distributed asymmetrically about this point, some deviation is expected. Results displayed in both Figure 38 and 46 are well in line with the numerical simulations conducted by Lande et al. [18]. His numerical calculation for the same wave spectra and scaled-down amplitudes show the same trend, which can be seen in the mentioned figures. The BUD37 wave event form a fairly symmetrical curve about the target focal position. However, the curves' top point increases and shifts downstream compared to the target location when the target amplitude is increased.

Table 17: Nonlinear amplification and shifting in both time and space for the focal location of each experimental BUD wave event.

Wave Case	**Nonlinear amplification** [%]	**Shift in focal position** [m]	**Shift in focal time** [s]
BUD37	+ 0.61	0	+ 0.05
BUD73	+ 17.18	+ 0.92	+ 0.52
BUD95	+ 40.98	+ 0.92	+ 0.47

With the coarse spatial setup of the wave gauges, the focal location of BUD73 is measured to shift 0.92 metres which are significantly more compared to the similar DUD73 event. However, as discussed in Section 4.3.2, it is assumed that the actual focal location is somewhere in between 10.08 metres and 11.00 metres. Hence, these measurements, with the coarse setup of wave gauges, are not sufficient to confirm the observations made by Baldock et al. [24], which demonstrates that an increase in bandwidth will reduce the downstream shifting of the focal position, while an increase in target amplitude will increase the downstream shifting.

4.4 JONSWAP-focused wave groups

The following section leaves behind the truncated wave spectra B and D and considers a full JONSWAP defined wave spectrum. As these following experiments are not based on previous experiments, the analysis is limited to only the measurements obtained in the present experiment and predictions by linear theory. Furthermore, due to practical reasons and cooperation with another project, the focal position for the JONSWAP cases was moved to 11 metres which correspond to wave gauge number four. Also, the spatial distribution of the wave gauges has been changed in JONSWAP wave events, restricting the analysis to wave gauge number one and four positioned at 8.8 metres and 11 metres, respectively. The following sections will analyse how the two different JONSWAP wave events compare to linear theory. Parameters such as crest steepness and nonlinear amplification will be addressed. The same method used to calculate energy spectral density for the truncated wave spectra are used in the JONSWAP wave events.

4.4.1 Energy spectral density

The most notable distinctions between the previous wave events and the following JONSWAP cases is the absence of clearly defined cut-off frequencies. In Figure 47, the two different sea states which are analysed are defined with spectral energy. Both wave cases are defined with the same significant wave height. However, the peak period distinguishes the two.

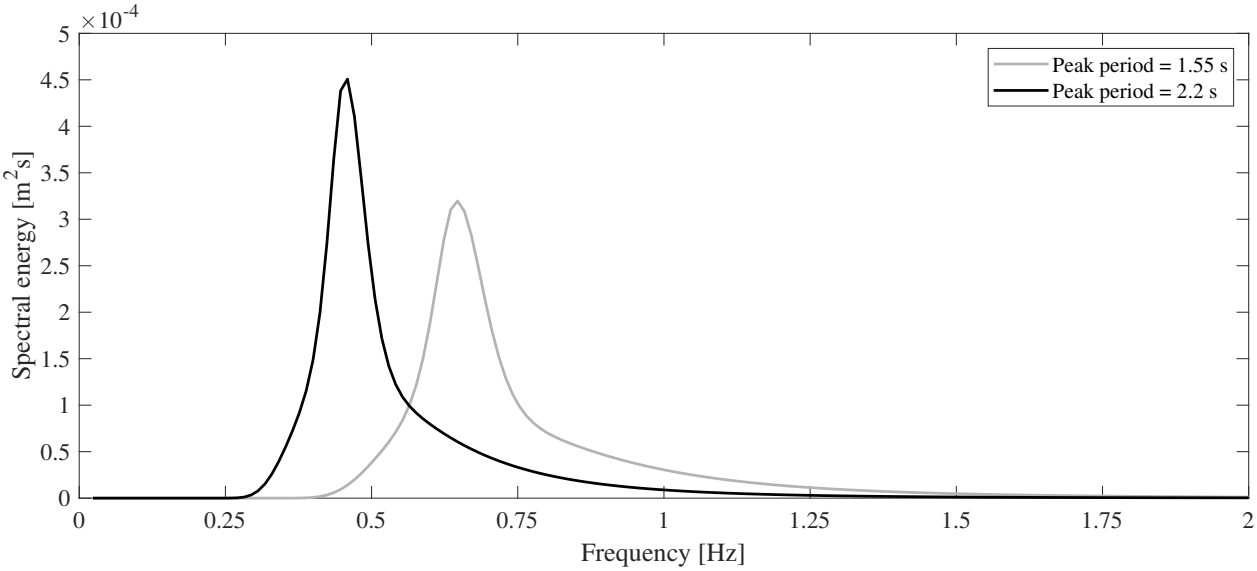

Figure 47: JONSWAP defined wave spectra used in the experimental cases.

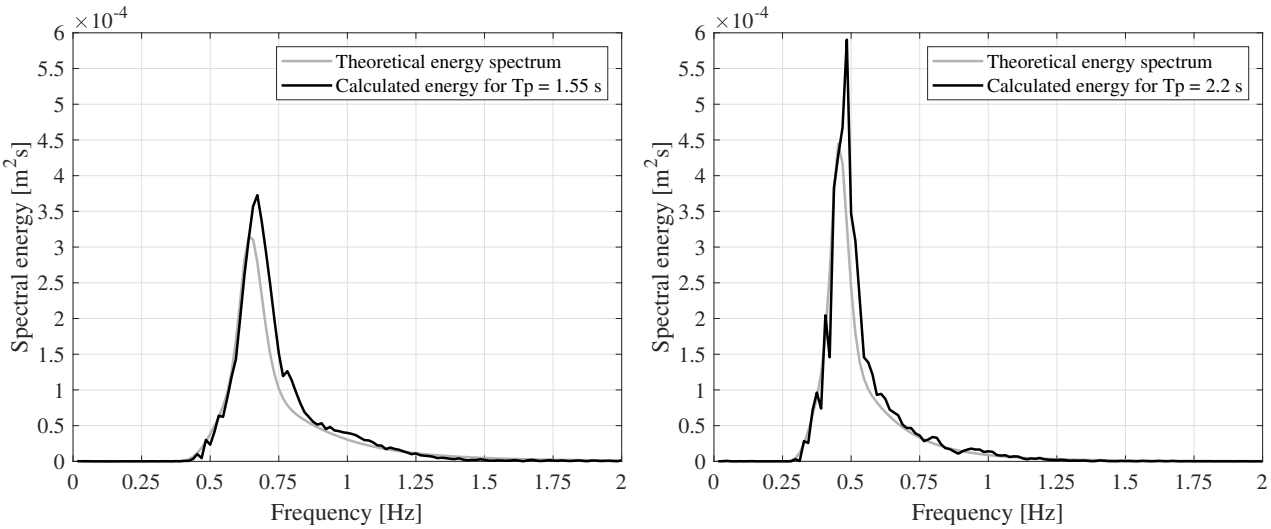

(a) Tp = 1.55 seconds

(b) Tp = 2.2 seconds

Figure 48: Energy calculations compared to theoretical energy spectrum for both JONSWAP wave events.

The calibration method described in Section 3.2.5 yields good results for the spectral energy in the JONSWAP wave events. Figure 48 shows both JONSWAP wave events with peak period equal to 1.55 seconds and 2.2 seconds in Figure 48a and 48b, respectively. The black line marks the measured and calculated energy spectrum, while the grey line is the theoretical target spectrum. As a result of reducing the spectral repeat time for the JONSWAP events

to 64 seconds, no frequency resolution errors were present in the calibration of the wave runs. Hence, the development and implementation of the transfer function yield a more accurate output with less fluctuating frequency components. Nonetheless, the calculated energy spectrum can be observed to overshoot the theoretical target spectrum.

Other than observing Figure 48, the accuracy of the measured and calculated energy spectrum can be determined with the parameters in Table 18. The RMSE-value is calculated with respect to the theoretical energy spectrum and is given with the same units as the input spectra. A lower m_0 deviation percentage indicates a better fit with the theoretical spectrum, and this parameter can be directly compared to the same calculation for the DUD events listed in Table 10.

Table 18: Energy calculations of measured energy spectrum for JONSWAP defined spectra with both $T_p = 1.55$ seconds and $T_p = 2.2$ seconds.

Wave Case	**RMSE** [$\mathbf{m^2 s}$]	$\boldsymbol{m_0}$ **deviation** [%]	**Linear peak deviation** [%]
$\boldsymbol{T_p = 1.55}$ **s**	$1.52 \cdot 10^{-5}$	+ 73.9	- 13.1
$\boldsymbol{T_p = 2.2}$ **s**	$1.82 \cdot 10^{-5}$	+ 74.9	- 13.3

From observations done in Figure 48, it is assumed that the actual spectral energy content would be greater than the theoretical. However, over 70 % increase in the zeroth-order moment is surprisingly large considering that the crest elevation in the focal position is approximately 13 % less than the linear prediction. By natural assumption, it follows that an increase in spectral energy content would yield a greater crest elevation at the focal location.

One explanation for why the deviation in the zeroth-order moments is significant for the JONSWAP cases might be the absence of clearly defined cut-off frequencies. As the energy content in the frequency components close to 0 Hz and 2 Hz approaches zero, small deviations will yield a large percentage. However, this does not fully explain the significant deviation of

74 % and 75 % as the energy contribution from these particular frequency areas are negligible compared to the area around the peak.

4.4.2 Surface elevation

Wave events conducted in the JONSWAP experiments are only limited to two cases. As both these two cases have been defined with the same significant wave height, the analysis in the following section is limited to differences in the surface elevation caused by the change in peak period. Deviation compared to linear prediction and the steepness of the focusing crest will also be addressed.

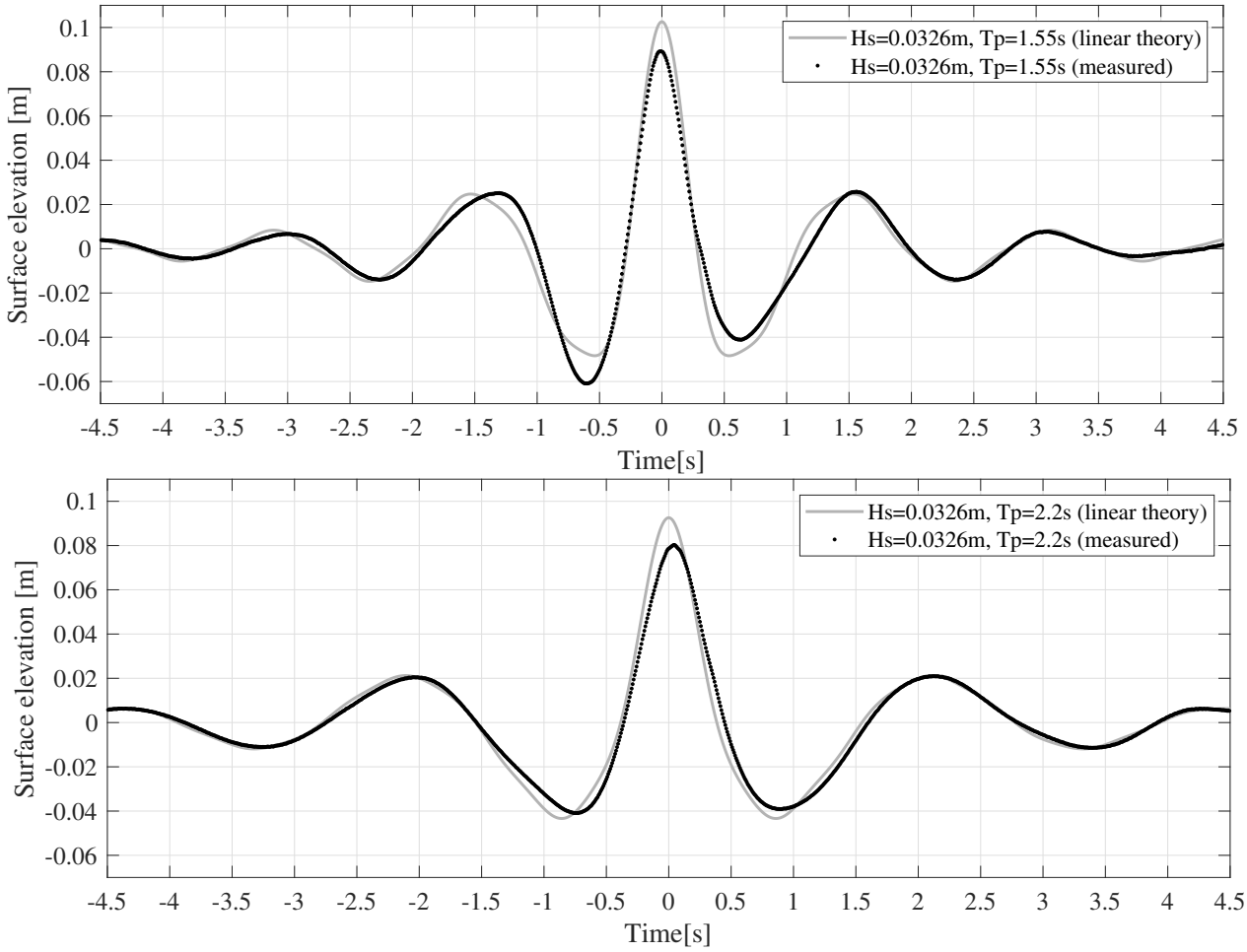

Figure 49: Measured surface elevation for both JONSWAP events with $T_p = 1.55$ seconds (top) and $T_p = 2.2$ seconds (bottom) compared against its respective linear prediction.

Figure 49 displays the two wave cases with their respective linear prediction. Both time series can be seen not fully to reach their target amplitude, and the linear deviation of approximately 13 % from Table 18 can be observed. A shift in the focal position can explain this and that not all the frequency components are superimposed at the location of the wave gauge. However, a near symmetrical surface profile can be observed in the bottom wave event in Figure 49, indicating that the focal quality is good for this particular wave event. With a peak period of 2.2 seconds, this wave case acts fairly linear, indicating that the deviation in crest elevation is caused by a lack of energy in the input to the wavemaker.

It can be observed that the JONSWAP event with a peak period of 1.55 seconds results in a steeper focal crest than the event with a peak period of 2.2 seconds. This observation is well in line with expectations considering that the majority of the energy in the 1.55-second event travels with a higher frequency, or shorter wavelength, and further, a larger wavenumber. The observations from Figure 49 is further strengthened by the steepness calculations in Table 19.

Table 19: Parameters for the maximum wave crest measured at the focal position for the JONSWAP wave events.

Wave Case	**Amplitude** [m]	**Linear deviation** [%]	**Calculated steepness** (ka)
$\boldsymbol{H_s = 0.0326}$ **m,** $\boldsymbol{T_p = 1.55}$ **s**	0.08923	- 13.1	0.237
$\boldsymbol{H_s = 0.0326}$ **m,** $\boldsymbol{T_p = 2.2}$ **s**	0.08026	- 13.3	0.122

Although the breaking limit for the JONSWAP events was not investigated, the results clearly display the effects of changing the peak period in terms of wave steepness. If scaled up, both of these wave events represent real-time conditions experienced at sea. The event with a peak period of 1.55 seconds would, in a scaled-up situation, represent a rogue wave at approximately 3.3 metres. This is significant compared to the scaled-up significant wave height of 1.2 metres.

4.5 Repeatability of focused wave groups

The focused wave groups showcase high stability compared to regular waves. When conducting an experimental test campaign, where one particular wave height or crest steepness is desirable, focused wave groups will, in many cases, be the desired choice. Furthermore, the calculated steepness parameter for some of the highest waves in this study would be impossible to achieve for the same amplitudes when using regular waves. Previous experiments with regular waves conducted at HVL has displayed some of the disadvantages and instability of these particular waves. During those experiments, it was observed that the first couple of waves in the regular wave train more or less always reached higher amplitudes than the desired input amplitude. As the regular wave train passes the wave gauge, the amplitudes slowly decrease and eventually tip below the input amplitude in some cases. Contrary, the focused wave groups only experience one target amplitude at a given location and time. The focused wave group can reach precisely the desired crest elevation with sensible and adequate calibration and input amplitude.

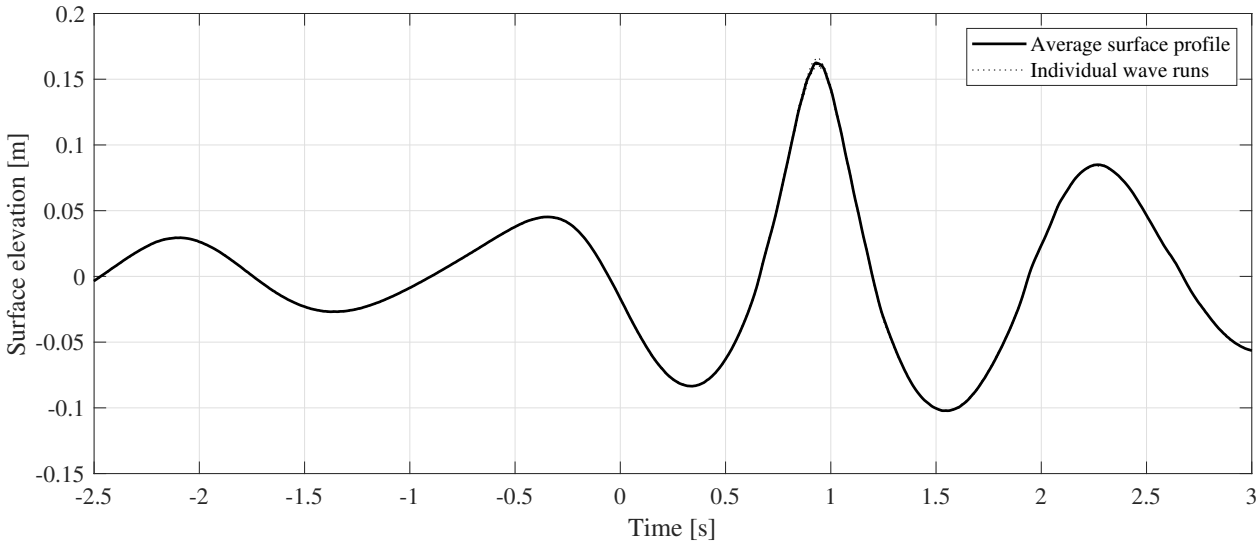

Figure 50: Five individual time series of DUD112 measured at wave gauge number 4 with solid line being the average surface elevation.

The DUD112 wave event was conducted five times with approximately 10 to 15 minutes between the runs to calm the water. Figure 50 displays the five individual time series measured

at wave gauge number four.

Figure 50 demonstrates the stability of the focused wave group and the only place the individual wave runs can be barely seen to deviate from the average is at the maximum crest. The same observations were made for all the other wave events, and a modest increase in the deviation was seen along with increasing target amplitude. Figure 51 offers a closer look at the peak from Figure 50 and the minor deviations between the individual wave runs and the average can be seen.

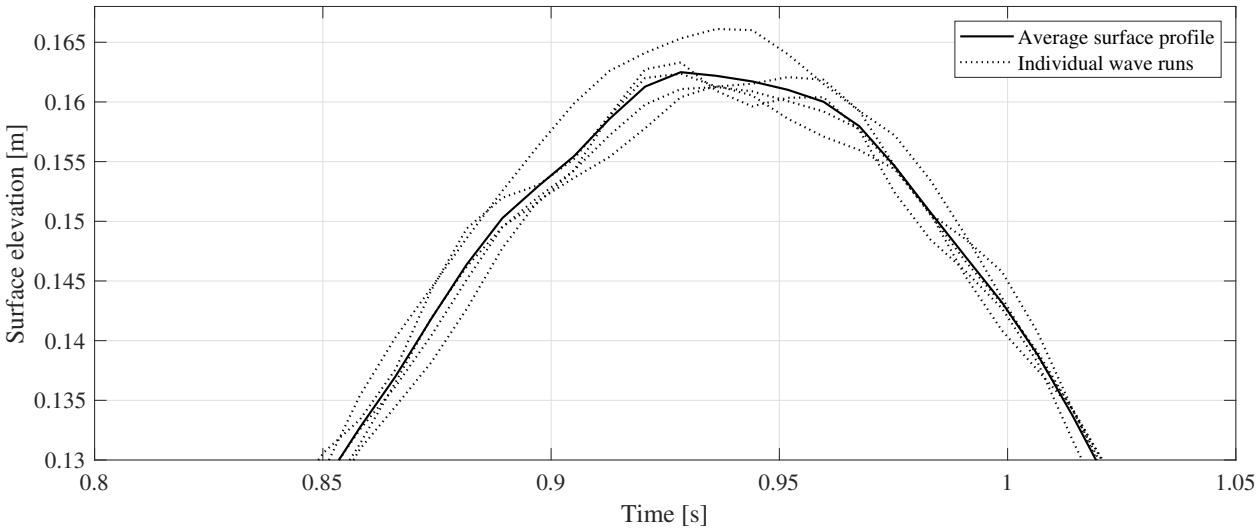

Figure 51: Five individual time series of DUD112 measured at wave gauge number 4 and zoomed in at the maximum crest elevation with solid line being the average surface elevation.

Once again, the relative minor deviations in crest elevation can be observed and that the maximum deviation is measured at the peak. The same deviation is seen to decrease further away from the peak. All the different wave cases in the present study and their individual wave runs are summarised in Table 20. The overall maximum crest elevation for each respective wave run is listed, and the average deviation compared to the wave events' average maximum. For comparison, a regular wave train with a target amplitude of 0.0562 metres and a wave period of 1.47 seconds has been included.

Table 20: Measured maximum amplitude for all wave events with average deviation compared to its respective average time series.

Wave Case	Average amplitude [m]	Run 1 [m]	Run 2 [m]	Run 3 [m]	Run 4 [m]	Run 5 [m]	Average deviation [%]
DUD37	0.0366	0.03685	0.03662	0.03646	-	-	± 0.4
DUD73	0.0812	0.08089	0.08122	0.08158	-	-	± 0.3
DUD101	0.1161	0.1171	0.1172	0.1176	-	-	± 1.0
DUD112	0.1625	0.1614	0.1633	0.1612	0.1624	0.1661	± 0.8
DUD115	0.1781	0.1780	0.1785	0.1780	-	-	± 0.1
DUD121	0.1938	0.1929	0.1941	0.1966	-	-	± 0.7
BUD37	0.0369	0.03716	0.03715	0.03667	-	-	± 0.7
BUD73	0.0859	0.08541	0.08678	0.08610	-	-	± 0.6
BUD95	0.1344	0.1314	0.1353	0.1367	-	-	± 1.5
$\boldsymbol{T_p = 1.55}$ **s**	0.08923	0.0893	0.08879	0.0898	-	-	± 0.4
$\boldsymbol{T_p = 2.2}$ **s**	0.08026	0.08118	0.08022	0.07948	-	-	± 0.7
Regular*	0.05845	0.0607	0.05673	0.05888	0.05737	0.05857	± 1.9

*Five random peaks in regular wave with $A_{reg} = 0.0562$ m and $T = 1.47$ s.

Even though only one regular wave train was included for the sake of comparison, the difference becomes apparent in Table 20. The average deviation for all the focused wave events is ± 0.64 %, less than half the deviation seen in the regular wave run. A more thorough investigation into the differences between regular waves and focused waves regarding stability and repeatability is needed to determine the actual difference. However, results from Table 20 and observations throughout the experimental testing indicate that focused waves act significantly more stable than regular waves.

Furthermore, no significant deviations in the phase from wave run to wave run were observed in the focused wave events. This can be seen in Figure 50 where all the five individual wave runs are hidden behind the solid line indicating the average of the five. Based on these

observations and calculations, it is fair to say that the focused wave groups showcase high stability and that they are highly repeatable with low levels of deviation from wave run to wave run.

4.6 Measurement database

All of the measurements presented in the previous sections will be made available in an open database, free to use for validation of numerical wave tanks. This section aims to describe how the data file is structured and the content of the database. The input file for the different wave events and the registered paddle motion of the wave generator will be made available. However, the data publication will remain on hold until the thesis has been approved and all guidelines and regulations from the University in terms of publishing are met. Therefore, to avoid misuse of the experimental data, the publication of the data aims to be presented in an additional publication within six months of the approval of the current thesis.

The first column in the measurement data file is time. Following this column, the next six columns are the position of each wave generator flap given as an angle in radians between the vertical position and its current position. The following six columns are the data collected from the wave gauges described in Section 3.2.2. Element 1 will correspond to the first wave gauge, element 2 to the second and so on.

The data is structured in folders corresponding to the name of the wave event, such as BUD73 and DUD112, for instance. Within these folders, there is another set of folders named *Original* and *Transfer function*. Files within these folders will contain measurements from the wave event with the theoretical input and wave events with gain corrected input. At least three repetitions for the same wave event are conducted and presented in the given sub-folders. In addition, the input for each wave event is uploaded together with the measurements. Note that the structure of the folders can change depending on the platform used to publish the data. Nonetheless, the data files will be accurately named according to the name of the wave event.

5 Numerical Simulations of Wave Groups

The CFD code introduced in Section 3.3 has been used to simulate some of the wave events investigated from the experimental campaign. The following chapter investigates the numerical wave events and compares them against the experimental data presented in Chapter 4. This chapter aims to quantify how well the numerical simulations represent the experimental data focusing on nonlinear wave amplitude amplification, the shift in focal position and crest steepness. All of the wave events within the DUD wave group have been recreated, in two dimensions, in the numerical wave tank.

5.1 Surface elevation

The following section investigates the surface elevation measured in the numerical wave events. Results from Basilisk will be compared with the measured surface profile from the experimental results. The two positions of interest are the theoretical focal position and the position of maximum crest elevation, i.e. the true focal position. To compare these two situations, only data from the wave gauges positioned at the same location as in the experimental setup will be considered in the following sections.

5.1.1 Focal position comparison

The theoretical focal position for the numerical waves is the same as in the experimental campaign, 8.8 metres. In this section, the numerical time series of DUD37, DUD112 and DUD121 are compared to both the experimental time series and the analytical time series calculated assuming linear wave theory.

The close to linear DUD37 wave event is displayed in Figure 52. Both the numerical and experimental time series are seen to agree well with each other, with the numerical event slightly overshooting the experimental measurements at the focal peak. Notably, both the

numerical and experimental measurements experience a phase shift compared to the linear time series. This observation strengthens the validity of the experimental measurements and indicates that at least the first wave gauge in the experimental setup is positioned at the correct distance from the wave generator.

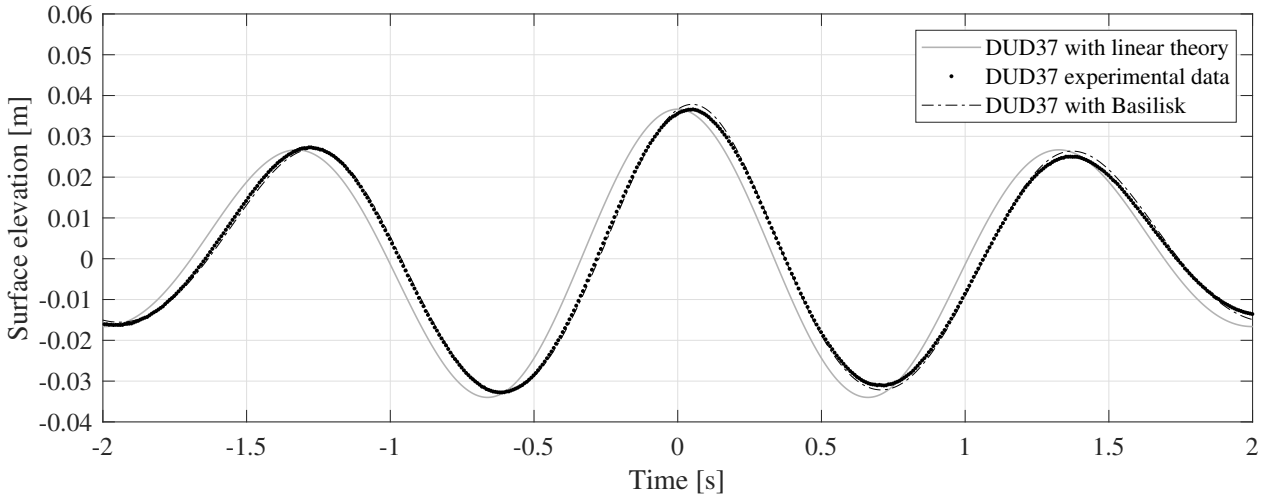

Figure 52: Numeric time series of DUD37 compared against experimental time series and time series computed with linear wave theory.

The DUD112 and DUD121 events are displayed in Figure 53. Here, the deviations between the experimental and numerical measurements become more significant. However, the measurements presented in Figure 53 serve as the first indication that the numerical solver is well equipped to capture the nonlinear effects present in these larger wave events. This observation is in line with previous work done using Basilisk for uni-directional focused waves [18]. Deviations between the experimental data and the numerical simulations are, as expected, more significant in the DUD121 event compared to DUD112 due to effects caused by the presence of strong nonlinear wave-wave interactions.

Furthermore, it is assumed that in a wave event with a larger input amplitude than DUD121, the numerical tool would struggle to recreate the surface elevation measured. Any wave event with an input amplitude larger than 121 mm for the DUD wave groups would result in breaking waves with the present configuration. Measuring surface elevation accurately for breaking waves is a demanding task for any numerical tool. Nevertheless, for the non-

breaking waves presented in this thesis, the two-phase Basilisk solver is seen to capture the nonlinear effects well.

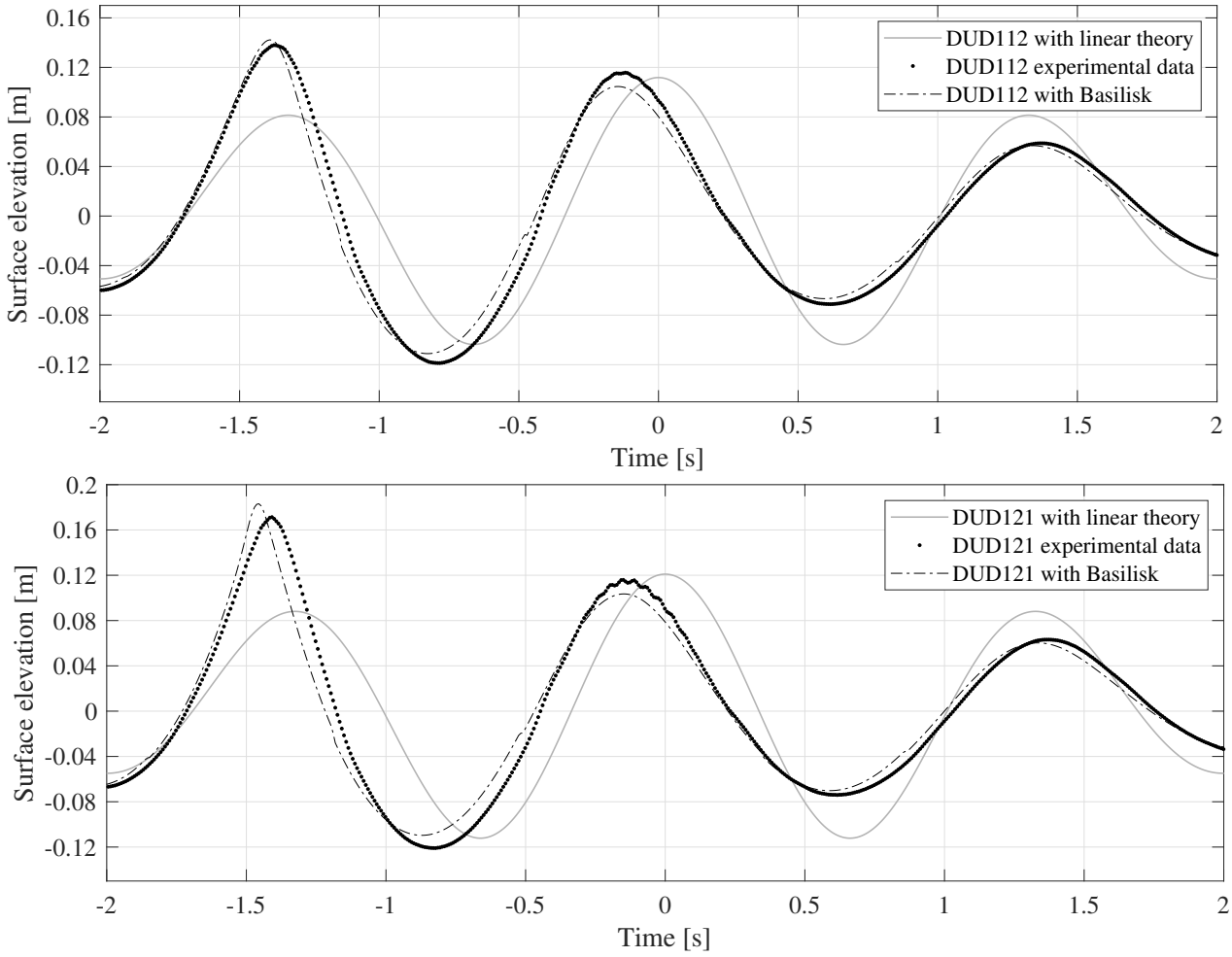

Figure 53: Numeric time series of DUD112 (top) and DUD121 (bottom) compared against its respective experimental measurements and linear time series.

5.1.2 Point of maximum crest comparison

The most significant wave amplitude amplification, caused by nonlinear wave-wave interactions, are present at the point of maximum crest. This is the location of the actual focal position, and Figure 54 showcase the measured time-trace at wave gauge number four for wave event DUD112 and DUD121. The linear wave event of DUD37 has not been included in this section as this wave event experiences its maximum crest at the target focal loca-

tion displayed in Figure 52. Details of maximum amplitude for all DUD wave events, both numerical and experimental, can be seen in Table 21.

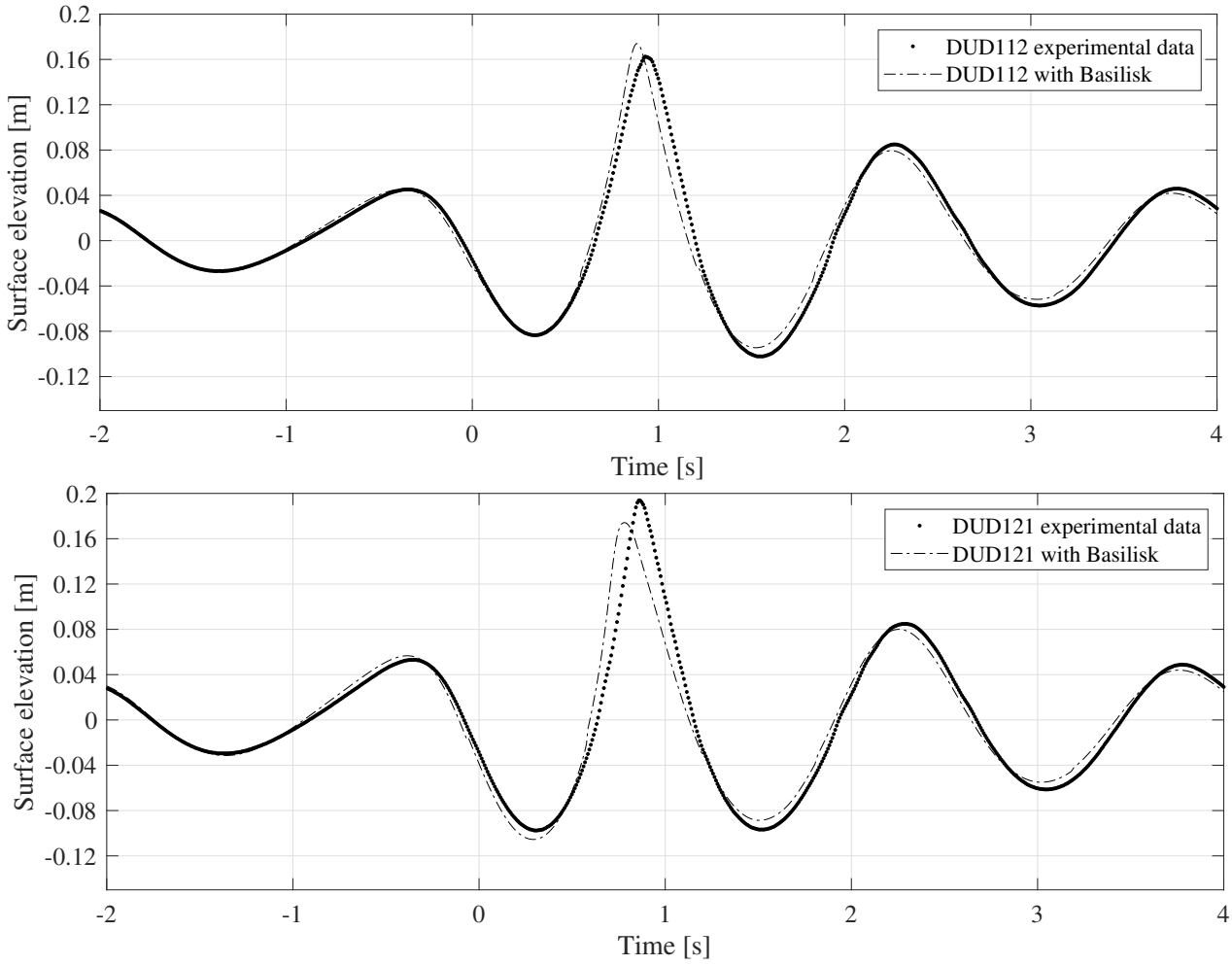

Figure 54: Numerical time series of DUD112 (top) and DUD121 (bottom) compared against its respective experimental measurements.

For both DUD112 and DUD121, the numerical results agree well with the measurements collected from the position of the maximum crest. However, the numerical solver is seen to deviate more for the larger DUD121 event, just as observed in the previous section and Figure 53. Notably, the big difference between the two numerical time-traces, displayed in Figure 54, is the overprediction of the crest for DUD112 and the underprediction of the crest in DUD121. Previous simulations of these particular wave groups reveal that the Basilisk solver tends to over-predict the crest height [18], contrary to what is observed in the numer-

ical wave event of DUD121. It is believed that the significant presence of nonlinear effects in DUD121, caused by nonlinear wave-wave interactions which effectively redistributes the energy to different frequencies and wave-numbers within the wave spectrum [43], could serve as a possible explanation as to why the Basilisk solver struggles to recreate the measured time-trace.

The measurements of maximum amplitude for all of the wave events within the DUD wave group are summarised in Table 21. The deviation listed in the table indicates how much the numerical solver overestimates the crest height. The deviation presented in Table 21 is defined as the difference between the numerical and experimental measurements and given as a percentage of the experimental measurement. The numerical crest elevation is collected from the same wave gauge as the one experiencing maximum crest in the experimental wave runs.

Table 21: Comparison of maximum crest elevation, measured at the position of the experimental wave gauges, for all wave events. Deviation is defined as the difference between the numerical and experimental measurements, and given as a percentage of the experimental measurement.

Wave event	**Experimental [m]**	**Basilisk [m]**	**Deviation [%]**
DUD37	0.0366	0.0378	+ 3.3
DUD73	0.0812	0.0858	+ 5.7
DUD101	0.1161	0.1362	+ 17.3
DUD112	0.1625	0.1741	+ 7.1
DUD115	0.1781	0.1846	+ 3.6
DUD121	0.1938	0.1743	- 10.1

Investigation into the numerical results shows that the Basilisk solver overestimates the surface elevation in all wave events except for the DUD121 event displayed at the bottom of Figure 54. Nevertheless, it is worth mentioning that even with the same setup of wave gauges in the numeric event, some of the numerical wave events experienced maximum crest elevation at a different wave gauge compared to the experimental result. For instance, in the

experimental wave event of DUD121, the maximum crest was measured to be 0.1938 metres for wave gauge number four positioned at 11.00 metres. However, in the numeric simulations of DUD121, the maximum crest was measured to be 0.1972 metres, and this time at wave gauge number five positioned at 11.53 metres. Furthermore, if the experimental and numeric event of DUD121 were compared with crest elevation from wave gauge number four in the experimental, and number five in the numeric, the deviation listed in Table 21 would change from -10.1% to $+1.8\%$. This is more in line with deviation from the other wave events.

5.2 Shift in focal location

A numeric wave tank offers the possibility to measure the surface elevation for any pre-defined position within the wave tank. This feature opens up the possibility to examine the true focal location to a much more accurate extent than as can be achieved in the experimental investigation. In all the numerical wave events, a total of 36 wave gauges, evenly distributed throughout the measurement area, has been used. The separation distance between the numerical wave gauges is set to 10 cm, starting from 8.8 metres. To compare the numeric data with the experimental data, numerical wave gauges positioned close to the position of the experimental gauges have been moved to the exact same position as in the experimental wave runs. In other words, the position of a numeric wave gauge initially located at 11.5 metres has been moved to 11.55 metres in order to capture similar data as wave gauge number five in the experimental events.

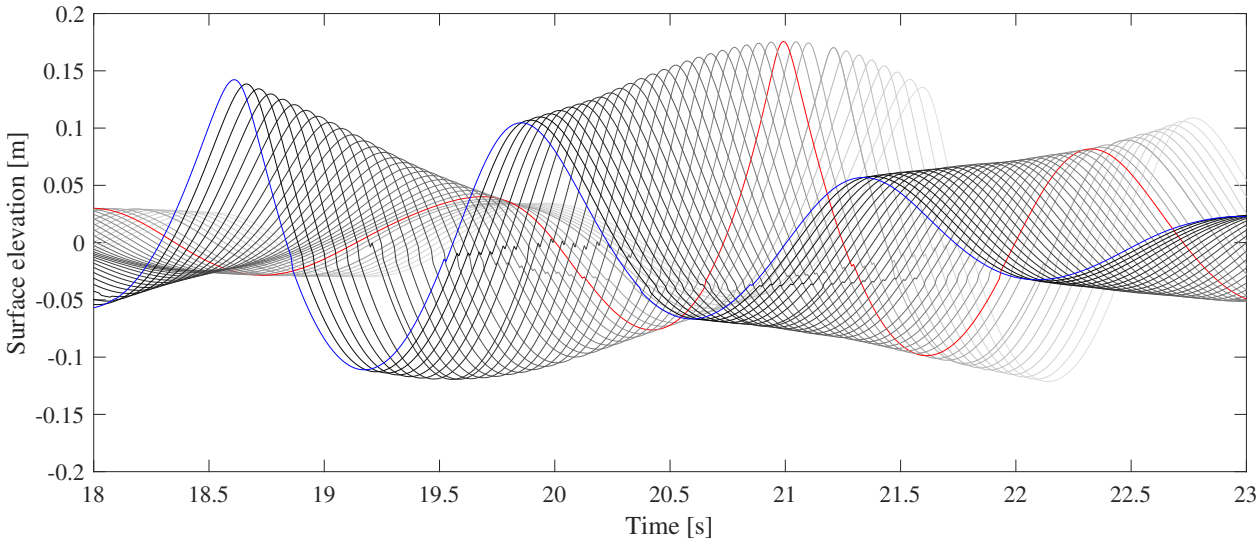

Figure 55: Data from all wave gauges present in the numeric wave event DUD112. The blue line indicates data from the target focal position, while the red line indicates time series with maximum surface elevation.

The method of determining the true numerical focal position is displayed in Figure 55. The blue line indicates data captured at the target focal locating, while the red line indicates the time series with the maximum measured surface elevation. The known distance between

the wave gauges gives the total distance the focal position has shifted relative to the target location. The numerical focal location can be compared to the experimental findings by applying this method to all the numerical wave events. This is displayed in Table 22 where the focal shift in both time and space is given for the experimental and numerical wave cases.

Table 22: Shift in focal location for all DUD wave events, both experimental and numerical.

Wave event	**Shift in focal time [s]**		**Shift in focal position [m]**	
	Experimental	Basilisk	Experimental	Basilisk
DUD37	+ 0.04	+ 0.05	+ 0.00	+ 0.00
DUD73	+ 0.00	+ 0.42	+ 0.00	+ 0.90
DUD101	+ 0.27	+ 0.76	+ 0.73	+ 1.80
DUD112	+ 0.93	+ 0.99	+ 2.20	+ 2.40
DUD115	+ 0.91	+ 1.16	+ 2.20	+ 2.80
DUD121	+ 0.86	+ 1.08	+ 2.20	+ 2.80

The effect of enabling multiple wave gauges becomes apparent when the two data sets are compared. The experimental data gives quite coarse data intervals in terms of focal shift, especially the data for the shift in the focal position, which only contains three unique values. Furthermore, the data from the numerical wave events, with five unique values, offers a much more detailed view of where the true focal position is located. However, the location of the true focal position in the numerical wave events is not necessarily the same as the true focal position in the experimental wave runs.

The results from Table 22 are further visualised in Figure 56, where the effects of multiple wave gauges become clear. Data points from the numerical wave runs make up a significantly smoother function compared to the experimental data. Interestingly, there is a significant offset between the focal location of the numerical and experimental events, especially for the wave case DUD101 with a target amplitude of 101 mm. Looking back at Figure 34, where data from all the six wave gauges are displayed, it is possible that wave gauge number three

has not captured the actual surface elevation properly. This strengthens the belief that the numerical results have managed to capture the true focal location accurately.

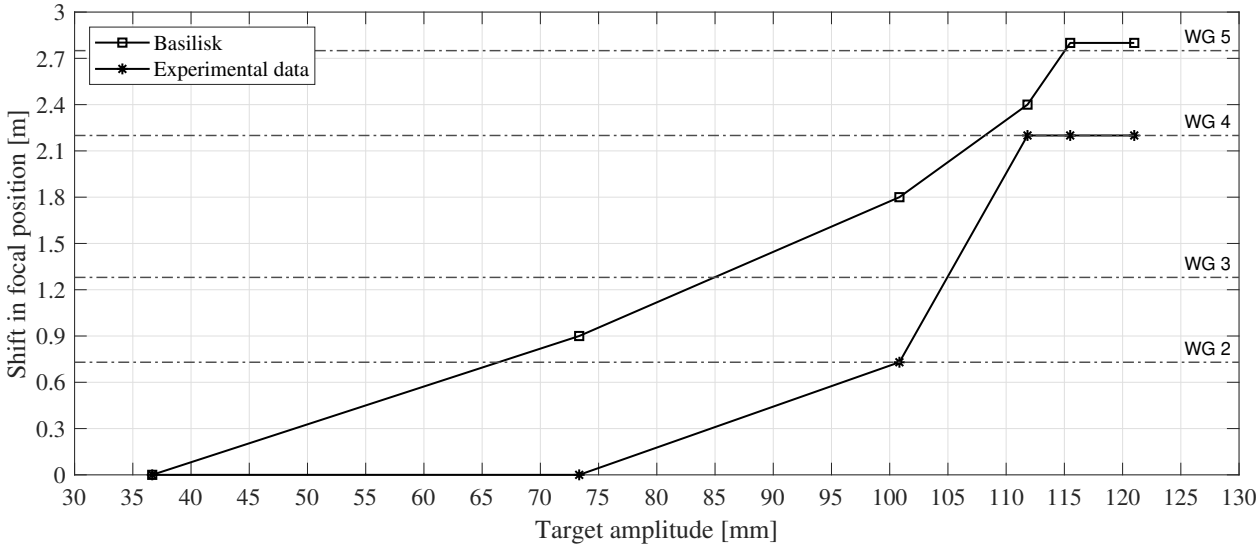

Figure 56: Shift in focal position, relative to the target position at 8.8 metres, as a function of input amplitude. Results from Basilisk are marked with a square, and the experimental data is indicated with an asterisk. Locations of the experimental wave gauges are named and marked with a dashed line.

5.3 Suitability of numerical tool

As this thesis aims to create a highly accurate database of free-surface gravity waves, which can be used for validation of CFD software, the suitability of the Basilisk solver will be assessed in the following section. By now, Basilisk has proven that it can capture highly nonlinear behaviour present in the wave events, strengthening the findings of Ø. Lande in [18]. Furthermore, some of the same parameters used to investigate the experimental wave events will be calculated for the numerical events. Table 23 summarises these parameters for both the experimental and numerical events of DUD37, DUD101 and DUD121.

Table 23: Comparison of key parameters between the numerical and experimental wave event of DUD37, DUD101 and DUD121. Deviation is defined as the difference between the numerical and experimental events, and given as a percentage of the given experimental result.

DUD37			
Parameter	**Experimental**	**Basilisk**	**Deviation [%]**
Maximum wave amplitude [m]	0.0366	0.0378	+ 3.3
Nonlinear amplification [%]	+ 0.0	+ 3.1	-
Steepness (ka)	0.083	0.087	+ 4.8
Focal peak period [s]	1.33	1.32	− 0.7
DUD101			
Parameter	**Experimental**	**Basilisk**	**Deviation [%]**
Maximum wave amplitude [m]	0.1161	0.1395	+ 20.2
Nonlinear amplification [%]	+ 15.1	+ 38.3	-
Steepness (ka)	0.281	0.383	+ 36.5
Focal peak period [s]	1.33	1.21	− 9.0
DUD121			
Parameter	**Experimental**	**Basilisk**	**Deviation [%]**
Maximum wave amplitude [m]	0.1938	0.1972	+ 1.8
Nonlinear amplification [%]	+ 60.1	+ 63.0	-
Steepness (ka)	0.533	0.570	+ 7.0
Focal peak period [s]	1.44	1.18	− 18.1

When comparing the experimental and numerical time series, it is a noticeable trend that the crest elevations for the numerical events exceed the experimental crest elevations. Furthermore, the wave period for the focal peak is shorter in all the numerical events compared to the experimental cases. This could very well result from fine spatial intervals between the wave gauges, which enables a greater range of data collection than the experimental measurements. Hence, the shorter wave periods could also be present in the experimental events but not measured due to the coarse spatial interval of wave gauges. Nevertheless, the parameters

calculated from the numerical data shows good agreement for the smallest and largest wave event but deviates more for the DUD101 event. It is believed that the significant deviation for the DUD101 event is caused by a measurement error present at wave gauge number three in the experimental tests. This can be observed in Figure 34, where the mentioned wave gauge measures a lower amplitude than the adjacent wave gauges, contrary to the expected development of the crest in a focused wave event.

Another way of comparing the CFD time series with the experimental is by calculating the Root Mean Square Error (RMSE) between the two. The 30 seconds long numerical time series has been compared with the first corresponding 30 seconds of the experimental time series in these calculations. Results from the RMSE calculations are displayed in Table 24. RMSE is considered an excellent general-purpose error metric for numerical predictions and offers a good measure of accuracy [44].

Table 24: RMSE value for the numerical time series compared against the experimental time series. All time series are measured at 8.8 metres and relative RMSE value is calculated from the wave events respective target amplitude.

Wave event	**RMSE value [mm]**	**Relative RMSE value [%]**
DUD37	0.86	2.3
DUD73	1.88	2.6
DUD101	4.34	4.3
DUD112	4.35	3.9
DUD115	4.84	4.2
DUD121	5.79	4.8

The accuracy of the numerical prediction is presented best in terms of relative RMSE value. The relative RMSE value is defined as the original RMSE value divided by the target amplitude and given as a percentage. As expected, the RMSE values increase with increasing target amplitude, indicating that the numerical results become less accurate for the largest wave events. Nevertheless, the Basilisk solver offers a fairly accurate prediction for all the

wave events, even the highly nonlinear DUD121 case. Hence, the Basilisk solver is considered to replicate these given wave events well and is suitable for predicting highly nonlinear non-breaking wave events.

6 Conclusion

Using the towing tank present at HVL, irregular focused wave groups have been generated and measured. Some of the wave cases investigated are directly scaled up experiments previously conducted by both TE. Baldock et al. and TB. Johannessen [24, 1]. Direct comparison between the present results and data from TB. Johannessen demonstrates that the Froude scaling of the wave components is accurate and that no measurable uncertainty is associated with water depth differences between the present and previous experiment. Moreover, the present study has been able to advance previous experiments by generating a non-breaking focused wave event with a target amplitude above the wave breaking limit identified by TB. Johannessen for the DUD wave groups.

Nonlinear effects such as wave amplification and shift in both focal position were identified and well in line with previous experiments. The largest wave cases within the narrow banded wave spectrum D experienced a nonlinear amplification of approximately 60 %, and the steepness parameter for these events closely approached the discussed threshold of $ka = 0.55$.

The results from the open-source Basilisk solver demonstrates excellent agreement with the experimental measurements, and the CFD code is able to capture the nonlinear effects caused by wave-wave interactions well. The good agreement between the numerical and experimental investigations not only demonstrates the numerical tool's capabilities to capture nonlinear wave propagation but also strengthens the validity of the upscaled experimental results in a different facility than has previously been tested.

The range of wave events, as well as the demonstrated accuracy of the measurements, and thorough documentation of the wavemaker calibration, will serve as a good foundation for validation of other CFD codes in terms of wave propagation capabilities and the ability to capture nonlinear behaviour such as wave amplification and nonlinear wave-wave interactions. With this research made available as an open database, the experimental data allows future CFD codes to be tuned and then applied for similar conditions at full-scale. As a result,

the validity of the CFD codes can be thoroughly investigated before requiring further validation experiments. Future tests and experiments can then focus on other wave conditions of interest, such as irregular sea-states.

Furthermore, future tests could be focussed more on wave-structure interactions, wave-current and wind-wave interactions, knowing that the chosen and applied CFD code can accurately capture the nonlinear behaviour of steep free-surface gravity waves. With the research presented in this thesis and the open database, the need for extensive validation experiments could potentially be reduced for other students, researchers and industry.

7 Suggestions for Further Work

The present thesis has set the basis for creating an extensive and open database consisting of measurements from free-surface gravity waves generated in a wave tank. However, the current work has only considered uni-directional wave events with wave gauges positioned along the centre line of the tank, thus limiting the CFD validations to two-dimensional codes. Therefore, rearranging the wave gauges in the transverse directions, as well as conducting wave events with directional spreading, would be a natural extension of the work presented in this thesis, such that also three-dimensional CFD codes can be validated with the use of this measurement database.

Furthermore, the measurement database should not only be limited to non-breaking wave events. Numerical simulation tools are constantly improving, and some can also capture wave breaking accurately. Hence, accurately measured wave events where wave breaking occurs will be useful to extend the applicability of the database. In these experiments, it is recommended to use focused irregular waves to ensure stable wave generation and consistency in terms of location within the measurement area where the wave breaking occurs.

As CFD has become a frequently used tool to assess the hydrodynamic interaction with offshore structures, the database can also be expanded to include wave-structure interactions and measurements of how waves propagate around structures such as wind turbine monopiles or semi-submersible platforms. Moreover, the wave kinematics beneath the crest of all the described wave events could also be measured with either ADV or PIV equipment, giving a second way of validating the CFD codes in addition to wave propagating capabilities.

Nevertheless, recommendations for future work are not limited to extending the database. Comparing different CFD codes with the measurements from this thesis can further strengthen the validity of the experiments. For instance, the results obtained with open-source codes such as Basilisk and OpenFOAM could be compared with software such as Star-CCM+ or other commercial CFD tools. Additionally, a standard three-dimensional CFD model could

be developed for the wave tank present at HVL, which could be used for several other bachelor or master's theses in the future.

The following list will summarise the main areas in terms of recommendations for future work.

- Extend the database with surface measurements from wave events with directional spreading and wave breaking. Additionally, wave kinematics can also be captured and presented as a further validation parameter.
- Conduct wave experiments with structures present in the wave tank. Measurements of the surface dynamics of waves propagating through and around the structure can be useful to include in the database.
- Use the database and the measurements and compare different CFD codes in terms of wave propagating capabilities. Also, develop an in-house CFD model of the wave tank at HVL, which can be used by lab engineers, researchers and students in the future.

The work presented in this thesis can be the foundation for several new theses. Furthermore, the extended contribution from these theses will further increase the relevance of the measurement database for industry, researchers and students.

References

[1] TB Johannessen. The effect of directionality on the nonlinear behaviour of extreme transient ocean waves. 1997.

[2] A Toffoli, A Babanin, M Onorato, and T Waseda. Maximum steepness of oceanic waves: Field and laboratory experiments. *Geophysical Research Letters*, 37(5), 2010.

[3] RG Dean and RA Dalrymple. *Water wave mechanics for engineers and scientists*, volume 2. world scientific publishing company, 1991.

[4] GB Airy. Airy's tides and waves. *Encyclopedia Metropolitana*, pages 1817–1845, 1841.

[5] GG Stokes. On the theory of oscillatory waves. *Transactions of the Cambridge philosophical society*, 1880.

[6] RG Dean. Stream function representation of nonlinear ocean waves. *Journal of Geophysical Research*, 70(18):4561–4572, 1965.

[7] JD Fenton. A fifth-order Stokes theory for steady waves. *Journal of waterway, port, coastal, and ocean engineering*, 111(2):216–234, 1985.

[8] PS Tromans, AR Anaturk, P Hagemeijer, et al. A new model for the kinematics of large ocean waves-application as a design wave. In *The first international offshore and polar engineering conference*. International Society of Offshore and Polar Engineers, 1991.

[9] DAG Walker, PH Taylor, and RE Taylor. The shape of large surface waves on the open sea and the Draupner New Year wave. *Applied Ocean Research*, 26(3-4):73–83, 2004.

[10] AK Magnusson and MA Donelan. The Andrea wave characteristics of a measured North Sea rogue wave. *Journal of Offshore Mechanics and Arctic Engineering*, 135(3), 2013.

[11] JB Rozario, PS Tromans, PH Taylor, and M Efthymiou. Comparison of loads predicted using "NewWave" and other wave models with measurements on the Tern structure. In *Wave kinematics and environmental forces*, pages 143–159. Springer, 1993.

[12] T Elzinga and PS Tromans. Validation of NewWave theory and RDWF predictions against measured global loading on a North Sea jacket. 1992.

[13] AC Hunt-Raby, AGL Borthwick, PK Stansby, and PH Taylor. Experimental measurement of focused wave group and solitary wave overtopping. *Journal of Hydraulic Research*, 49(4):450–464, 2011.

[14] W Bai and RE Taylor. Numerical simulation of fully nonlinear regular and focused wave diffraction around a vertical cylinder using domain decomposition. *Applied Ocean Research*, 29(1-2):55–71, 2007.

[15] S Draycott, A Nambiar, B Sellar, T Davey, and V Venugopal. Assessing extreme loads on a tidal turbine using focused wave groups in energetic currents. *Renewable Energy*, 135:1013–1024, 2019.

[16] T Bunnik, A Veldman, P Wellens, et al. Prediction of extreme wave loads in focused wave groups. In *The Eighteenth International Offshore and Polar Engineering Conference*. International Society of Offshore and Polar Engineers, 2008.

[17] T Vyzikas, D Stagonas, C Maisondieu, and D Greaves. Intercomparison of Three Open-Source Numerical Flumes for the Surface Dynamics of Steep Focused Wave Groups. *Fluids*, 6(1):9, 2021.

[18] Ø Lande and TB Johannessen. Propagation of Steep and Breaking Short-Crested Waves: A Comparison of CFD Codes. In *International Conference on Offshore Mechanics and Arctic Engineering*, volume 51210, page V002T08A022. American Society of Mechanical Engineers, 2018.

[19] DZ Ning, J Zang, SX Liu, RE Taylor, B Teng, and PH Taylor. Free-surface evolution and wave kinematics for nonlinear uni-directional focused wave groups. *Ocean Engineering*, 36(15-16):1226–1243, 2009.

[20] B Pettersen. *Pensumhefte, Marin Teknikk 3 - Hydrodynamikk*. Akademika, 2020.

[21] Norske Veritas. *DNVGL-RP-C205 Environmental conditions and environmental loads*. Det Norske Veritas, september 2019 edition, 2000.

[22] JN Sharma, RG Dean, et al. Second-order directional seas and associated wave forces. *Society of Petroleum Engineers Journal*, 21(01):129–140, 1981.

[23] YJ Yang and SH Kwon. Prediction for irregular ocean wave and floating body motion by regularization: Part 1. Irregular wave prediction. *Transactions of FAMENA*, 40(4):41–54, 2016.

[24] TE Baldock, C Swan, and PH Taylor. A laboratory study of nonlinear surface waves on water. *Philosophical Transactions of the Royal Society of London. Series A: Mathematical, Physical and Engineering Sciences*, 354(1707):649–676, 1996.

[25] BH Riise, J Grue, A Jensen, and TB Johannessen. A note on the secondary load cycle for a monopile in irregular deep water waves. *Journal of Fluid Mechanics*, 849, 2018.

[26] EE Bachynski, T Kristiansen, and M Thys. Experimental and numerical investigations of monopile ringing in irregular finite-depth water waves. *Applied Ocean Research*, 68:154–170, 2017.

[27] KF Hasselmann, TP Barnett, E Bouws, H Carlson, DE Cartwright, K Eake, JA Euring, A Gicnapp, DE Hasselmann, P Kruseman, et al. Measurements of wind-wave growth and swell decay during the joint north sea wave project (JONSWAP). *Ergaenzungsheft zur Deutschen Hydrographischen Zeitschrift, Reihe A*, 1973.

[28] W Wang, A Kamath, C Pakozdi, and H Bihs. Investigation of focusing wave properties in a numerical wave tank with a fully nonlinear potential flow model. *Journal of Marine Science and Engineering*, 7(10):375, 2019.

[29] H Bredmose and NG Jacobsen. Breaking wave impacts on offshore wind turbine foundations: focused wave groups and CFD. In *International Conference on Offshore Mechanics and Arctic Engineering*, volume 49118, pages 397–404, 2010.

[30] Edinburgh Designs. Wave Generators. `http://www4.edesign.co.uk/waves/some-wave-1/`. Accessed: 2021-03-28.

[31] S Steen. Experimental methods in marine hydrodynamics. University Lecture, 2014.

[32] Edinburgh Designs. Wave Gauges. `http://www4.edesign.co.uk/product/wavegauges/`. Accessed: 2021-05-9.

[33] E Engebretsen, S Haver, and D Myrhaug. Extreme Wave Condition at Doggerbank. *Journal of Offshore Mechanics and Arctic Engineering*, 138, 05 2016.

[34] GS Payne, JRM Taylor, and D Ingram. Best practice guidelines for tank testing of wave energy converters. *The journal of ocean technology*, 4(4):38–70, 2009.

[35] Basilisk. src/two-phase.h. `http://basilisk.fr/src/two-phase.h`. Accessed: 2021-05-15.

[36] Basilisk. src/navier-stokes/centered.h. `http://basilisk.fr/src/navier-stokes/centered.h`. Accessed: 2021-05-15.

[37] Ø Lande. CFDwavemaker's documentation. `http://www.hydrodynamics.no/CFDwavemaker/`. Accessed: 2021-05-13.

[38] JA van Hooft, S Popinet, CC van Heerwaarden, SJA van der Linden, SR de Roode, and BJH van de Wiel. Towards adaptive grids for atmospheric boundary-layer simulations. *Boundary-layer meteorology*, 167(3):421–443, 2018.

[39] Sandbox/Antoonvh. The Tree-Grid Structure in Basilisk. `http://basilisk.fr/sandbox/Antoonvh/The_Tree-Grid_Structure_in_Basilisk`. Accessed: 2021-05-10.

[40] ParaView. Paraview User's Guide. `https://docs.paraview.org/en/latest/UsersGuide/index.html`. Accessed: 2021-06-12.

[41] Basilisk. src/heights.h. `http://basilisk.fr/src/heights.h`. Accessed: 2021-05-14.

[42] S Popinet. An accurate adaptive solver for surface-tension-driven interfacial flows. *Journal of Computational Physics*, 228(16):5838–5866, 2009.

[43] K Hasselmann. On the non-linear energy transfer in a gravity-wave spectrum Part 1. General theory. *Journal of Fluid Mechanics*, 12(4):481–500, 1962.

[44] SP Neill and MR Hashemi. Chapter 8 - ocean modelling for resource characterization. *Fundamentals of ocean renewable energy*, pages 193–235, 2018.

Appendices

A.1: MATLAB code - Spectral energy density

```
function P = spec2(t,x,y,m,n,ns)
% ------------------------------------------------------------------------
% function P = spec2(t,x,y,m,n,ns)
% ------------------------------------------------------------------------
% Description: performs FFT analysis of the two sequences
%      X and Y.
%      The X and Y sequences of N points are divided into K sections of
%      M points each (M must be a power of two). Using an M-point FFT,
%      successive sections are windowed, FFT'd and accumulated.
%      SPEC returns the M/2 by 8 REAL array. The parameter N is a logical
%      variable used to turn on and off window overlapping. The overlapping
%      length = M/2. NS is the number of points used to define the slope of
%      the window algorithm.
%         P = [F abs(Txy) angle(Txy) RAO_xx Pxx Pyy Pxy Cxy]
%      where
%      F    = frequency (Hz)
%      Pxx  = X-vector power spectral density
%         Pyy  = Y-vector power spectral density
%         Pxy  = Cross spectral density
%         Cxy  = Coherence function between X and Y - not recorded in this modification
%         Pxxc,Pyyc,Pxyc = Confidence range (95 percent).
%
% ------------------------------------------------------------------------
% Author: Øystein Lande
% Date: 2007-08-14
% ------------------------------------------------------------------------

if nargin < 4,
    m = length(t);
    n = 0;
    ns = 128;
end
if nargin == 4,
    n = 0;
    ns = 128;
end
if nargin == 5,
    ns = 128;
end

% load model_ts
% x = elemforce_qua{2}{2};
% y = wave_elev{2}(1:length(wave_elev{2}));
% t = elemforce_qua{2}{1};
% m = 2^14;
% n = 1;

if m < length(t),
    k = floor(length(t)/m)+n*(floor((length(t)-(0.5*m))/m));
    k2 = floor(length(t)/m);
    if ~n
        kk = m*(0:(k-1));

    else
        kk2 = m*(0:(k2-1));
        j = 1;
        for i = 1:2:(2*k2)-1,
            kk(i) = kk2(j);
```

```
            if kk2(j)+(m*(3/2))> length(t),
                break;
            end
            kk(i+1) = kk2(j) +m/2;
            if j == k2
                break;
            end
            j = j + 1;
        end
    end
    kk(1) = 1;
%     kk
%     k
    for i = 1:k,
        Tx(:,i) = x(kk(i):kk(i)+m-1);
        Tt(:,i) = t(kk(i):kk(i)+m-1);
        Ty(:,i) = y(kk(i):kk(i)+m-1);
    end
%     size(Tx)
else
    Tx = x;
    Ty = y;
    Tt = t;
    k = 1;
end
% size(Tx)

% clear;
% P = 0;


% size(elemforce_qua{11}{2})
% size(wave_elev{2})
% plotlength = 5000;
dt = (Tt(length(Tt))-Tt(1))/(length(Tt)-1);
N = length(Tx);
df = 1/(dt*N);
F = (1/dt)*(1:N)/N;
W = 2*pi*(1/dt)*(1:N)/N;
Sxx2 = zeros(1,length(Tx));
Syy2 = zeros(1,length(Tx));
Sxy2 = zeros(1,length(Tx));
lw = landewindow(N,ns);
% plot(Tt(:,1),Tx(:,1).*lw')
% figure
% length(lw)
for i = 1:k,
    Xx = fft(Tx(:,i).*lw')/N;
    % y = fft(elemforce_qua{11}{2});
    % x = fft(wave_elev{2}(1:length(wave_elev{2})));
    Yy = fft(Ty(:,i).*lw')/N;
    % length(x)
    % length(y)
    Sxx = 2*Xx.*conj(Xx)/df;
%     Sxx = (Xx.^2)/df
    Sxy = 2*Xx.*conj(Yy)/df;
    Syy = 2*Yy.*conj(Yy)/df;
    Sxx2 = Sxx2 + Sxx.';
```

```
    Syy2 = Syy2 + Syy.';
    Sxy2 = Sxy2 + Sxy.';
end

Sxx2 = Sxx2/k;
Syy2 = Syy2/k;
Sxy2 = Sxy2/k;
% sqrt(trapz(F(1:plotlength),Syy(1:plotlength)))/3.5


% coherence = sqrt((Sxy.*conj(Sxy))./(Sxx.*Syy));
% subplot(2,1,1)
% plot(F(1:plotlength),abs(Sxy(1:plotlength)))
% subplot(2,1,2)
% plot(F(1:plotlength),angle(Sxy(1:plotlength)))
% figure;
% plot(F(1:plotlength),abs(Syy(1:plotlength)))
%
% figure;

Cxy = (Sxy2.*conj(Sxy2))./(Sxx2.*Syy2);
% Cxy = abs(Sxy2.^2)./(Sxx2.*Syy2);
RAO_xx = sqrt(Sxx2./Syy2);
RAO_xy = Sxy2./Syy2;
%
P = [F' abs(RAO_xy)' angle(RAO_xy)' RAO_xx' Sxx2.' Syy2.' Sxy2.' Cxy' RAO_xy.'];
%
% length(P)

% % subplot(2,1,1)
% plot(F(5:plotlength),RAO_xx(5:plotlength))
% figure;
% subplot(2,1,1)
% plot(F(5:plotlength),abs(RAO_xy(5:plotlength)))
% subplot(2,1,2)
% plot(F(5:plotlength),180*angle(RAO_xy(5:plotlength))/pi)
% % figure
% fid = fopen('SECLRAO_nirwana.dat','w');
% for i = 1:8:plotlength,
%     fprintf(fid,'%7.4f  %7.4f\n',F(i),abs(RAO_xy(i))*10^3);
% end
% plot(F(1:plotlength),coherence(1:plotlength))
% % plot(F(1:plotlength),angle(RAO_1(1:plotlength)))
% % powspec(elemforce_qua{11}{2},wave_elev{2}(1:length(wave_elev{2})-1),0.25)

function w = landewindow(m,n,varargin)
% ------------------------------------------------------------------------
% Generates window for stochastic analysis of timeseries
% m - Number of points in window
% n - Number of points in slope
% ------------------------------------------------------------------------
% Author: Oeystein Lande
% Date: 2007-08-14
% ------------------------------------------------------------------------
% m = 512
% n = 128;

if nargin >= 3,
```

```
    ramptype = varargin{1};
else
    ramptype = 'cosine';
end
if strcmp(ramptype,'cosine')
    for i= 1:n,
        tt(i) = ((1+cos(pi+(pi*(i)/(n)))))/2;
        tt3 = fliplr(tt);
    end
elseif strcmp(ramptype,'linear')
    tt = (0:n-1)./n;
    tt3 = fliplr(tt);
elseif strcmp(ramptype,'nonsymmetric')
    pp = varargin{2};
    tt = (0:pp(1)-1)./pp(1);
    tt3 = [fliplr(tt) zeros(1,m-n-pp(2))];

end



tt2 = ones(1,m-(length(tt)+length(tt3)));

w = [tt tt2 tt3];
% plot(1:64,tt,1:64,fliplr(tt))
% plot(w)
```

A.2: Basilisk - waveflume.c

```
1
2   /**
3   # Simple flume with wavemaker
4   This little example which shows how to implement a simple waveflume in Basilisk,
    where a wave is propagated into the domain from the left boundary. To keep it
    simple, linear wave theory is used. The example may however easily be replace by
    more advanced theories by replacing the functions velox, veloy and wave_elev.
5   The wave elevation at inflow is measured using the waveprobe functionality added
    with "waveprobes.h".
6
7   Oystein Lande 2018
8
9   We start by including the building blocks:
10  */
11  #include <sys/stat.h>
12  #include "grid/quadtree.h"
13  #include "utils.h"
14  #include "navier-stokes/centered.h"
15  #include "two-phase.h"
16  #include "navier-stokes/conserving.h"
17  #include "reduced.h"
18  #include "tension.h"
19
20  #include "adapt_wavelet_leave_interface.h"
21  #include "waveprobes.h"
22  #include "output_vtu_foreach2.h"
23  #include "CFDwavemaker.h"
24  //#include "view.h"
25
26
27
28  /** For simplicity, all input parameters defining the simulation is defined in the
    struct below */
29
30  struct SIM_properties {
31      double tmax; // simulation length
32      double dtmax;
33      double size[4]; // wave flume dimensions, [x_min, x_max, y_min, y_max]
34      double waterlevel; // elevation of stillwater level, relative to domain definition
35      double gravity; // m/s^2 (default 9.81)
36      double rho1; // density of water
37      double rho2; // density of air
38      int refine_init; // refinment level at t = 0
39      int adapt_refine_max; // maximum level of refinement
40      int adapt_refine_min; // minimum level of refinement
41      int adapt_utol;
42  };
43
44  struct SIM_properties simdata = {
45      .tmax = 30.,
46      .dtmax = 0.1,
47      .size = {0.,50.,-2.2,0.75},
48      .waterlevel = 0.0,
49      .gravity =9.81,
50      .rho1 = 1000.,
51      .rho2 = 1.225,
52      .refine_init = 8,
53      .adapt_refine_max = 12,
54      .adapt_refine_min = 6,
55  };
56
57  int num_omp = 6;
58  int vtucount = 0;
59  double slope_start = 42.;
60  double slope_end = 50.;
61  double dampingfac = 0.02;
62
63  /**
64  ## Functions
65  We define some useful functions which will be called further down.
66
67  Sets the domain size and origin according to the specified values in simdata
68  */
```

```
69  void set_domain_size(){
70
71      double lx = simdata.size[1]-simdata.size[0];
72      double lz = simdata.size[3]-simdata.size[2];
73
74      fprintf(stderr,"data:%.2f\n",simdata.size[1]);
75      init_grid (1 << (simdata.refine_init));
76
77      if (lx >= lz){
78          size (lx);
79          origin (simdata.size[0], simdata.size[2]); // move origin
80          //mask (y > dp.size[5]  ? top : none);
81      }
82      else {
83          size (lz);
84          origin (simdata.size[0], simdata.size[2]); // move origin
85          //mask (x > dp.size[1]  ? right : none);
86      }
87  }
88
89
90  /** maskes away parts of the domain to make it the right size*/
91  void  mask_domain(){
92
93      double lx = simdata.size[1]-simdata.size[0];
94      double lz = simdata.size[3]-simdata.size[2];
95
96      if (lx >= lz){
97          mask (y > simdata.size[3]  ? top : none);
98      }
99      else {
100         mask (x > simdata.size[1]  ? right : none);
101     }
102 }
103
104 /** fills the basin and sets kinematics to 0 in entire basin*/
105 void set_kinematics(){
106     // initialize basin with wave
107     scalar phi[];
108     foreach_vertex() {
109         phi[] = -y + simdata.waterlevel;
110     }
111     fractions (phi, f);
112     fprintf(stderr,"Initializing basin velocities... rest...\n");
113     foreach()
114         foreach_dimension()
115             u.x[] =    0.0;
116     boundary((scalar*){f,u});
117 }
118
119 /** Nice to have print function*/
120 void mg_print (mgstats mg)
121 {
122     if (mg.i > 0 && mg.resa > 0.)
123         fprintf (stderr, "#   %d %g %g %g\n", mg.i, mg.resb, mg.resa,
124                  exp (log (mg.resb/mg.resa)/mg.i));
125 }
126
127
128 /** write unstructured vtu files */
129 void save_vtu ( int nf, int j)
130 {
131   char name[80];
132   FILE * fp ;
133   nf > 0 ? sprintf(name, "RES_VTK/res_n%3.3d_%4.4d.vtu",pid(),j) : sprintf(name,
      "RES_VTK/res_%4.4d.vtu",j);
134   fp = fopen(name, "w"); output_vtu_bin_foreach ((scalar *) {f,p}, (vector *) {u},
      N, fp, false); fclose (fp);
135 }
136
137
138 /**
139 ## Setting boundaries */
```

```
140  // Left boundary (wave inflow)
141  u.n[left]  = f[]*dirichlet(wave_VeloX(x,0.,y,t)) + (1.-f[])*neumann(0);
142  u.t[left]  = f[]*dirichlet(wave_VeloZ(x,0.,y,t)) + (1.-f[])*neumann(0);
143  f[left]    = wave_VFrac(x,0.,y,t,Delta);
144
145  // Top boundary
146  u.n[top] = neumann(0);
147  p[top] = dirichlet(u.y[]*abs(u.y[])*rho(f[])*0.5); // this is a neat little trick to
     avoid escalating back-circulating flows in the top boundary.
148
149  // bottom boundary
150  //p[bottom]  = neumann(-a.y[]*fm.y[]*rho(f[])); // Think this is already default,
     but just to be sure...
151
152  /**
153  ## Main loop
154  */
155  int main() {
156      TOLERANCE = 1E-8;
157      mkdir("./RES_VTK",0755); // make a directory to store the resulting VTU files
158
159      //Set domain properties
160      set_domain_size();
161
162      dtmax = simdata.dtmax;
163      rho1 = simdata.rho1, rho2 = simdata.rho2;
164      mu1 = 0., mu2 = 0.;
165
166      G.y = -simdata.gravity;
167      Z.y = 1.;
168
169      omp_set_num_threads(num_omp);
170      int initcheck = wave_Initialize();
171      if (initcheck != 0){
172      fprintf(stdout,"Wavelibrary did not start. aborting\n");
173      return -1;
174      }
175
176      run();
177
178      omp_set_num_threads(1);
179      wave_Cleanup();
180
181  }
182
183
184  /**
185  ### initialize basin at rest
186  */
187  event init (t = 0) {
188      // Mask domain to fit specified size
189      mask_domain();
190      // Set flume surface at rest
191      set_kinematics();
192  }
193
194  /**
195  # Events
196  */
197
198  /** Daming Zone at the rear end of the flume
199  */
200  #if 1
201  event damping(i++) {
202      foreach(){
203          foreach_dimension()
204              u.x[] = x < slope_end ? u.x[] -
                    u.x[]*clamp(((x-slope_start)/(slope_end-slope_start)),0.0,dampingfac) :
                    u.x[];
205      }
206  }
207  #endif
208
```

```
/** This is a useful function to dump some simulation data during runtime, but strictly not neccessary */
#if 1
event logfile (i++) {
    stats s = statsf (f);
    scalar l[];
    foreach()
    l[] = (sqrt(sq(u.x[]) + sq(u.y[])));

    norm n = normf (l);
    fprintf (stderr, "time: %g i: %d dt: %g statsF: %g %g %g", t, i, dt, s.sum, s.min, s.max - 1.);
    fprintf (stderr, ", Urms: %g Umax: %g, speed: %g cellcount: %ld\n", n.rms, n.max, perf.speed, grid->tn);

    mg_print (mgp);
    //mg_print (mgpf);
    mg_print (mgu);
    fflush (stderr);
}
#endif


/**
## Waveprobes
This function uses the height function to calculate the surface elevation at a given point x (or x,y in 3D)
*/
#if 1
event waveprobe (t+=0.008;t<=simdata.tmax) {
    heights (f, h);
    static FILE * fp0 = fopen("waveprobe0.dat", "w");
    double ycoords[2]  = {-0.2,0.25}; // define a vertical line of points
    double yMax0 = wprobe(8.8,ycoords,450);
    double yMax1 = wprobe(8.9,ycoords,450);
    double yMax2 = wprobe(9.0,ycoords,450);
    double yMax3 = wprobe(9.1,ycoords,450);
    double yMax4 = wprobe(9.2,ycoords,450);
    double yMax5 = wprobe(9.3,ycoords,450);
    double yMax6 = wprobe(9.4,ycoords,450);
    double yMax7 = wprobe(9.53,ycoords,450);
    double yMax8 = wprobe(9.6,ycoords,450);
    double yMax9 = wprobe(9.7,ycoords,450);
    double yMax10 = wprobe(9.8,ycoords,450);
    double yMax11 = wprobe(9.9,ycoords,450);
    double yMax12 = wprobe(10.,ycoords,450);
    double yMax13 = wprobe(10.08,ycoords,450);
    double yMax14 = wprobe(10.2,ycoords,450);
    double yMax15 = wprobe(10.3,ycoords,450);
    double yMax16 = wprobe(10.4,ycoords,450);
    double yMax17 = wprobe(10.5,ycoords,450);
    double yMax18 = wprobe(10.6,ycoords,450);
    double yMax19 = wprobe(10.7,ycoords,450);
    double yMax20 = wprobe(10.8,ycoords,450);
    double yMax21 = wprobe(10.9,ycoords,450);
    double yMax22 = wprobe(11.,ycoords,450);
    double yMax23 = wprobe(11.1,ycoords,450);
    double yMax24 = wprobe(11.2,ycoords,450);
    double yMax25 = wprobe(11.3,ycoords,450);
    double yMax26 = wprobe(11.4,ycoords,450);
    double yMax27 = wprobe(11.53,ycoords,450);
    double yMax28 = wprobe(11.6,ycoords,450);
    double yMax29 = wprobe(11.7,ycoords,450);
    double yMax30 = wprobe(11.8,ycoords,450);
    double yMax31 = wprobe(11.9,ycoords,450);
    double yMax32 = wprobe(12.,ycoords,450);
    double yMax33 = wprobe(12.1,ycoords,450);
    double yMax34 = wprobe(12.2,ycoords,450);
    double yMax35 = wprobe(12.28,ycoords,450);
    //double yMax = wave_SurfElev(0.,0.,t);
    // update file
    fprintf(fp0, "%g %g %g %g %g %g %g %g %g %g %g %g %g %g %g %g %g %g %g %g %g %g %g %g %g %g %g %g %g %g %g %g %g %g %g %g %g\n",t,
```

```
        yMax0,yMax1,yMax2,yMax3,yMax4,yMax5,yMax6,yMax7,yMax8,yMax9,yMax10,yMax11,yMax12,y
        Max13,yMax14,yMax15,yMax16,yMax17,yMax18,yMax19,yMax20,yMax21,yMax22,yMax23,yMax24
        ,yMax25,yMax26,yMax27,yMax28,yMax29,yMax30,yMax31,yMax32,yMax33,yMax34,yMax35);
277         fflush(fp0);
278     }
279     #endif
280
281
282     /** dump a vtu file (which can be viewed directly in paraview), for a given
        timeinterval */
283     #if 1
284     event logfilevtu (t=0.0;t<=simdata.tmax;t+=0.1) {
285       save_vtu(0,vtucount);
286       vtucount += 1;
287     }
288     #endif
289
290
291     /**
292     ## mesh adaptation
293     Using a sligtly modified version of adapt_wavelet, which restricts the mesh to be at
        max level around the fluid interface
294     */
295     #if 1
296     event adapt(i++){
297         adapt_wavelet_leave_interface((scalar *){u},{f},(double[]){0.1, 0.1},
            simdata.adapt_refine_max, simdata.adapt_refine_min,1);
298         //adapt_wavelet((scalar *){u,f},(double[]){0.1, 0.1, 0.1},
            simdata.adapt_refine_max, simdata.adapt_refine_min);
299     }
300     #endif
301
302     /**
303     #Results
304     The simulation takes about a min on a resonable desktop computer.
305
306
307     */
308
```

A.3: Basilisk - DUD112 input file

```
@v213
# Long crested wave example

[wave type]
# WAVETYPE
irregular

[general input data]
depth 2.2
mtheta 0.0
normalize 0
amplify 1

[second order]

[wave reference point]
# for focused waves this will correspond to the focus point in time and space
time 20.0
x 8.8
y 0.0

[irregular wave components]
nfreq 28
ndir 1
#   OMEGA      A           K           Phase
        3.8429     0.006009     1.5093     0.0000
        3.9154     0.005789     1.5660     0.0000
        3.9879     0.005580     1.6236     0.0000
        4.0604     0.005382     1.6827     0.0000
        4.1329     0.005195     1.7428     0.0000
        4.2054     0.005018     1.8040     0.0000
        4.2779     0.004849     1.8664     0.0000
        4.3504     0.004689     1.9300     0.0000
        4.4229     0.004536     1.9947     0.0000
        4.4954     0.004391     2.0605     0.0000
        4.5679     0.004253     2.1274     0.0000
        4.6404     0.004121     2.1954     0.0000
        4.7129     0.003995     2.2643     0.0000
        4.7855     0.003875     2.3345     0.0000
        4.8580     0.003760     2.4057     0.0000
        4.9305     0.003650     2.4780     0.0000
        5.0030     0.003545     2.5515     0.0000
        5.0755     0.003445     2.6252     0.0000
        5.1480     0.003348     2.7016     0.0000
        5.2205     0.003256     2.7780     0.0000
        5.2930     0.003167     2.8557     0.0000
        5.3655     0.003082     2.9348     0.0000
        5.4380     0.003001     3.0146     0.0000
        5.5105     0.002922     3.0955     0.0000
        5.5830     0.002847     3.1774     0.0000
        5.6555     0.002774     3.2603     0.0000
        5.7280     0.002704     3.3447     0.0000
        5.8005     0.002637     3.4298     0.0000
# DIRS
```

```
0.00000     1.0
```